Control Systems for Silicon Photonic Microring Devices

Kishore Padmaraju

Submitted in partial fulfillment of the
requirements for the degree of
Doctor of Philosophy
in the Graduate School of Arts and Science

COLUMBIA UNIVERSITY

2014

ABSTRACT

Control Systems for Silicon Photonic Microring-Based Devices

Kishore Padmaraju

The continuing growth of microelectronics in speed, scale, and complexity has led to a looming bandwidth bottleneck for traditional electronic interconnects. This has precipitated the penetration of optical interconnects to smaller, more localized scales, in such applications as data centers, supercomputers, and access networks. For this next generation of optical interconnects, the silicon photonic platform has received wide attention for its ability to manifest, more economical, high-performance photonics. The high index contrast and CMOS compatibility of the silicon platform give the potential to intimately integrate small footprint, power-efficient, high-bandwidth photonic interconnects with existing high-performance CMOS microelectronics.

Within the silicon photonic platform, traditional photonic elements can be manifested with smaller footprint and higher energy-efficiency. Additionally, the high index contrast allows the successful implementation of silicon microring-based devices, which push the limits on achievable footprint and energy-efficiency metrics. While laboratory demonstrations have testified to their capabilities as powerful modulators, switches, and filters, the commercial implementation of microring-based devices is impeded by their susceptibility to fabrication tolerances and their inherent temperature sensitivity.

This work develops and demonstrates methods to resolve the aforementioned sensitivities of microring-based devices. Specifically, the use of integrated heaters to thermally tune and lock microring resonators to laser wavelengths, and the underlying control systems to enable such functionality.

The first developed method utilizes power monitoring to show the successful thermal stabilization of a microring modulator under conditions that would normally render it inoperational. In a later demonstration, the photodetector used for power monitoring is co-integrated with the microring modulator, again demonstrating thermal stabilization

of a microring modulator and validating the use of defect-enhanced silicon photodiodes for on-chip control systems.

Secondly, a generalized method is developed that uses dithering signals to generate anti-symmetric error signals for use in stabilizing microring resonators. A control system utilizing a dithering signal is shown to successfully wavelength lock and thermally stabilize a microring resonator. Characterizations are performed on the robustness and speed of the wavelength locking process when using dithering signals. An FPGA implementation of the control system is used to scale to a WDM microring demultiplexer, demonstrating the simultaneous wavelength locking of multiple microring resonators. Additionally, the dithering technique is adopted to create control systems for microring-based switches, which have traditionally posed a challenging problem due to their multi-state configurations.

The aforementioned control systems are rigorously tested for applications with high speed data and analyzed for power efficiency and scalability to show that they can successfully scale to commercial implementations and be the enabling factor in the commercial deployment of microring-based devices.

Contents

List of Figures

Glossary

ADC Analog-to-Digital Converter

ASIC Application-Specific Integrated Circuit

AWG Arrayed Waveguide Grating

B2B Back to back

BER Bit Error Rate

BERT Bit Error Rate Tester

BPSK Binary Phase Shift Keying

CH Channel

CMOS Complementary Metal Oxide Semiconductor

CW Continuous Wave

DAC Digital-to-Analog Converter

DCA Digital Communications Analyzer

DFB Laser Distributed Feedback Laser

DLI Delay Line Interferometer

DPSK Differential Phase Shift Keying

DUT Device Under Test

E-O Electrical-to-Optical

EDFA Erbium Doped Fiber Amplifier

ER Extinction Ratio

FPGA Field-Programmable Gate Array

FSR Free Spectral Range

IC Integrated Circuit

IL Insertion Loss

IM Intermodulation

LA Limiting Amplifier

MCF Multi-Core Fiber

MZI Mach-Zehnder Interferometer

MZM Mach-Zehnder Modulator

NRZ Non Return to Zero

O-E Optical-to-Electrical

OOK On-Off Keying

OSNR Optical Signal to Noise Ratio

PD Photo Diode

PDH Pound-Drever-Hall

PIC Photonic Integrated Circuit

PID Proportional-Integral-Derivative

PLL Phase-Locked Loop

PM Phase Modulator

PM Fiber Polarization Maintaining Fiber

PON Passive Optical Network

PPG Pulsed Pattern Generator

PRBS Pseudo Random Bit Sequence

PROFA Pitch Reducing Optical Fiber Array

Q Quality Factor

QPSK Quadrature Phase Shift Keying

Rx Receive

SEM Scanning Electron Microscope

SOI Silicon-on-Insulator

SSA Surface State Absorption

SSMF Standard Single Mode Fiber

TE Transverse Electric

TEC Thermo-Electric Cooler

TIA Trans Impedance Amplifier

TL Tunable Laser

TM Transverse Magnetic

Tx Transmit

VOA Variable Optical Attenuator

WDM Wavelength Division Multiplexing

WSS Wavelength-Selective Switch

Acknowledgements

First and foremost, I would like to thank my advisor, Professor Keren Bergman, for enabling my graduate studies. The guidance, resources, and freedom she provided allowed me to pursue the successful research projects that comprise this dissertation.

I would like to thank the dissertation committee members, Professors Richard Osgood, Tony Heinz, Chee Wei Wong, and Luca Carloni, who have provided me valuable input, both directly, and through their students, over the course of my graduate studies. In addition, I thank Professor Heinz for his support and encouragement of our OSA/SPIE student chapter.

I would especially like to thank my collaborators, whose expertise in photonic device design and nanofabrication were the enabler of my graduate work. In particular, Dylan Logan, Jason Ackert, and Professor Andrew Knights of McMaster University; Lian-Wee Luo, Long Chen, Carl Poitras, Sasikanth Manipatruni, Kyle Preston, Qianfan Xu, Bradley Schmidt, Jagat Shakya and Professor Michal Lipson of Cornell University; and Yang Liu and Professor Michael Hochberg of the University of Delaware.

I am indebted to Noam Ophir and Aleksandr Biberman for their mentorship early in my graduate career. Additionally, I am grateful to Lee Zhu, Johnnie Chan, Richard Grote, and Takashi Shiraishi for their assistance in the work that comprises this dissertation, and thankful to all of the members of the Lightwave Research Laboratory, past and present, for their collaboration and friendship. In addition, I would like to thank Jeff Driscoll, James McMillan, and Tingyi Gu, for the innumerable valuable discussions we have had.

Lastly, I would like to thank and acknowledge IBM and the Semiconductor Research Corporation (SRC) for fellowship support, and the SPIE for scholarship support of my graduate studies.

Chapter 1

Introduction

1.1 Silicon Photonics for Next-Generation Optical Interconnects

The growing bandwidth needs of data applications have motivated the replacement of traditionally electronic links with photonic links for information networks as diverse as data centers, supercomputers, and fiber-optic access networks [20, 21]. As is illustrated in Fig. 1.1, the progression of time has brought photonic links to more localized scales as the bandwidth needs at those scales have outstripped the capabilities of traditional electronic links. However, at each progression of scale, the platform on which photonic links manifest themselves must evolve to fit the economic and technology realities in commercial data applications.

The next generation applications of photonic links stress the current portfolio of optical components, rebalancing the emphasis from expensive high-performance components towards low-cost high-volume components that can be closely integrated with electronics. With these considerations in mind, the silicon photonics platform has received wide attention for its ability to deliver the necessary bandwidth required at an economy-of-scale that will be enabled by its compatibility with CMOS fabrication processes [18].

Within the silicon photonic platform, traditional optical components such as low-loss waveguides [22], low-loss waveguide crossings [3], high-speed mach-zhender modulators (MZM) [23], arrayed waveguide-gratings [24], and efficient high-speed photodetectors [4, 25] have been demonstrated. Fig. 1.2 depicts several of these manifested

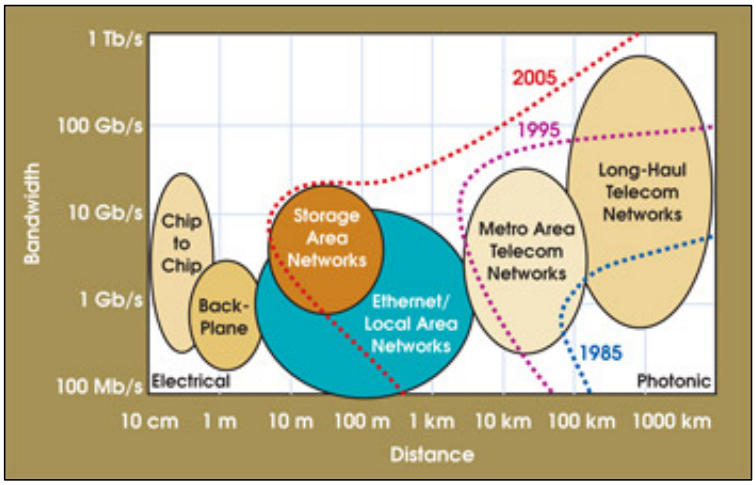

Figure 1.1: Historical displacement of electronic interconnects with photonic interconnects (adapted from [1]).

components in the silicon photonic platform. Leveraging the high index contrast between silicon and silicon-on-insulator, the aforementioned components have been shown with much smaller footprints than their counterparts in more conventional optical platforms. For active devices, these smaller footprints directly translate to higher energy-efficiencies.

As depicted in Fig. 1.3, the past three decades of research in silicon photonics have culminated in the commercial manifestation of the silicon photonic platform. Fig. 1.3 displays only a sample of organizations that are pursuing or enabling the product development of the silicon photonic platform. The large number of organizations partially stems from the variety of ways in which the silicon photonic platform can be manifested, ranging from pure monolithic integration, to hybrid integration, to co-packaging solutions.

While the first generation of commercialization serves as a validation of the silicon photonic platform, it is by far not the culmination of its true potential. In particular, the high-index contrast present in the silicon photonic platform enables the effective use of microring-based devices. These novel microring-based devices have the potential to dramatically push the limits of energy-efficiency and bandwidth-density achievable in a photonic link [26]. While their novelty has attached a great deal of research attention, it has also precluded them from the first generation of silicon photonic commercialization.

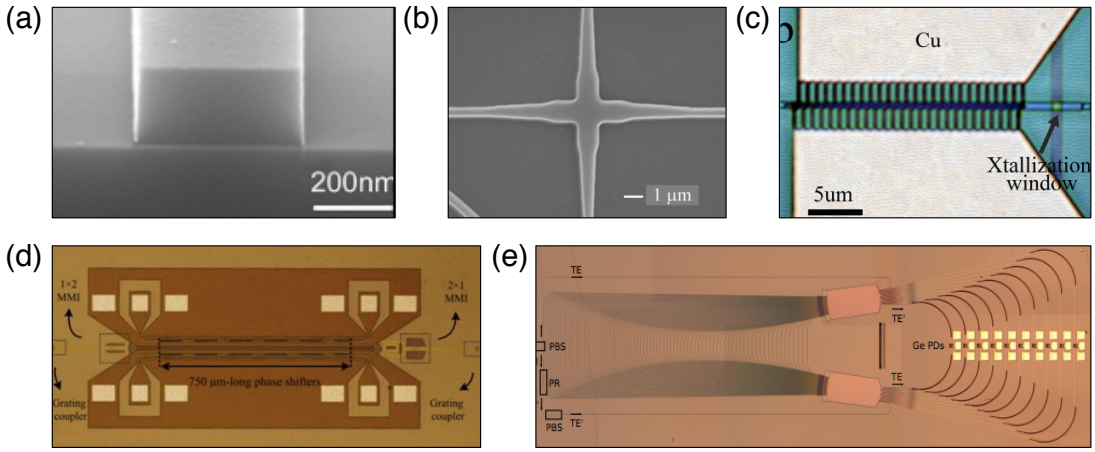

Figure 1.2: Several examples of components in the silicon photonic platform, including (a) low-loss waveguides (adapted from [2]), (b) waveguide crossings (adapted from [3]), (c) germanium photodetectors (adapted from [4]), (d) mach-zhender modulators (MZM) (adapted from [5]), (e) and polarization insensitive arrayed-waveguide-gratings (AWG) (adapted from [6]).

In particular, in what also defines the scope of this dissertation, commercial implementation requires resolving the thermal susceptibility and fabrication offsets of this pioneering new generation of silicon microring-based devices.

1.2 Silicon Microring Devices

The following section will formally define the physical characteristics of microring resonator devices and their basic configurations, establishing a framework for the work covered in this dissertation.

A microring is a traveling wave resonator consisting of a ring structure side-coupled to a bus waveguide. A schematic showing the basic configuration of a microring resonator is shown in Fig. 1.4(a). The optical response of a microring resonator can succinctly be described using the coupling coefficients, t and κ (with the condition that $t^2 + \kappa^2 = 1$), and a, the aggregate round-trip loss of the microring [27, 28]. The relationship between the input, circulating, and output fields (as indicated in Fig. 1.4(a))

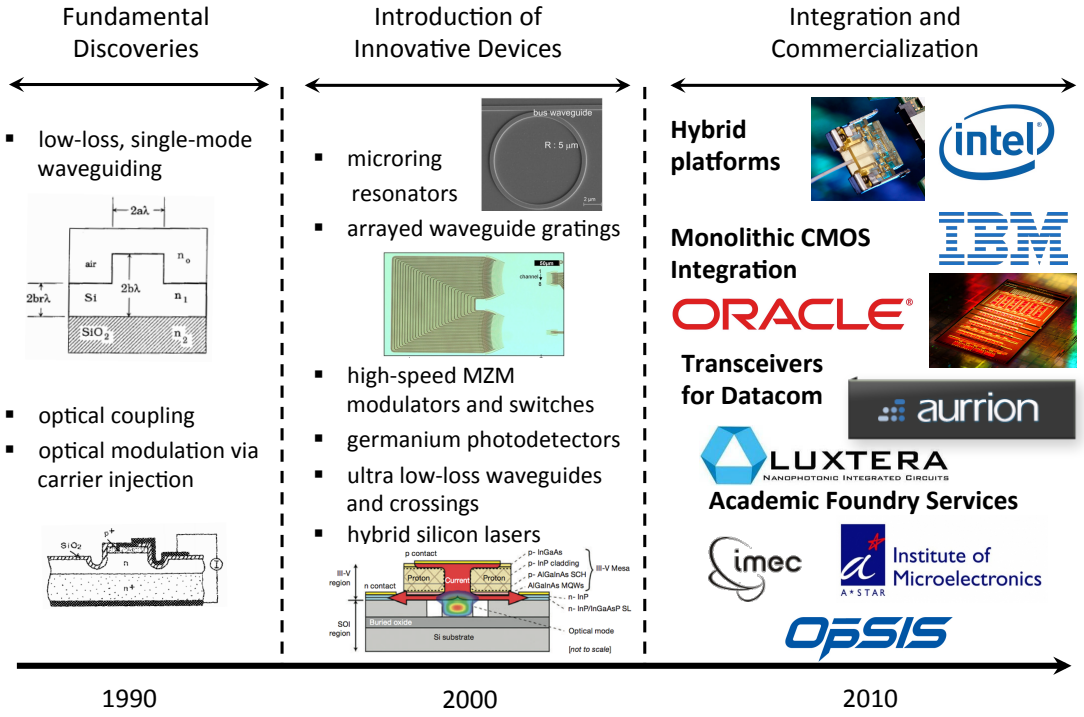

Figure 1.3: Historical progression of silicon photonic technology from fundamental discoveries to current product development and commercialization.

in the coupling region can be described with the matrix transformation:

$$\begin{vmatrix} E_2 \\ E_4 \end{vmatrix} = \begin{vmatrix} t & i\kappa \\ i\kappa & t \end{vmatrix} \begin{vmatrix} E_1 \\ E_3 \end{vmatrix} \tag{1.1}$$

Additionally, within the microring, $E_3 = ae^{i\theta}E_4$ where $\theta = \beta L$ is the round-trip phase accumulation, with β as the propagation constant of the optical mode, and L as the physical length of the ring [27]. The relationship between the input and output fields is then given as

$$\left(\frac{E_{output}}{E_{input}}\right) = \left(\frac{E_2}{E_1}\right) = \frac{te^{-i\theta} - a}{e^{-i\theta} - ta} \tag{1.2}$$

The transmission of the basic ring resonator configuration can then be expressed as

$$T = \left(\frac{E_{output}}{E_{input}}\right)^2 = \frac{a^2 + t^2 - 2at\cos\theta}{1 - a^2t^2 - 2at\cos\theta} \tag{1.3}$$

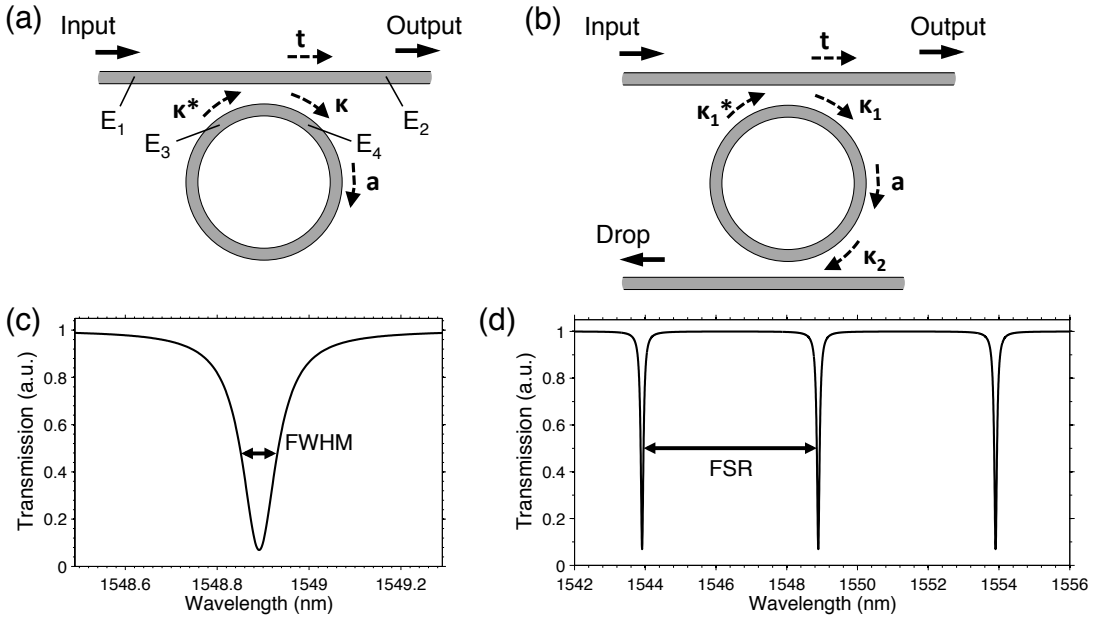

Figure 1.4: (a) Schematic showing the basic configuration of a ring resonator. (b) Configuration of the ring resonator with a drop port. (c) Example spectrum of a silicon microring resonator, identifying the full-width at half maximum (FWHM) metric. (d) Example spectrum of a silicon microring resonator, showing the wavelength-periodic resonances, and the free-spectral range (FSR).

Fig. 1.4(c) evaluates the transmission spectrum in Eq. 1.3 for parameters typical of a silicon microring resonator. Indicated in the graph is the full-width at half-maximum (FWHM) of the microring resonance, also equated as $\Delta\lambda$ in the wavelength regime. The quality factor, Q, approximated as $Q \approx \lambda_0/\Delta\lambda$ (where λ_0 is the resonant wavelength) is one of the important metrics for evaluating the resonator's suitability for telecomm applications. Other important metrics for microring resonators are the extinction ratio, describing the suppression of the transmitted light at the resonant wavelength, and the free spectral range (FSR), describing the wavelength spacing between successive resonances (Fig. 1.4(d)). The resonant wavelengths occur when the optical length of the ring is an integer multiple of the wavelength:

$$\lambda_0 = \frac{n_{eff} L}{m} \tag{1.4}$$

where n_{eff} is the effective index, and m is an integer [29].

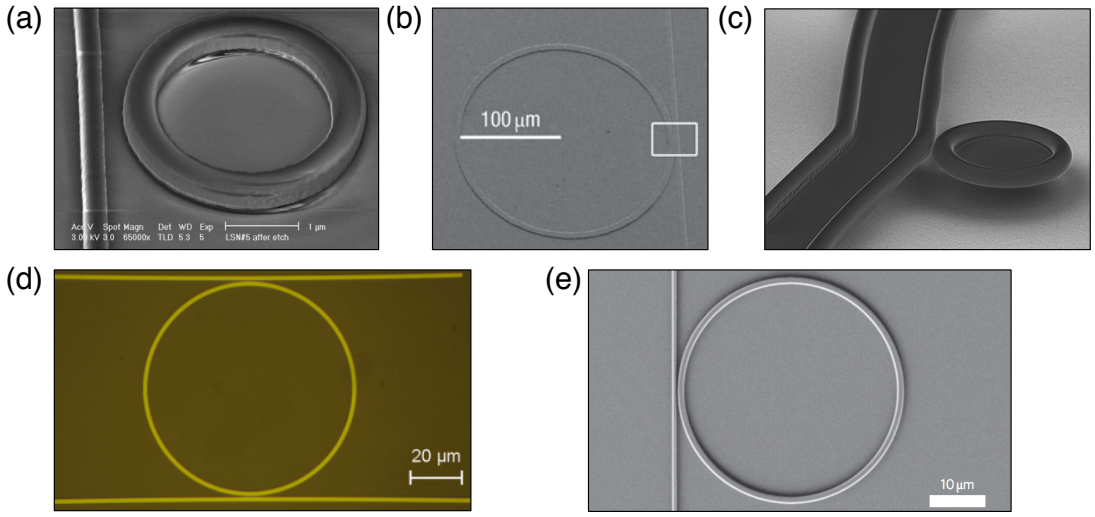

Figure 1.5: (a) Microring resonator on SOI platform (adapted from [7]). (b) Lithium niobate microring resonator (adapted from [8]). (c) Whispering gallery-mode silica microtoroid resonator (adapted from [9]). (d) Microring resonator on silicon-on-sapphire (SOS) platform (adapted from [10]). (e) Silicon nitride microring resonator (adapted from [11]).

The generalized expressions and parameters given prior are enough to model the basic spectral characteristics of simple microring resonator systems. Additional variants, such the additional drop-port configuration depicted in Fig. 1.4(b), can be modeled by adding additional coupling and loss parameters as necessary [29].

As shown in Fig. 1.5, the simple configuration of the ring resonator system has led to its manifestation on a variety of platforms, including, silicon-on-insulator, lithium niobate ($LiNbO_3$), silica, silicon-on-sapphire (SOS), silicon nitride (SiN), fiber, and III-V materials [7, 8, 9, 10, 11]. However, it can safely be argued that the SOI manifestation of the microring resonator has received the greatest amount of attention in the research community. The popularity of the silicon microring resonator can be partly be attributed to its role as a component of the silicon photonic platform, and the associated advantages of the silicon photonic platform that were discussed prior. However, there are several key advantages of the SOI platform that aid in making silicon microring resonators ideal for use in photonic interconnects:

1. The loss in silicon waveguides and coupling regions is sufficiently low as to achieve Q factors high enough for essential telecomm functions such as filtering, switching, and modulation.

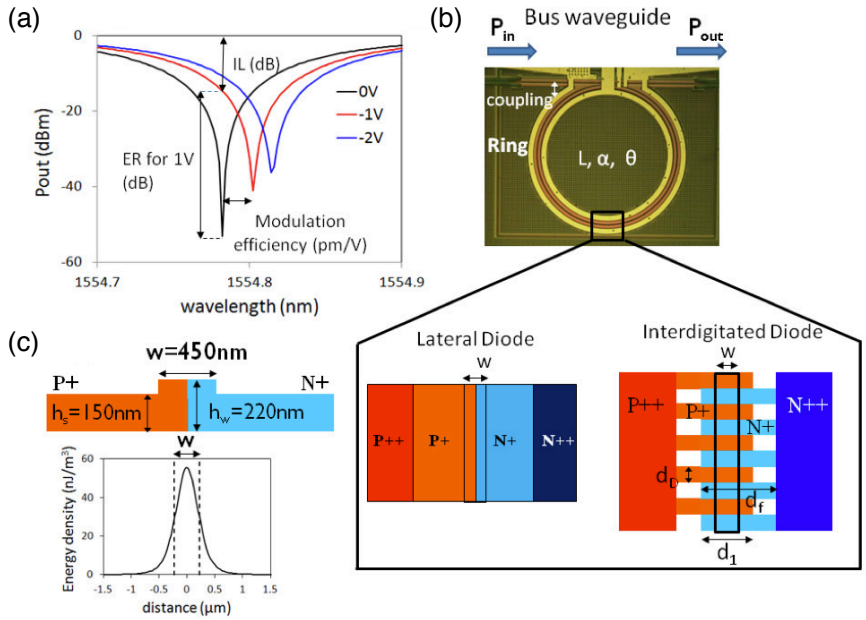

Figure 1.6: (a) Transmission spectrum of a carrier depletion microring modulator at various applied bias. (b) Ring modulator schematic showing the possibility of either a lateral or interdigitated diode design. (c) Ring waveguide cross-section and optical mode distribution (adapted from [12]).

2. The high-index contrast between Si and SiO_2 allows high modal confinement, in turn enabling higher bending radii in Si waveguides. The smaller achievable microrings enable large FSRs, allowing large spectral regions of the telecomm band to be used without repeating resonances.

3. The electro-optic free-carrier plasma-dispersion effect available on the silicon photonic platform enables high-speed microring modulators and switches.

These advantages have allowed silicon microring resonators to be manifested as small as 1.5 μm in radius [7], and when used in conjunction with the free-carrier dispersion effect [30], well into the GHz-rate bandwidth. Fig. 1.6(a) illustrates the optical resonance of the microring and its shift with applied electrical bias [12]. In their most basic capacity they can serve as effective filters [31], switches [15, 32], and modulators with bit-rates as high as 60 Gb/s [33, 34].

Additionally, microrings can be multiplexed along the same waveguide bus, with each microring being offset to provide functionality for a specific wavelength. In

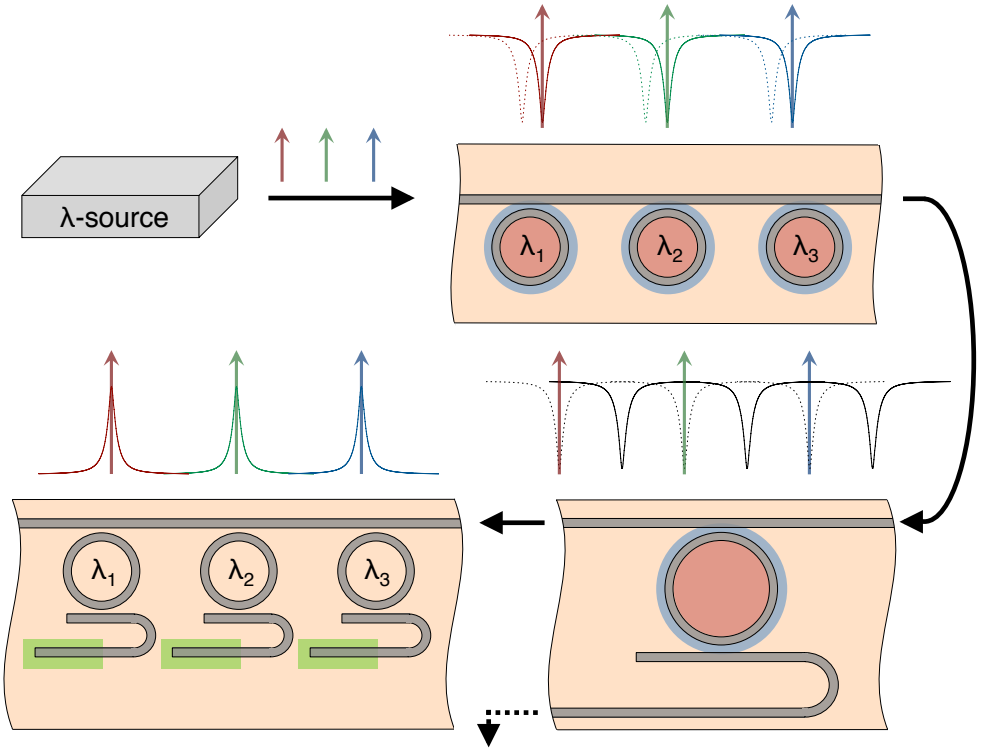

Figure 1.7: An optical link composed of microring-based devices. A wavelength source (λ-source) is modulated by multiplexed microring modulators (doped in a diode configuration to enable fast carrier-induced resonance shifts). A microring switch can then route the entire set of signals appropriately before it is received by a demultiplexing array.

this manner, the microring lends itself naturally for wavelength-division-multiplexed (WDM) operation, a common solution for multiplying the bandwidth of optical links [35]. Fig. 1.7 illustrates the multiplexing of microring modulators for the generation of WDM optical data as well as a microring switch for fast WDM routing, with an array of microring filters on the receive side for demultiplexing the WDM stream [31].

These silicon microring-based devices push the limits on footprint and energy efficiency and provide an ideal solution for enabling low-cost WDM communication within the silicon photonics platform. Commercially implemented microring-based optical networks will likely be application-tailored through the optimization of such microring characteristics as optical insertion loss, crosstalk, footprint, modulation-bandwidth, -linearity, and -depth [26, 36, 37]. However, superseding these parameters in importance is the issue of thermal susceptibility. For the successful migration of microring res-

onators from academic novelty to commercial implementation, the thermal challenges that plague silicon microring-based devices must be resolved.

1.3 Thermal Challenges for Silicon Microring Devices

Most optical devices exhibit some vulnerability to temperature changes. However, the high thermo-optic coefficient of silicon (1.86x10^{-4} K^{-1}) and the wavelength selectivity of microring resonators make them especially susceptible to fluctuations in temperature [38]. The shift in the resonant wavelength of a microring with respect to temperature is given by

$$\frac{d\lambda}{dT} = \left(n_{eff}\alpha_{sub} + \frac{\partial n_{eff}}{\partial T} \right) \frac{\lambda_0}{n_g} \tag{1.5}$$

where λ_0 is the resonant wavelength, n_{eff} is the effective index, α_{sub} is the substrate expansion coefficient, and n_g is the group index [13, 39]. While not explicitly indicated in Eq. 1.5, these terms will have wavelength dependence. Because the optical mode is tightly confined in the silicon core, and also because the thermo-optic coefficient of SiO_2 (1x10^{-5} K^{-1}) is a magnitude lower than that of Si, the corresponding contribution is omitted from Eq. 1.5. Additionally, because α_{sub} (2.6x10^{-6} K^{-1} for a Si substrate) is two orders of magnitude smaller than the thermo-optic coefficient for silicon, it can be omitted as well [40], leaving the commonly reduced expression:

$$\frac{d\lambda}{dT} = \frac{\partial n_{eff}}{\partial T} \frac{\lambda_0}{n_g} \tag{1.6}$$

The repercussions of resonance shifts on microring functionality will be dependent on the Q of the resonance. However, for typical applications, deviations in temperature > 1 K will render most silicon microring-based devices inoperable [41]. This susceptibility of microring-based devices is not compatible with the temperature ranges typical of microelectronic environments. It should be clarified that it is not the absolute temperature that is hazardous for microring functionality; rather, it is the relative changes in temperature during active operation of the optical link.

Resolutions to this problem can be classified into two categories:

1. Solutions that reduce the thermal dependence of the microring resonator (denoted as **"athermal solutions"**).

2. Solutions that actively maintain the local temperature of the microring resonator (denoted as **"control-based solutions"**).

In general, a significant advantage of athermal solutions is that they require no active power consumption to implement. The disadvantages of athermal solutions are their difficulty in fabricating, either through the incorporation of non-CMOS materials, or additional photonic structures. In contrast, the only additional structures that control-based systems typically require are integrated heaters and photodetectors, elements that are readily available in a typical silicon photonic platform. However, the main disadvantage of control-based systems is their active power consumption.

Before committing to either class of solutions, further system analysis must be given consideration. Specifically, the laser sources driving the optical link must be evaluated. Currently, in commercial telecommunication links, laser wavelengths are kept locked to a fixed wavelength grid (the ITU standard). However, for the future short-reach interconnects that silicon-photonic devices are envisioned to populate, a different class of low-power laser sources will be required [26, 42, 43, 44]. For athermal solutions, it will be required that laser wavelengths are fixed to the resonant wavelengths of the microring resonators, and that the stability of the laser wavelength can be ensured throughout operation of the optical link. In contrast, for control-based solutions no such constraints are needed for the initial wavelengths of the laser source, or for guaranteeing wavelength stability. Fluctuations in wavelength are analogous to fluctuations in temperature; any control system that corrects for temperature changes will correspondingly be able to correct for fluctuations in wavelength as well. Ultimately, when considering the larger system design, any power required to stabilize the laser source must be included when weighing the advantages and disadvantages of these two classes of solutions.

1.3.1 Athermal Solutions

The goal of athermalizing silicon microring-based devices is to significantly decrease the temperature-dependence of the microring resonance (the use of the term "athermal" is somewhat of a misnomer because the temperature dependence is never completely eliminated, just reduced to a tolerable level for a select wavelength range). The two

dominant techniques for achieving athermalization is the use of materials with negative thermo-optic coefficients (silicon has a positive thermo-optic coefficient) in waveguide claddings, and embedment of the microring in a thermally balanced interferometer.

1.3.1.1 Athermalization using Negative Thermo-optic Materials

The concept of using a negative thermo-optic polymer cladding for the athermalization of optical waveguides was first introduced by Kokobun *et al* [45], and has since been adapted to silicon microring resonators. The goal of this technique is to produce an aggregate thermo-optic coefficient for the waveguide which is zero, with the thermo-optic coefficient defined as

$$\frac{\partial n_{eff}}{\partial T} = \Gamma_{core}\frac{\partial n_{core}}{\partial T} + \Gamma_{cladding}\frac{\partial n_{cladding}}{\partial T} + \Gamma_{substrate}\frac{\partial n_{substrate}}{\partial T} \tag{1.7}$$

where Γ is the modal confinement factor for the core, cladding, and substrate, as specified [46]. The modal confinement and negative thermo-optic coefficient of the cladding are engineered to balance the modal confinement and positive thermo-optic coefficients of the core (Si) and substrate (SiO_2). It should be noted that the wavelength dependency is not denoted in Eq. 1.7, and furthermore, only linear terms have been included. Higher-order wavelength dependencies of the thermo-optic coefficient make it difficult to achieve athermal behavior over a broad wavelength and temperature range [46, 47].

The high thermo-optic coefficient and modal confinement of silicon waveguides makes it difficult to balance Eq. 1.7 such that the net thermo-optic coefficient is zero. In addition to finding a polymer with a negative thermo-optic coefficient of the same magnitude as Si, it is necessary to re-engineer the optical mode such that it is more distributed in the polymer cladding (a larger $\Gamma_{cladding}$). Demonstrated methods to achieve this have involved narrowing or thinning the waveguide, or utilizing a slotted structure [13, 40, 48, 49, 50]. Fig. 1.8(a) depicts a typical cross-section of a polymer-clad silicon waveguide. As the waveguide is narrowed or thinned, more of the optical mode is distributed in the polymer cladding. The graph in Fig. 1.8(b) quantitatively shows this relationship, and identifies a waveguide dimension for which Eq. 1.7 balances for a particular wavelength and polymer cladding. In particular, this design was able to reduce the temperature dependent (resonant) wavelength shift (TDWS) to -5 pm/K

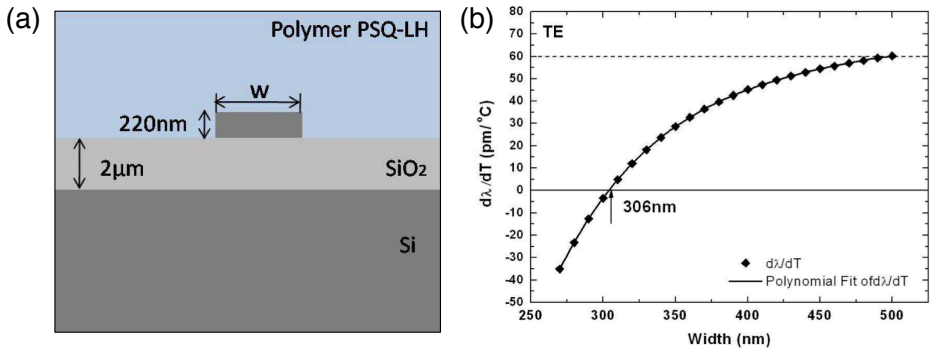

Figure 1.8: (a) Cross-section of a SOI waveguide with negative thermo-optic polymer overlay. (b) Calculated wavelength temperature dependence of the TE mode as a function of waveguide widths (adapted from [13]).

over a range of 50 K [13]. More recent work has established TDWS as low as 0.2 pm/K [47].

The strict requirement on waveguide dimensions may make it difficult to consistently achieve the desired athermalization given the tolerances achievable in currently fabricated silicon photonic structures. A possible resolution to this issue is to use photosensitive materials, such as chalcogenide glasses, to enable the thermo-optic coefficient to be trimmed post-fabrication as necessary [49, 51, 52].

In addition to the difficulty in precisely tuning the thermo-optic coefficient of the polymers, additional consideration must be given to their compatibility with the CMOS-fabrication processes that are envisioned for the future production of silicon photonic platforms. In particular, polymers are vulnerable to degradation, especially when exposed to high temperatures, as would exist in certain stages of a typical CMOS-process cycle [53]. Additionally, polymers suffer from chemical instability, UV aging, and poor mechanical characteristics [54].

Given these detrimental characteristics of polymers, recent research has focused on the use of titanium dioxide (TiO_2) for use in negative thermo-optic coefficient cladding material [54, 55, 56, 57]. TiO_2 is one of the few CMOS-compatible materials that has a negative thermo-optic coefficient ($\sim$ -1.8x10^{-4} K^{-1}) on the same order of Si [55]. TiO_2-clad silicon microring resonators have been demonstrated to have a TDWS $<$ 2 pm/K over a range of 5 K, and importantly, have been shown to be capable of current-injection induced resonance shifts (necessary for high-speed modulation) [56].

The aforementioned results show that negative thermo-optic coefficient materials can be effectively used to drastically reduce the thermal susceptibility of silicon microring resonators, making them appropriate for applications in microelectronics. However, the difficulty in the solution lies in the incorporation of said materials, whether polymer or TiO_2, into a CMOS compatible fabrication process. Additionally, these configurations must be able to fall within the fabrication tolerances of said processes (or be able to be tuned post-fabrication). Finally, it should be noted that the required reduction in the modal confinement of the core will have consequences on the losses of the microring in straight and bent configurations, negatively impacting such desired attributes as footprint and Q-factor [46].

1.3.1.2 Athermalization using an Inteferometric Structure

An alternative to using negative thermo-optic materials is to embed the microring resonator in a thermally matched mach-zhender interferometer (MZI). It has been shown that a silicon MZI can be athermalized by engineering the optical modes in each arm of the MZI. Specifically, the width of the waveguides in the MZI is varied so that the guided mode in each arm of the MZI experiences a different effective thermo-optic coefficient. This is balanced against the length of the arms to produce an overall athermal optical response for the MZI filter [58, 59]. It is possible to adapt this technique to microring resonators by embedding the resonator in one arm of the MZI, as seen in Fig. 1.9(a).

Fig. 1.9(c) shows that the structure can be designed such that the thermal sensitivity of the microring resonator cancels the thermal sensitivity of the MZI it is embedded in. However, because the dependence of the phase shift of the MZI with respect to temperature is linear, whereas it is nonlinear for the microring resonator, the resultant optical resonance will slightly deviate and deform across a given temperature range [14]. By embedding a PN junction in the microring it has been shown that this device can be utilized as an athermal microring modulator [60]. However, the slight deformation and deviation in the MZI-embedded microring resonator's optical response across the temperature range sometimes yields atypical modulation, albeit, this may be sufficient for some applications.

The advantage of this technique is clear, the introduction of the thermally balanced MZI structure does not require the incorporation of any new layers or materials

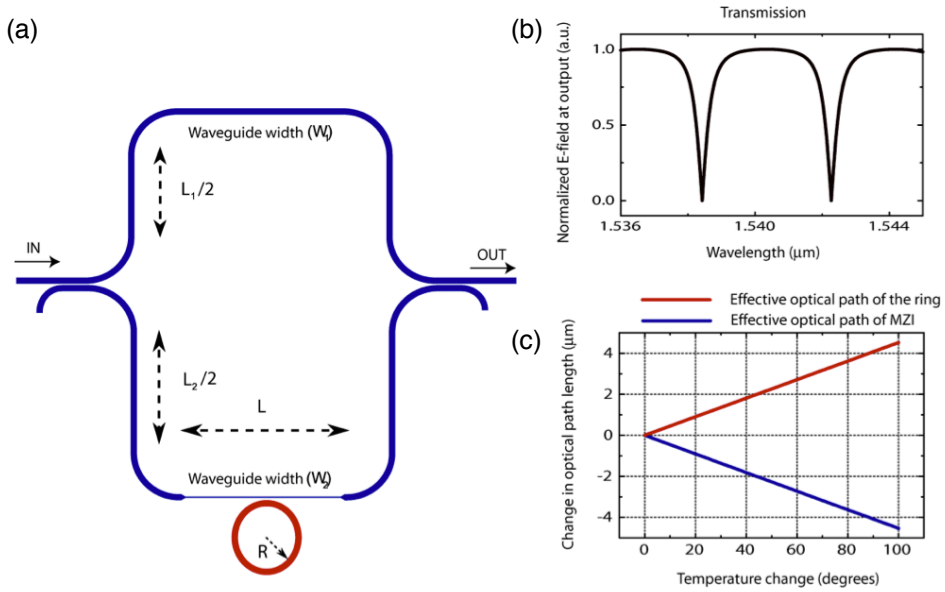

Figure 1.9: (a) Schematic of a microring resonator embedded in a thermally engineered MZI, showing the various waveguide lengths and widths. The MZI is highlighted in blue and the microring in red. (b) Typical transmission spectrum for such a device with a 40 μm microring radius. (c) Change in optical path length with temperature for the microring and MZI. The devices are designed to have opposite and equal phase shifts with change in temperature (adapted from [14]).

in the fabrication of the silicon photonic structure. In contrast to the athermal solutions utilizing a negative thermo-optic material, this solution can be readily integrated using current CMOS-fabrication techniques. However, the structure still suffers from susceptibility to fabrication tolerances, and furthermore, increases the footprint of the microring structure. Additionally, it is non-trivial to adapt the technique to larger microring switch fabrics [15].

1.3.2 Control-based Solutions

While the zero energy-consumption properties of athermal solutions are ideal, their fabrication challenges impede their current deployment, and future research advancements are needed to resolve the required compromises in modal confinement. For example, typical silicon microring resonators have modal confinements as high as 0.95 [61], whereas the reviewed athermal designs can only achieve modal confinements on

the order of 0.5. In order to increase the modal confinement of an athermal microring it would be necessary to find a cladding material with a negative thermo-optic coefficient not only on the same order as the thermo-optic coefficient of silicon, but a magnitude of order greater than it. For these reasons, athermal solutions are still a nascent solution that needs further development before being practically applicable to commercial implementations of silicon microring resonators. This conclusion leads to consideration of the other class of solutions for resolving the thermal susceptibility of microring resonators: control-based solutions.

While athermal solutions work by removing the thermal sensitivity of silicon microring resonators, control-based solutions operate by maintaining the local temperature of the microring resonator throughout the duration of its operation. This is accomplished through the use of an integrated heater localized to the microring resonator. Because cooling solutions (such as peltier coolers) are prohibitively power inefficient, there is no practical method to effectively cool microring resonators. Rather, leveraging the periodic nature of the microrings optical resonances, the predominant solution is to use integrated heaters to "*run the microring hot*" during the system initialization. Subsequent decreases or increases in environmental temperature can then be corrected for by increasing and decreasing, respectively, the power delivered to the integrated heater.

In its generalized form, control systems require a method to monitor the temperature drift of the microring resonator, a feedback controller to condition the response, and a method to adjust the local temperature of the microring resonator (the integrated heater). Hence, there are two major components to any control-based solution, the integrated heater controlling the local temperature of the microring resonator, and the control-system driving the integrated heater. The characteristics of each of these components, including the power consumption and ease of implementation, can be analyzed separately.

Because the scope of this thesis is on the control-systems driving the integrated heaters, a thorough review of current integrated heater technology will be given, followed by a survey of control-systems implemented by other researchers.

1.3.2.1 Integrated Heaters

Integrated heaters are resistive elements and are typically constructed from nichrome, titanium, or doped silicon materials. Running current through these resistive structures

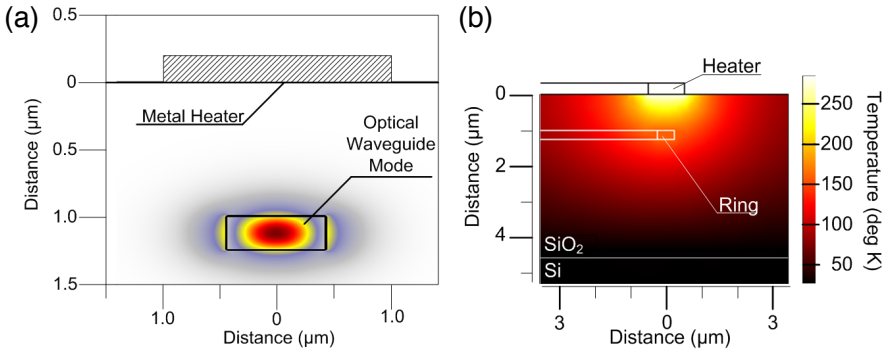

Figure 1.10: Standard optimized design for integrated heaters: (a) the optical mode is separated from the heater to avoid absorption while (b) maintaining enough proximity to couple heat into the waveguide (adapted from [15]).

generates heat, which can be used to tune the local temperature of the microring resonator. The critical metrics for integrated heaters are their tuning efficiency and their tuning speed. While the tuning efficiency is typically given in (mW/nm) or (mW/GHz), a more universal metric is to express the tuning efficiency as the power required to tune the microring resonator by one free-spectral-range (FSR). The (mW/nm) metric increases with increasing microring size, however, because the FSR of the microring also correspondingly decrease, the (mW/FSR), also denoted as (mW/2π), will remain relatively constant across varying microring sizes [62]. This is useful for comparing tuning efficiency results of integrated heaters on microring resonators of different radii.

The cross-sections in Fig. 1.10 depicts the normal configuration for integrated heaters, whereby a thermally grown SiO_2 layer of $\sim$1 μm separates the metal heater from the silicon waveguide [15]. The separation between the heater and silicon waveguide is required to protect the optical mode (Fig. 1.10(a)). The tuning efficiency is not optimal as a consequence of the separation, as the generated heat has to diffuse from the point-like source of the heater down to the silicon waveguide (Fig. 1.10(b)). While this configuration is the easiest to implement in fabrication, demonstrated tuning efficiencies are limited, with most results ranging around $\sim$100 mW/FSR [15, 63, 64, 65], and the best demonstration at $\sim$42 mW/FSR with a tuning speed of 14 μs [66]. These tuning efficiencies may be sufficient for some applications, but for the applications with the most stringent requirements on interconnect power consumption an improved tuning efficiency will be required. Demonstrations have shown that the tuning efficiency can

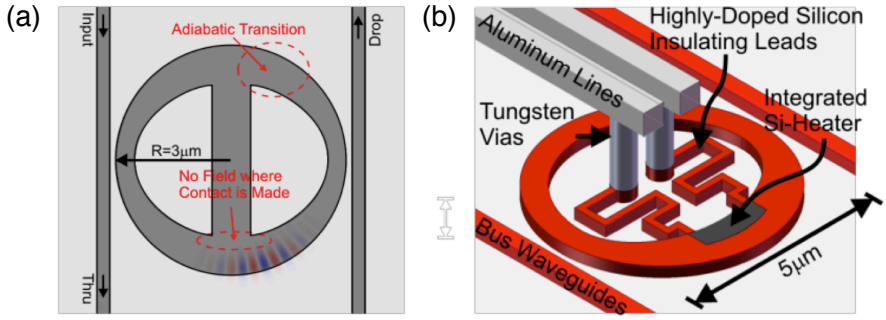

Figure 1.11: (a) FD-TD simulation of an adiabatic microring resonator. (b) Diagram of an adiabatic microring resonator with integrated heaters (adapted from [16]).

be improved by either locating the integrated heater closer to the microring resonator or by improving the thermal isolation of the microring.

There is an inherent difficulty in locating the integrated heater closer to the microring resonator without causing the optical mode to incur additional scattering loss. A solution to resolving this problem is to utilize a microdisk resonator (functionality equivalent to a microring resonator) and place the integrated heater within the interior of the resonator. However, microdisk structures also support additional optical modes which corrupt the FSR of the resonator. The use of adiabatic microring resonators merges the benefits of microring and microdisk structures, allowing interior connections to the resonator while suppressing spurious optical modes and maintaining a small footprint [67]. Fig. 1.11(a) depicts the form factor of an adiabatic microring resonator, and the direct integration of a heater within the resonator (Fig. 1.11(b)). Leveraging the intimate placement of the heater, tuning powers as low as ~20 mW/FSR with tuning speeds as fast as ~1 μs were demonstrated [16]. Additionally, it was shown that adiabatic microring modulators could be fabricated [68]. Modulators with interior integrated heaters have been shown to be able to produce error-free 10 Gb/s modulation across a 60 K temperature tuning range, with comparable tuning efficiencies [69].

Another method to improve the tuning efficiency of integrated heaters is to increase the thermal isolation of microring resonators. Ordinarily, much of the heat generated by the integrated heater is dissipated into the surrounding oxide and substrate. To prevent this, air trenches can be etched around the resonator structure, increasing its thermal isolation from the surrounding environment (Fig. 1.12(a)). Using this technique, tuning powers of 21 mW/FSR with tuning time constants < 10 μs were demonstrated [70].

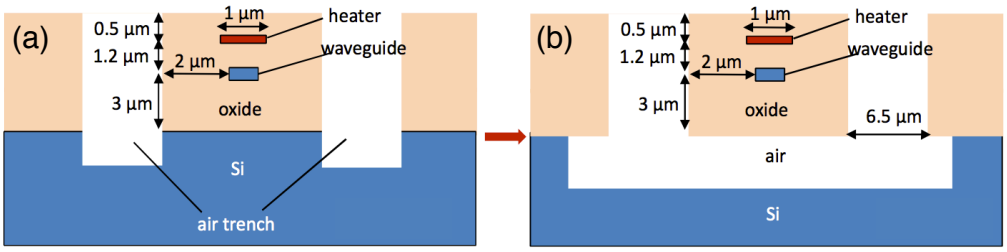

Figure 1.12: (a) Cross-section of the resonator waveguide with air trenches. (b) Cross-section of the resonator waveguide with undercuts beneath the waveguides (adapted from [17]).

Further improvements in tuning efficiency can be obtained by completely thermally isolating the resonator structure from the silicon substrate (Fig. 1.12(b)). The particulars of the nanofabrication technique to achieve this physical isolation differ, and can utilize either topside silicon under-etching [17, 39], or backside substrate etching [62]. When isolated from the substrate, tuning powers of 2.4 mW/FSR [17], 3.9 mW/FSR [62], and 4.9 mW/FSR [39] were demonstrated, a magnitude of order improvement in tuning efficiency.

These record-breaking results in tuning efficiency are ideal for applications where microring-based devices have to abide by strict power consumption requirements. However, the etch removal of the substrate may not be compatible with certain silicon photonic implementations, albeit, impressive progress has been made in extending undercut structures at larger scales [71]. Additionally, a consequence of the thermal isolation is that the thermal time constant is drastically increased, as high as $\sim$170 μs [17]. This may not be a critical parameter however, as environmental temperature fluctuations are likely to be above the $\sim$ms regime [72], making undercut integrated heaters appropriate for thermal stabilization systems. However, it should be noted that increasing the thermal impedance of the microring resonator renders it more susceptible to optical bistability effects, which can have deleterious effects on microring modulators at sufficiently high optical input powers [73, 74].

1.3.2.2 Methods for Control-based Solutions

In order for an integrated heater to effectively stabilize the temperature of a microring resonator it must be interfaced with control circuitry. The goal of the control circuitry

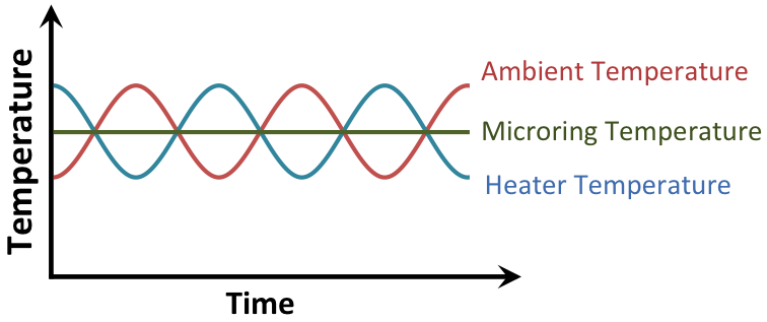

Figure 1.13: Heuristic graphic illustrating the counterbalancing of the heat generated by the heater against ambient temperature changes in order to keep the localized region of the microring under constant temperature.

is to dynamically counter-tune the integrated heater against thermal fluctuations in the ambient environment in order to maintain the local temperature of the microring at a constant temperature (see illustration in Fig. 1.13). In addition to thermally stabilizing the microring resonator, this control circuitry should be able to initialize the optical link by aligning the relevant microring resonators with their corresponding laser wavelengths (a process known as wavelength locking).

The general scheme of this control system would be to utilize some sensing mechanism to ascertain thermal drifts in the microring, denoted as an error signal, and a close-looped feedback controller to condition the error and adjust the voltage on the integrated heater. The feedback controller in any implemented control system is likely to be some digital or analog manifestation of a proportional-integral-derivative (PID) controller, a robust and simple method of achieving closed-loop feedback control.

However, there is no clear consensus as to what the best method to monitor the drift of the microring resonator is. The ideal solution is one that is low-cost and energy-efficient, does not require additional photonic structures, is compatible with the WDM implementation of microring resonators, immune to fluctuations in laser power, and implementable for either passive microring resonators or active components such as microring modulators.

Direct monitoring of the microring resonator temperature has been demonstrated [75], however, temperature sensors may be too slow and they have not yet been demonstrated working successfully in a control system. Rather, the predominant solutions

rely on indirectly monitoring drifts in the microring resonator. For instance, one example utilizes an infrared camera to image scattered light, however, this method will likely be difficult to scale and implement in a cost-effective and compact manner [76].

Several methods utilize the optical power of the signal to infer drifts in the microring resonator. It was shown that wavelength locking and stabilization could be achieved by algorithmically searching for the point of minimum power transmission of a passive microring resonator [77]. While effective, it remains to be seen whether the FPGA-implementation can be translated to simple low-power circuitry, and additionally, the technique may be vulnerable to Fabry-Perot artifacts in the optical path.

A method that is applicable specifically to microring modulators is to directly monitor the bit-error-rate (BER) of the generated data stream [78]. Demonstrated results showed wavelength locking and thermal stabilization of the modulator over a range of 32 K. By directly monitoring and optimizing the BER of the modulator the method controls microring modulator drift according to the most important application metric: the quality of the generated data.

However, monitoring of the BER is a complex procedure, requiring pattern-matching circuitry and high-speed receivers. Essentially, this requires duplicating the receive chain at the transmitter itself, which has consequences on the ease of implementation and overall power-consumption of the system. In addition, this method is only applicable to microring modulators, not microrings implemented as switches or filters.

As will be elaborated on in further detail in this dissertation, the difficulty in finding an efficient and straight-forward method for wavelength locking and stabilizing resonators is a result of the symmetry of the microring's optical resonance. A similar engineering problem is faced when the locking the wavelength of a laser to a fixed reference gas cavity, which also possesses a symmetrical optical resonance. For that scenario, the common and established method has been to create an anti-symmetric error signal (a derivative of the optical response) centered about the resonant wavelength [79]. Similarly, the generation of an anti-symmetric error signal would greatly ease the task of locking and stabilizing microring resonators.

One method to produce this desired error signal is to place the microring in an interferometric structure and utilize homodyne detection [80]. While meeting many metrics of the ideal solution, such as its simplicity and WDM compatibility, the introduction

of the interferometric structure may be difficult to implement with some configurations of microring resonators, such as more complicated microring switch routers [15].

1.4 Scope of Thesis

The work in this dissertation is focused on implementing control-based solutions to resolve the thermal and fabrication susceptibilities of microring-based devices.

As opposed to the control-based solutions highlighted in section 1.3.2.2, the control systems demonstrated in this work will be shown to form a comprehensive and complete solution. The chapters that follow form a narrative that introduce and demonstrate elegant methods that can be argued to meet the aforementioned metrics: low-cost and energy-efficient, does not require additional photonic structures, is compatible with the WDM implementation of microring resonators, immune to fluctuations in laser power, and implementable for either passive microring resonators or active components such as microring modulators.

Specifically, chapter 2 will introduce the application of power monitoring for thermally stabilizing microring modulators. Chapter 3 will continue to advance the technique by demonstrating power monitoring using integrated on-chip components.

Recognizing the specificity of power monitoring to microring modulators, chapter 4 introduces the use of dithering signals for the general solution of wavelength locking and stabilizing microring resonators. Characteristics of this technique, such as its ability to achieve μs-scale wavelength locking, are also elaborated in detail in chapter 4. Chapter 5 continues the narrative by showing how the use of dithering signals can be scaled to wavelength lock a WDM microring resonator demultiplexer. In chapter 6, the dithering mechanism is adapted to a 1×2 microring switch, demonstrating the switch's thermally stable operation over fluctuations as high as 20 K. Additionally, chapter 6 also proposes methods to scale such a control system to cover high-radix microring switches. Finally, chapter 7 expounds on the additional utility of the developed control systems for use in microring sensing applications.

Additionally, appendix C and D detail the intermodulation crosstalk and phase modulation characteristics of microring modulators, respectively. Work performed during the author's tenure, and relevant to to the study of microring-based devices, but falling outside the immediate scope of the narrative in this dissertation.

Chapter 2

Optical Power Monitoring for Thermally Stabilizing Microring Modulators

This chapter reviews the author's initial work on demonstrating a thermal stabilization system for a microring modulator. The control system was enabled by the use of optical power monitoring to track temperature fluctuations in the local environment of the microring modulator. Rigorous testing using eye diagrams and bit-error-rate (BER) measurements were used to validate the efficacy of the control system.

Notable contributions of this work:

- The general methodology of a closed-loop control system to thermally stabilize a microring-based device.
- The adaptation of optical power monitoring to a microring modulator for the purpose of ascertaining temperature drifts.
- Creation of a thermal test environment using a high-power external visible laser that allows the generation of thermal fluctuations without disrupting optical coupling.
- Demonstration of error-free operation of a 10-Gb/s microring modulator while is it being subjected to thermal fluctuations that would normally render it inoperable.

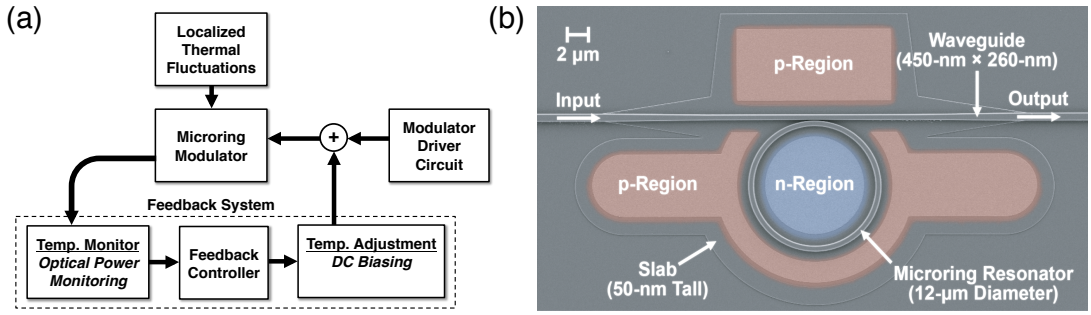

Figure 2.1: (a) Schematic outlining the testing and implementation of the control system for thermally stabilizing the microring modulator. (b) Scanning-electron-microscope (SEM) image of the microring modulator.

2.1 Developing a Closed-Loop Control System

In this work a general methodology to thermally stabilize a microring-based device using a closed-loop control system was first introduced. As depicted in Fig. 2.1(a), such schemes require a monitor for observing temperature drift, a mechanism to adjust the temperature accordingly, and a feedback controller to maintain closed-loop operation of the system. Using the techniques of optical power monitoring and bias tuning, we experimentally show that this general dynamic is sufficient to maintain the high data-rate performance of a silicon microring modulator under temperature conditions that would normally render it inoperable

The silicon microring modulator (capable of 10-Gb/s modulation) used to demonstrate the control system was fabricated at the Cornell Nanofabrication Facility. As pictured in Fig. 2.1(a), the device consists of a 6-μm-radius microring side-coupled to a waveguide. The microring and waveguide are designed for quasi-TE mode using a width and height of 450 nm and 260 nm, respectively. A 50-nm Si slab surrounding the microring was doped accordingly to produce the *p-i-n* structure capable of injecting carriers into the microring, which is necessary to produce the high-speed resonance shift required for optical modulation. Further fabrication details can be found in [61]. The thermal sensitivity of the resonance is given by Eq. 1.3. With a group index of $\sim$4 [61], the microring modulator has a TDWS of 0.07 nm/K.

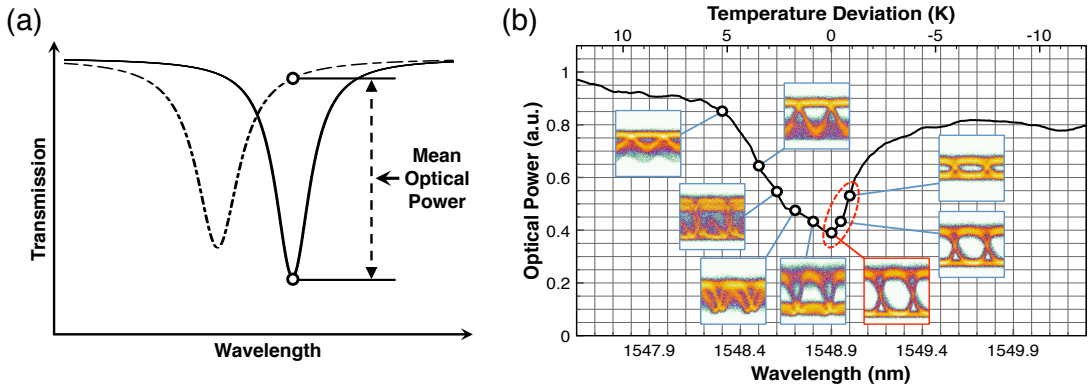

Figure 2.2: (a) The mean optical power is given as half of the power between the two bit-states of the modulated response. (b) Measured mean optical power of the 10-Gb/s microring-modulated optical signal versus wavelength. Eye diagrams of the 10 Gb/s signal are incrementally shown at points on the wavelength scan. The top x-axis gives the equivalent range when sweeping the temperature.

2.1.1 Optical Power Monitoring

Optical power monitoring is an established technique commonly used in telecommunication systems. Specifically, for traditional MZMs, power monitoring can help stabilize the DC bias required for proper OOK modulation. However, as previously espoused, the functionality of microring-based devices is dramatically different from traditional standing-wave devices such as the MZM.

An initial step in implementing the full control-system described prior was to first confirm that the optical power monitoring was valid for microring modulators. As Fig. 2.2(a) illustrates, the mean optical power is an average between the power in the one and zero bit-states of the microring modulation. The suitability of optical power monitoring was studied by measuring the mean optical power of the generated data signal as the wavelength of the laser was swept (Fig. 2.2(b)). Eye diagrams of the 10-Gb/s optical signal were also recorded at incremental wavelengths, and are shown inset in Fig. 2.2(b). While this measurement was done by sweeping the wavelength, an identical result will be produced by sweeping the temperature, which has been charted on the top axis of Fig. 2.2(b).

The dashed red region of Fig. 2.2(b) indicates a region of wavelengths (or equivalent temperature deviation) where suitable OOK is generated for data transmission.

This monotonically increasing slope can be used to detect changes in the temperature of the microring modulator. Increases or decreases in the received optical power indicate corresponding decreases or increases, respectively, of the temperature at the modulator. This measurement confirmed that optical power monitoring could be exploited by initially aligning the wavelength of the laser to a point on the middle of the aforementioned slope.

Because this method requires only the mean power of the optical signal, the photodetector used to monitor the signal can have a much smaller bandwidth than the GHz-rate optical signal it is monitoring. Subsequently, this monitoring mechanism is more opportune to be energy-efficient because the bandwidth of the slow photodetector used can be matched to the bandwidth of the thermal fluctuations afflicting the microring modulator. Additionally, only a small tap of the optical power is required to ascertain the mean power of the signal, minimizing the insertion loss added by the monitoring system. Lastly, it should be noted that this method operates on the assumption that over a large data set, the ratio of '1' bits to '0' bits does not change. For instances where this may not be a necessarily safe assumption, encoding schemes such as 8b/10b or 64b/66b can used to guarantee a DC-balanced data stream [81].

2.1.2 Thermal Tuning using Carrier-Injection Biasing

As per the aforementioned control system (Fig. 2.1(a)), once a deviation in temperature has been established, the temperature must be adjusted back to its normative value. In section 1.3.2.1, it had been elaborated that integrated heaters were the ideal method for controlling the local temperature of the microring resonator. While this is true, for this demonstration there was no integrated heater built into the device, and the alternative method of bias-tuning was used as a substitute.

Bias tuning is performed by adjusting the bias voltage (and subsequently the current) of the electrical signal driving the microring modulator. In carrier-injection microring modulators a small forward bias current is necessary to attain optimum optical modulation [82]. Due to the significant amounts of heat generated by carrier recombination in the diode junction, the forward bias current has the ancillary effect of altering the temperature of the microring modulator. Hence, the bias current can be reduced or increased to cool or heat, respectively, the microring, thus counteracting thermal fluctuations in the ambient environment [83].

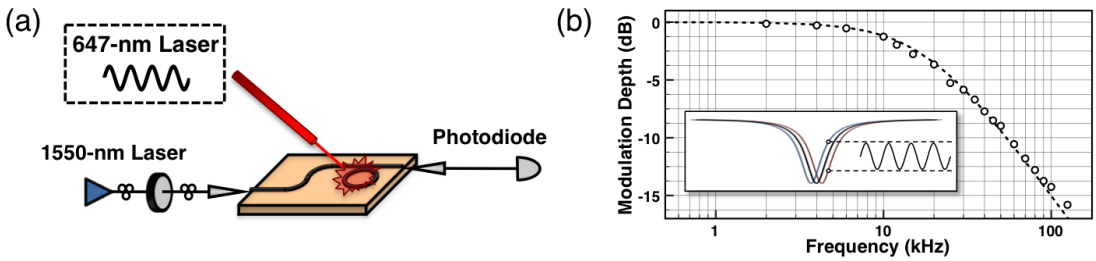

Figure 2.3: (a) Generation of thermal fluctuations using a visible laser. (b) Measured bandwidth of the thermal fluctuations produced by the visible laser.

2.1.3 PID controller

As shown in Fig. 2.1, closed-loop operation of the control system requires a feedback controller. In this demonstration, an analog proportional-integral-derivative (PID) controller was implemented. Because the signal coming off the power monitor is slow-speed, and subsequently the temperature adjustment is also slow-speed, the controller can be implemented using relatively slow-speed components. The slow-speed analog circuitry composing the feedback controller consisted of op-amps with a bandwidth of 3 MHz and an instrumentation amplifier with a bandwidth of 20 MHz.

2.2 Generation of Test Thermal Fluctuations

The evaluation of our feedback system requires the ability to dynamically inflict temperature changes on the microring modulator, akin to what the modulator would experience in a thermally volatile microelectronics environment. A traditional experimental setup would utilize a thermo-electric cooler (TEC) to produce the desired effect. However, TECs can be limited in bandwidth, and more importantly, heating and cooling of the entire nanophotonic chip will result in expansion and contraction of the entire chip, and subsequently, optical decoupling when using lateral fiber coupling. To resolve these issues, for this experimental demonstration a high-power multistripe 647-nm visible laser was used to inflict thermal fluctuations on the microring modulator. As depicted in Fig. 2.3, a cleaved multi-mode fiber is shone vertically on the microring modulator. Transparent to SiO_2, the 647-nm light is able to pass through the SiO_2 cladding after which it is absorbed by the silicon layer in the localized region of the microring modulator.

Through internal sinusoidal modulation of the 647-nm laser, a thermal fluctuation is produced in the localized vicinity of the microring modulator. Because the thermal fluctuation is localized to the microring modulator, the coupling of optical power into the chip is not affected, thereby enabling the use of optical power monitoring.

To characterize the bandwidth of this technique a CW-laser was coupled into the modulator chip while the modulator was in its passive state, and the laser wavelength was tuned to the modulator's resonance (Fig. 2.3(a)). The 647-nm laser was modulated with a sinusoid, while the output of the chip was received on an appropriate photodiode. The modulation produced on the photodiode (from the thermal modulation of the resonance) was measured for frequencies up to 100 kHz (Fig. 2.3(b)). It was found that the thermal modulation has a bandwidth of 18 kHz. 18 kHz is the modulation bandwidth of the 647-nm laser used for the experiment, indicating that the visible laser technique is not bandwidth-limited in the tested frequency regime (5 kHz).

The one disadvantage of using a high-power visible laser is its mode-hopping behavior stemming from the large modulation of the laser current. This results in small but fast discontinuities in the modulation of its optical power, which then produces small but fast thermal fluctuations in the localized region of the microring resonator. Since the control systems in our demonstration are designed for a certain frequency range, often implementing low-pass filters to shield from external electrical noise, it can not contend with these small but fast thermal fluctuations. As will be seen, while our implemented control systems will be able to correct for the large thermal fluctuations we induce, there will be resultant power penalties from not being able to contend with these thermal fluctuations from the mod-hopping behavior of the visible laser.

2.3 Demonstration of the Control System

Our experimental setup to test the implemented control system is illustrated in Fig. 2.4. A pulsed-pattern-generator (PPG) was used to generate a 10-Gb/s non-return-to-zero (NRZ) 2^7-1 pseudo-random bit sequence (PRBS) electrical signal. The 1.1-Vpp signal was biased at 0.4 V and conditioned with a pre-emphasis circuit to enable high-speed operation of the device [82]. A CW tunable laser was set to TE polarization before being launched onto the chip with a power of 15 dBm. Waveguide and coupling losses yielded a fiber-to-fiber loss of 33 dB. The OOK modulation produces additional

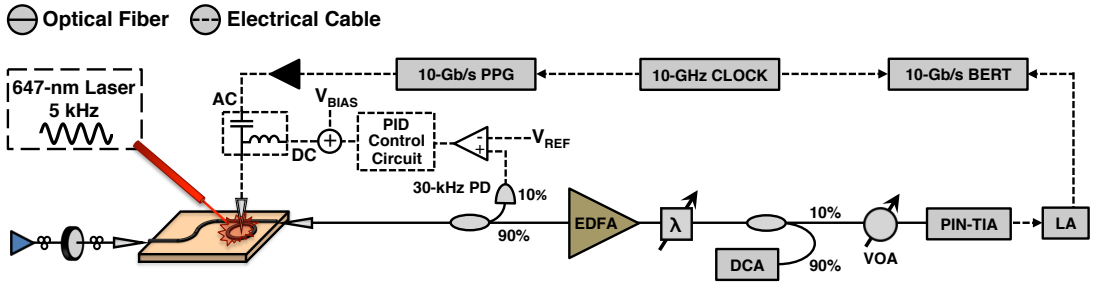

Figure 2.4: Experimental setup used to test our implemented control system.

loss, yielding a recovered power ranging from −21 dBm to −18 dBm, depending on the depth of the modulation. 10% of this microring-modulated signal was tapped for the power monitoring. The remaining signal is then amplified and filtered before being sent to a PIN-TIA photodetector followed by a limiting amplifier (LA). A bit-error-rate tester (BERT) and variable optical attenuator (VOA) are used in conjunction for the BER measurements.

As 2.4 illustrates, and as previously described, a visible laser is used to inflict thermal fluctuations in the region of the microring modulator. Using an optical spectrum analyzer, we map the passive resonance shift to the visible laser at varying powers, in order to determine the magnitude of the temperature change the microring modulator is experiencing. From that data, we can ascertain the magnitude of the thermal fluctuations at the microring modulator. In the first trial thermal fluctuations of magnitude 6 K are generated. In the second trial, the system is further stressed by increasing the thermal fluctuations to 12 K. In both instances, the operating wavelength and visible laser power are set such that the temperature of the microring modulator both increases and decreases relative to its ideal operating temperature.

The portion of the 10-Gb/s optical signal tapped for power monitoring is received on a photodiode with a bandwidth of 30-kHz. With its limited bandwidth, the photodiode acts as an effective monitor of the mean power in the 10-Gb/s optical signal. The voltage generated on the photodiode is compared to a reference voltage using an instrumentation amplifier (20-MHz bandwidth). The error signal is then relayed to an analog PID controller composed of op-amps (3-MHz bandwidth). The feedback signal is then added to the bias voltage using a standard op-amp summing circuit.

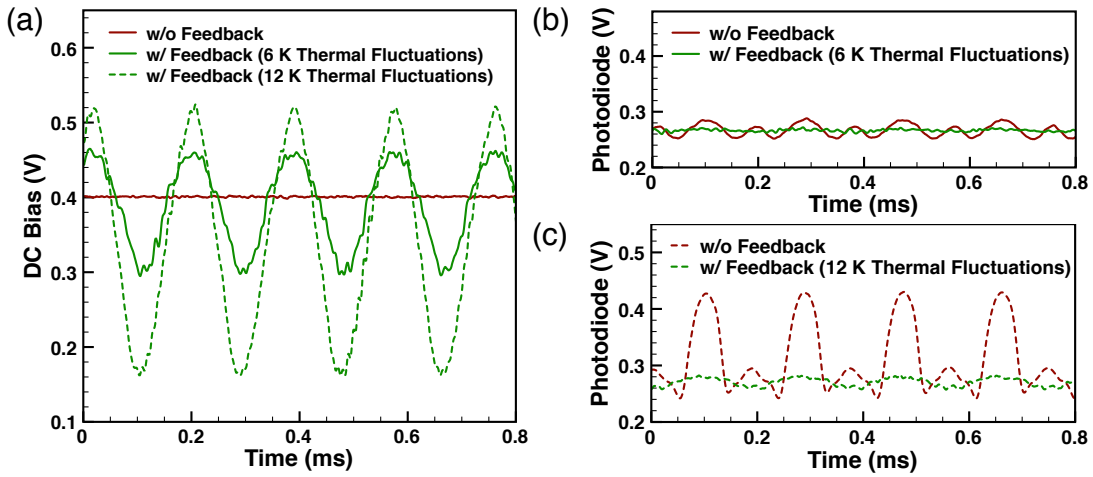

Figure 2.5: (a) The DC bias of the modulator, demonstrating how the feedback system dynamically adjusts the DC bias to counteract thermal fluctuations of magnitude 6 K and 12 K. (b) The voltage from the TIA following the photodiode (used to monitor the optical power) when the modulator is exposed to thermal fluctuations of magnitude 6 K, with and without the feedback system implemented. (c) The voltage on the TIA following the photodiode when the modulator is exposed to thermal fluctuations of magnitude 12 K, with and without the feedback system implemented.

The dynamic adjustment of the DC bias is illustrated in the oscilloscope trace of Fig. 2.5(a). Without the feedback circuit, the DC bias is set at a constant 0.4 V, whereas, with the feedback circuit, the voltage is swung dynamically to correct for the thermal fluctuations. Fig. 2.5(a) shows the system when it is subjected to both 6-K and 12-K thermal fluctuations, with the DC bias swing larger (from 0.15 V to 0.50 V) for the latter scenario. The effect of this action can be seen in the voltage of the transimpedance-amplifier (TIA) following the photodiode (Fig. 2.5(b), 2.5(c)), which is an indication of the mean power in the 10-Gb/s optical signal. Without the feedback system the mean power fluctuates in correspondence with the thermal fluctuations. The feedback system locks the mean modulation power to the set reference, ensuring that the modulation is maintained throughout the duration of the thermal fluctuations.

The eye diagrams in Fig. 2.6 and bit-error-rate (BER) curves in 2.7 provide validation of the control systems functionality. Fig. 2.6(a) and 2.6(d) show eye diagrams of the microring-modulated optical signal when there are no thermal fluctuations, without and with the control system implemented, respectively. In this scenario, the eye

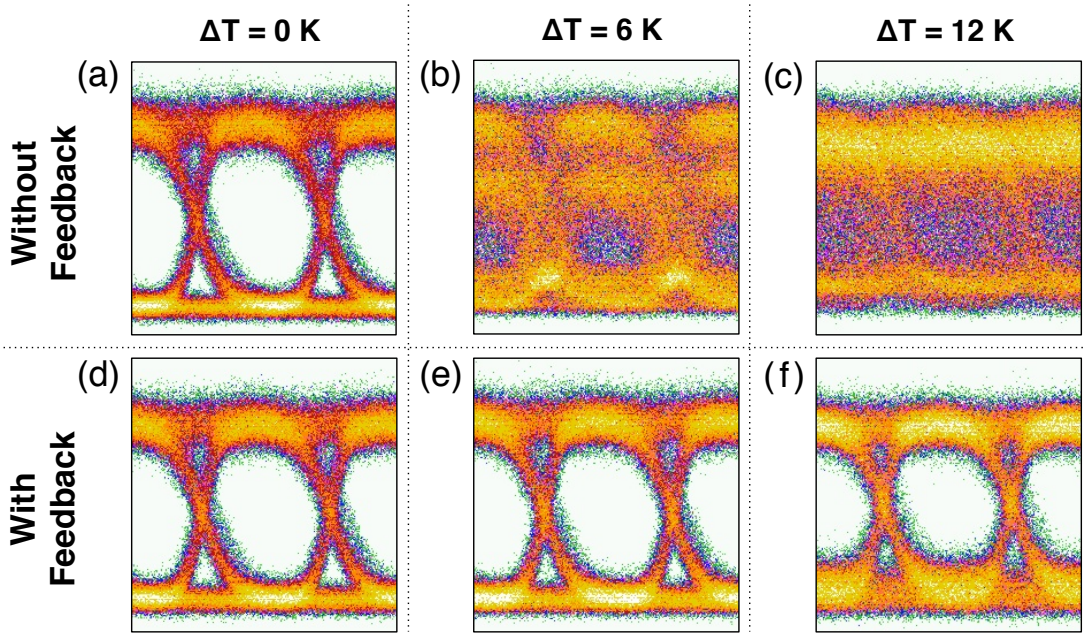

Figure 2.6: Eye diagrams of the 10-Gb/s microring modulation when subjected to temperature fluctuations of magnitude (a) 0 K (b) 6 K (c) and 12 K with no implemented control system. Similarly, eye diagrams of the 10-Gb/s microring modulation when subjected to temperature fluctuations of magnitude (d) 0 K (e) 6 K (f) and 12 K but with no control system thermally stabilizing the microring modulator.

diagrams show similar modulation performance, and furthermore, the measured BER curves of Fig. 2.7 show only a power penalty of 0.6 dB as a consequence of implementing the control system. This power penalty can be attributed to the operation of the microring modulator at a modulation point that, while optimal for the control system, is not optimal for the generation of optical data. It should be noted that the reference level was set to minimize this power penalty while ensuring that there was enough of a margin for the feedback system to operate successfully.

In Fig. 2.6(b) and Fig. 2.6(c) the eye diagram is shown for when the modulator is subjected to thermal fluctuations of 6 K and 12 K, respectively, and without the control system implemented. With thermal fluctuations of 6 K, the ensuing resonance shifts are severe enough that the data in the optical signal becomes severely distorted (Fig. 6(b)). When the thermal fluctuations are increased to 12 K, the distortion becomes further exacerbated, with the majority of the optical power contained at the '1' level, as the

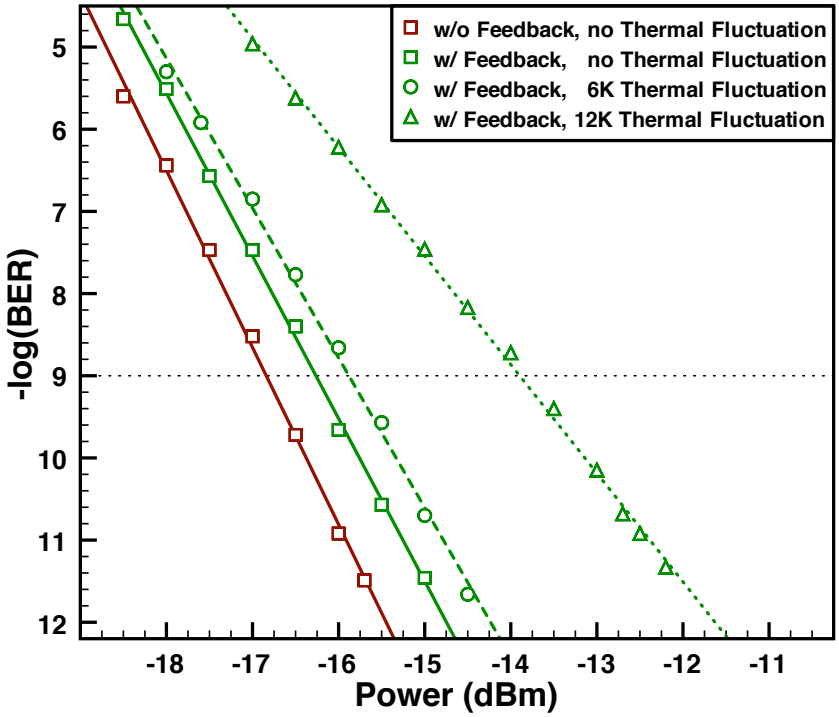

Figure 2.7: BER measurements of the 10-Gb/s microring-modulated signal. These measurements correspond to the eye diagrams in Fig. 2.6(a), 2.6(d), 2.6(e), and 2.6(f).

modulator is shifted completely out of the modulation region for a significant portion of the thermal fluctuation (Fig. 2.6(c)). For both scenarios, the optical data is distorted to a degree that no BER measurement is possible.

In contrast, Fig. 2.6(e) and Fig. 2.6(f) show that with the implementation of the control system, the modulation of the microring modulator can be maintained, even when subjected to thermal fluctuations of 6 K and 12 K, respectively. BER measurements further validate this result with error-free performance (defined as a 10^{-12} error-rate) being measured when the feedback system is implemented (Fig. 2.7).

Although the feedback system is able to maintain error-free performance in the presence of the aforementioned thermal fluctuations, there were power-penalties incurred as the magnitude of the thermal fluctuations was increased. With thermal fluctuations of magnitude 6 K a power penalty of 0.4 dB is measured relative to the scenario with no thermal fluctuations (and with the feedback system implemented). When the thermal fluctuations are increased to a magnitude of 12 K this power penalty increases

to 2.4 dB. These power penalties are evident in the eye diagrams of Fig. 2.6(e) and Fig. 2.6(f). As the magnitude of the thermal fluctuations increase the noise in the '1' and '0' levels also increase. This behavior is partially attributed to the mode-hopping behavior of the visible laser generating the thermal fluctuations (see section 2.2), it is also attributable to the DC biasing mechanism used for maintaining the temperature of the microring. The carrier dynamics of the microring modulator are sensitive to adjustments in the DC bias. As a result, even the small changes in DC bias caused by the feedback system produce distortions in the modulation of the microring modulator. As the thermal fluctuations increase in magnitude the feedback system responds by applying larger variations to the DC bias, incidentally producing more distortion in the modulation of the modulator, and an ensuing increase in power penalty.

2.4 Conclusion

The work described in this chapter established and demonstrated the general methodology for thermally stabilizing a microring modulator using a closed-loop control system. The most notable contribution of this work was in showing that error-free performance of a microring modulator could be achieved even in the midst of thermal fluctuations, thus showing that the thermal challenges facing microring-based devices could be resolved without resorting to athermal solutions.

The creation of a thermal testbed (using the visible laser) was an important achievement, allowing the testing of the control system when inflicted with real thermal fluctuations, and as will be seen, would continue to be used in the validation of future implemented control systems.

Finally, the use of optical power monitoring as applied to microring modulators was an important innovation, demonstrating a technique that will likely continue to be used in the future for both its simplicity and efficacy. As a testament to its capability, other researchers were able to use of optical power monitoring for stabilizing microring modulators, in this case, with a sophisticated pairing of custom CMOS circuitry with a silicon microring modulator [84].

While this demonstration served as an important proof-of-principle demonstration there were still a number of ways in which the control system could be improved. As was previously described, while the use of DC biasing was effective, it was limited in its

temperature tuning range when compared to the use of an integrated heater. Furthermore, in our demonstration we had used an optical split and external photodetector to monitor the optical power of the generated data-signal. To demonstrate the validity of this technique for future silicon photonic interconnects, it must be demonstrated with integrated photodiodes.

Chapter 3

Integrated Thermal Stabilization of a Microring Modulator

The work in this chapter builds upon the accomplishments of the work presented in chapter 2 by integrating the optoelectronic components used to thermally stabilize the microring modulator. Specifically, instead of DC bias tuning (with its limited tuning range), an integrated heater is used. Additionally, instead of using an off-chip photodetector, an integrated silicon photodiode is used to implement the power monitoring technique. These integrated components are tied together using a control system that separates the high-speed generation of data from the low-speed thermal stabilization of the microring modulator.

Notable contributions of this work:

- Incorporation of an integrated photodiode and integrated heater into a closed-loop control system to thermally stabilize a microring modulator.
- Demonstration of receiving 10 Gb/s data using a defect-enhanced silicon photodiode.
- Demonstration of the efficacy of a defect-enhanced silicon photodiode for the power-monitoring method.
- Demonstrated WDM-compatible control system through the use of the microring drop port for power monitoring.

3.1 Defect-Enhanced Silicon Photodiodes

While germanium and III-V photodetectors are typically considered the default choice for use as photodetectors in silicon photonic platforms, we have done notable work demonstrating the utility of defect-enhanced silicon photodetectors. Through the use of ion implantation, silicon can be embedded with sub-bandgap defect states, increasing its C-band photoresponsivity, a spectral region where it is normally transparent. Leveraging the high modal confinement of SOI waveguides, Si^+ implanted waveguide photodetectors have been demonstrated with a bandwidth of > 35 GHz and responsivities of 0.5 to 10 A/W [85]. These defect-enhanced silicon photodiodes have comparably high responsivities (Ge photodetectors typically range from 0.8 to 1 A/W [86]), but have a significantly lower absorption coefficient, resulting in a relatively efficient, but weak, photodetector. Defect-enhanced silicon photodetectors for data reception must be considerably longer than Ge or III-V photodetectors, with the increased capacitance hindering the bandwidth of the photodetector. Despite these disadvantages, there remains the advantage of simplicity in fabrication (both in patterning, and avoiding the introduction of new materials) that makes defect-enhanced silicon photodiodes extremely attractive for use on the silicon photonic platform.

Tangent to our work on control systems, we performed the first validation of defect-enhanced silicon photodetectors for use in receiving high-speed data. The Si^+ ion-implanted silicon waveguide *p-i-n* photodetectors used in the characterization were fabricated on the CMOS line at MIT Lincoln Laboratory, as described in [87], with dimensions given in Fig. 3.1(a). The eye diagrams in Fig. 3.1(c) depict the received optical data (at 2.5 Gb/s and 10 Gb/s) for device lengths of 250 μm and 3 mm. BER measurements verified error-free operation of the silicon photodetectors for both 2.5 Gb/s and 10 Gb/s.

While our work validated the use of defect-enhanced silicon photodetectors for high-speed data reception, an additional (and arguably more important) utility of defect-enhanced silicon photodetectors is in their use as in-situ optical power monitors [88]. This work incorporates silicon photodetectors to yield an integrated power monitoring solution that lends itself to ease-of-fabrication.

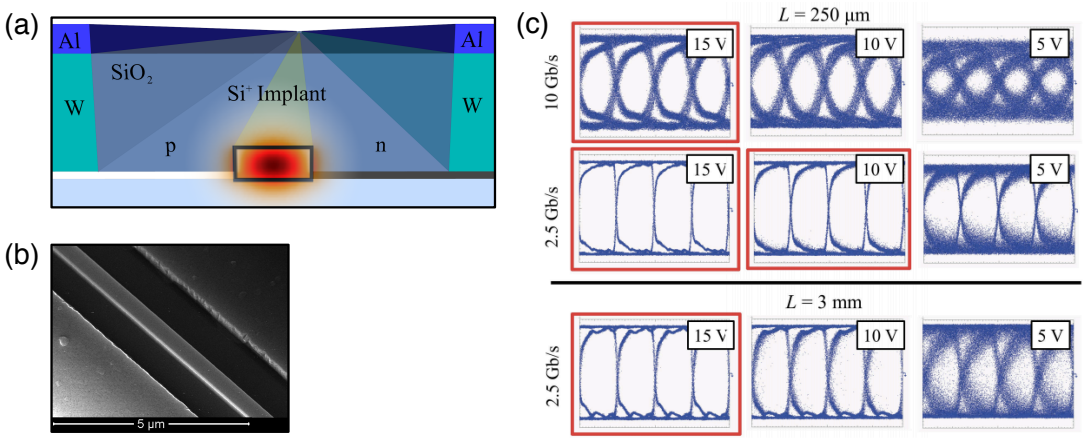

Figure 3.1: (a) Cross-section of the silicon waveguide photodetector. The channel waveguide section is Si^+ ion implanted, while the wings are doped p and n to form a p-i-n photodiode. The fundamental quasi-TE mode is overlaid. (b) SEM image of the silicon waveguide photodetector. (c) Eye diagrams for the $L = 250$ μm and $L = 3$ mm devices for 5 V, 10 V, and 15 V reverse biases (taken after a TIA-LA). Red outlines signify error-free operation.

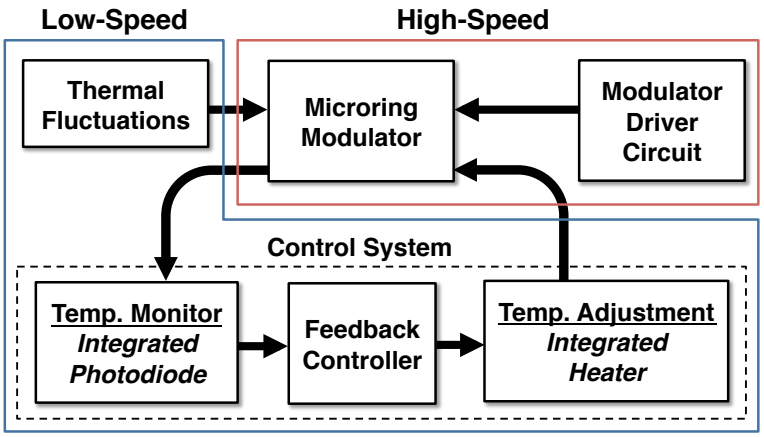

Figure 3.2: Schematic of the control system, highlighting the separation of the high-speed data transmission from the low-speed stabilization of thermal fluctuations.

3.2 A Control System using Integrated Components

In contrast to the initial control system introduced in Chapter 2 (Fig. 2.1(a)), this implemented control system (depicted in Fig. 3.2) separates the low-speed thermal stabilization from the high-speed data generation. This is important both for preserving

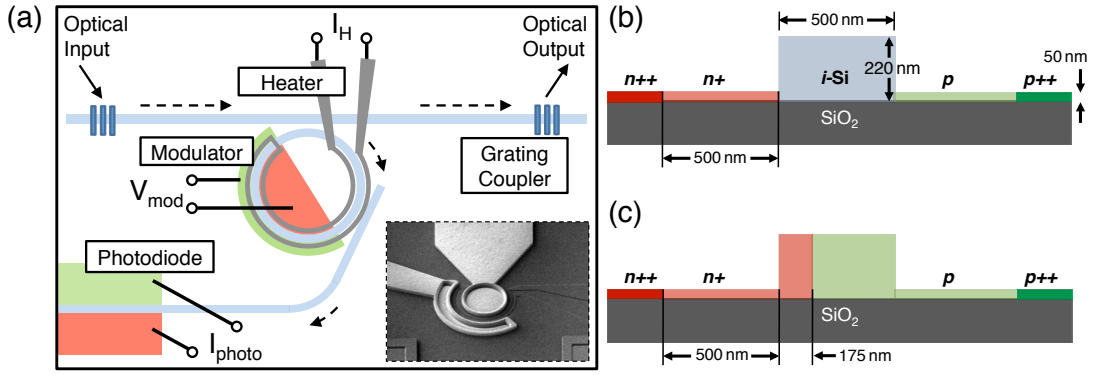

Figure 3.3: (a) Schematic of the integrated device (not to scale), and SEM image of fully processed device (inset). Waveguide geometry and doping profile for the (b) defect-enhanced silicon photodiode and (c) depletion-mode microring modulator.

the integrity of the data, but also for creating an energy efficient control system.

As highlighted in section 3.1, the use of a defect-enhanced silicon photodiode enables all the optoelectronic components to be integrated onto a single device using CMOS-compatible processes and materials. Fabricated at Singapore's IME, the layout of the integrated device is shown in Fig. 3.3(a), and consists of a depletion-mode microring modulator, with a thin film heater directly above it, and a defect-enhanced silicon photodiode on the drop port. Holographic gratings of 70-nm etch depth are employed to facilitate coupling of C-band wavelengths into and out of the chip. The ring is 15 μm in radius, and has a 210 nm point-coupling gap to the input and drop port waveguide. The cross-section of the photodiode and modulator are shown in Fig. 3.3(b) and 3.3(c), respectively. The waveguides are 500 nm wide and 220 nm in height, and etched to a depth of 170 nm. The modulator is formed of an n^+p junction that takes up one-half of the ring circumference. The p-side of the junction is composed of a uniform boron concentration of $5x10^{17}$ cm^{-3} and the n^+-side of the junction is composed of a uniform phosphorus concentration of $1x10^{18}$ cm^{-3}. The junction is offset by 75 nm from the center of the waveguide. The thin film heater is patterned on a 180-nm thick titanium-based layer separated from the active layer by 1.2 μm of oxide. The photodiode is 500 μm long, and consists of a p-i-n^+ junction formed laterally on the waveguide. The p and n^+ doping levels of the modulator are in this case aligned to the edge of the waveguide, leaving the core undoped. Sensitivity to sub-bandgap wavelengths was provided by deep

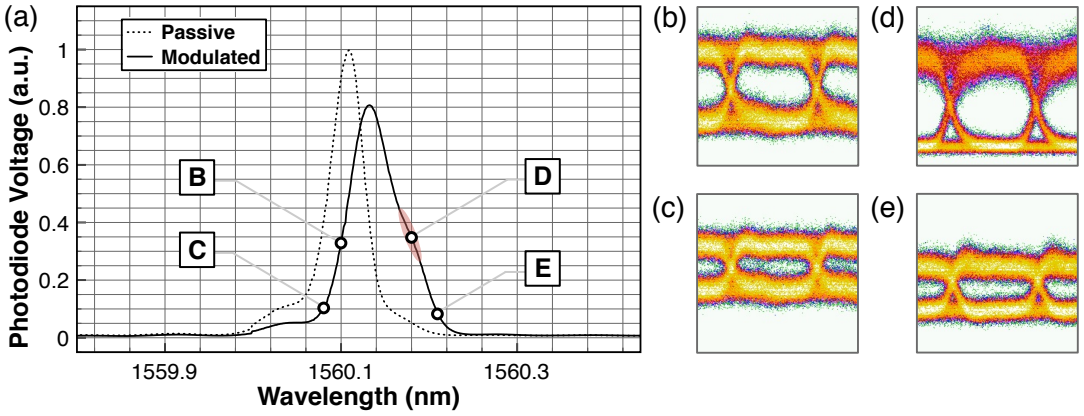

Figure 3.4: (a) Measured photoresponse of the drop port photodiode for when the microring is in its passive state, as well as for when it is modulated. (b-e) Generated 5-Gb/s eye diagrams as indicated at several points on the measured photoresponse of the modulated microring.

level lattice defects introduced by a masked phosphorus implantation of 300 keV and 1x10^{13} cm^{-2} dose followed by a 10 min anneal at 475 °C in a N_2 ambient. The damage implantation and anneal was performed directly prior to the metal heater deposition in the process flow.

Positioned on the drop port of the microring modulator, the silicon photodiode is utilized as the photodetector neccessary to monitor the mean optical power of the modulated signal. This configuration avoids the use of a power tap and is compatible with the wavelength-division-multiplexed (WDM) arrangement of microring modulators, in which several microrings are multiplexed along the same waveguide bus. Fig. 3.4(a) shows the photoresponse (voltage produced after the TIA) of the silicon photodiode when the modulator is in its passive (dotted) state and when the modulator is actively modulated data (solid). Also indicated in Fig. 3.4(b)-(e) are the eye diagrams of the generated data at several points on the photoresponse curve.

3.3 Demonstration of the Integrated Control System

Our experimental setup to test the implemented control system is illustrated in Fig. 3.5(a). A pulsed-pattern-generator was used to generate a 5 Gb/s NRZ 2^7-1 PRBS electrical signal (we had previously demonstrated the system with 2^{31}-1 PRBS as well).

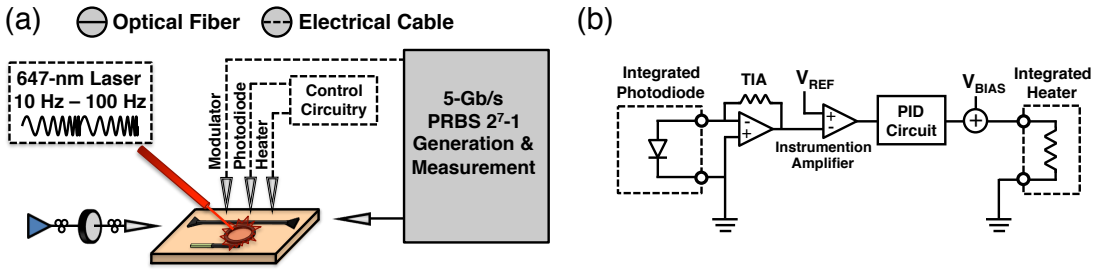

Figure 3.5: (a) Experimental setup used to test our implemented control system. (b) Circuitry comprising the control system. Indicated in the dashed boxes are the on-chip integrated components.

This electrical signal was amplified to 5 Vpp and biased at −5 V to drive the microring modulator using high-speed electrical probes. A separate set of low-speed electrical probes was used to contact the heater and silicon photodiode. A CW tunable laser was set to TE polarization before being launched into the grating coupler with a power of 3 dBm. The microring-modulated 5 Gb/s optical signal was recovered from the exit grating coupler for BER measurements and eye diagrams.

As previously detailed in section 2.2, the localized region of the microring modulator was excited from above by a 647-nm visible laser to generate thermal fluctuations. The power of the visible laser was internally modulated from 10 Hz – 100 Hz to generate ensuing thermal fluctuations of the same frequency, and of magnitude 3 K, in the region of the microring modulator.

As Fig. 3.5(a) shows, the operation of the control system occurs independent of the high-speed operation of the microring modulator. Fig. 3.5(b) outlines the control circuitry, including the interface between the circuitry and the on-chip integrated photodiode and heater. As previously mentioned, the silicon photodiode is used to ascertain changes in the mean power of the modulated optical signal. The photodiode current is fed into an op-amp transimpedance-amplifier (TIA) circuit that produces a voltage corresponding to the amount of optical power received by the silicon photodiode. The transimpedance voltage generated from this arrangement is then compared to a reference voltage using an instrumentation amplifier. The resultant error signal is fed into a PID controller circuit. The PID controller circuit generates a feedback signal that is used to adjust the voltage on the integrated heater. A bias voltage (V_{BIAS} in

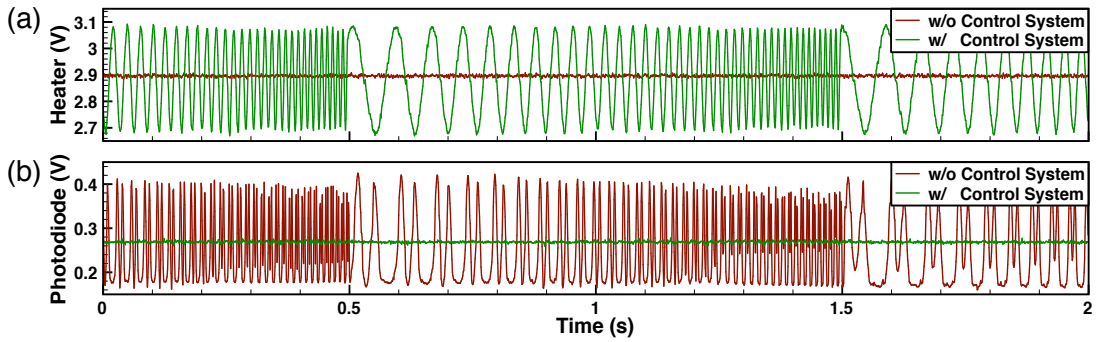

Figure 3.6: Oscilloscope measurements (with and without the control system) of the (a) voltage applied to the heater, and the (b) voltage generated from the photodiode (following the TIA) measuring the mean optical power in the generated data-signal.

Fig. 3.5(b)) is also used to set the microring modulators operating point to an initial wavelength.

Through the described mechanism, the integrated heater dynamically reduces current (cools down) in the presence of high ambient temperatures and increases current (heats up) in the presence of low ambient temperatures, thereby maintaining the temperature of the microring modulator at a set operating temperature throughout the duration of the thermal fluctuations inflicted by the visible laser.

The dynamic adjustment of the heater voltage is seen in the oscilloscope trace of Fig. 3.6(a). Without the control circuit, the heater voltage is set at a constant 2.9 V (an arbitrary voltage), whereas, with the control circuit, the voltage is swung dynamically between 2.7 V and 3.1 V to correct for the thermal fluctuations afflicting the microring modulator. The effect of this action can be seen in the transimpedance voltage from the photodiode (Fig. 3.6(b), which was used to measure the mean power of the optical signal in our control system. Without the control system the mean power fluctuates in correspondence with the thermal fluctuations. The control system locks the mean power to the set reference, ensuring that the modulation is maintained throughout the duration of the thermal fluctuations.

The resonance tuning efficiency of the integrated heater was measured to be 0.12 nm/mW. Utilizing a calculation of the group index of the waveguide, the thermal sensitivity of the resonance is 0.072 nm/K (8.9 GHz/K) (Eq. 1.3). From measuring the minimum and maximum voltage needed to thermally stabilize the microring modulator

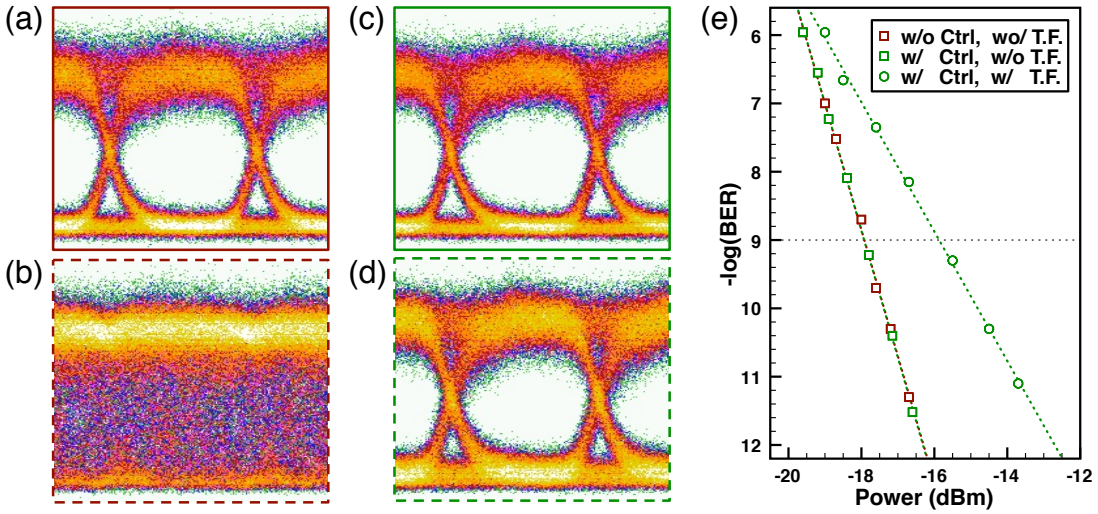

Figure 3.7: Eye diagrams of 5-Gb/s microring-modulated optical signal ***without*** the control system (Ctrl) in (a) a stable environment, and (b) under thermal fluctuations (T. F.). Similarly, the microring modulation ***with*** the control system in (c) a stable thermal environment, and (d) under thermal fluctuations. (e) BER measurements corresponding to eye diagrams in (a), (c), and (d).

(Fig. 3.6(a)), the magnitude of the temperature fluctuation is inferred to be 3 K. This was the maximum temperature fluctuation that we could generate using the visible laser. While this modest temperature fluctuation is enough to demonstrate the functionality of the stabilization system, it does not represent the full temperature range that the system would be able to correct for. The real limit on the temperature range of the system is the tuning range is the integrated heater, which we were able to routinely tune upwards of 50 K.

The eye diagrams and BER measurements in Fig. 3.7 validate the performance of the control system. Without the thermal fluctuations, there is a negligible difference between operating the microring modulator without control (Fig. 3.7(a)), and with control (Fig. 3.7(c)), further confirmed by the BER measurements in Fig. 3.7(e), which shows that there is no incurred power penalty as a consequence of operating with the control system. As seen in Fig. 3.7(b), subjection of the microring modulator to thermal fluctuations without corrective feedback tuning will result in complete failure of the modulation. However, as can be seen in Fig. 3.7(d), the control system can completely correct for the thermal disturbances, maintaining error-free modulation with

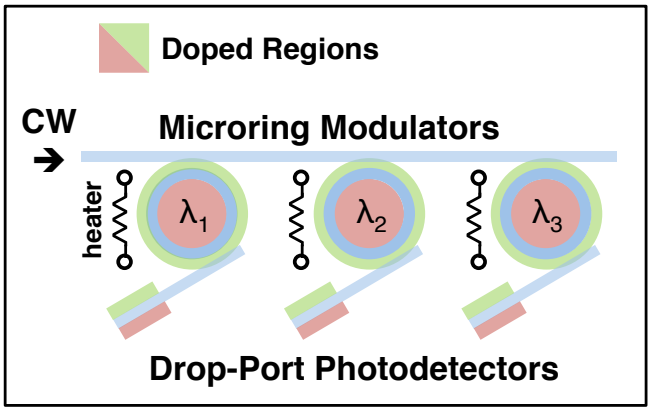

Figure 3.8: Typical arrangement of multiplexed microring modulators for WDM modulation. Individualized drop ports allow independent thermal stabilization of each modulator.

a power penalty of 2 dB (in comparison to the back-to-back case of Fig. 3.7(a)). As detailed in section 2.2, this power penalty is attributable to the constraints of the testing setup, specifically the mode-hopping behavior of the visible laser generating the thermal fluctuations.

3.4 WDM Compatibility

In our earlier work depicted in Chapter 2 a tap of the bus waveguide's output was used to implement the power monitoring technique. While effective for a single modulator, this method is not compatible with the typical multiplexed arrangement of microring modulators used for WDM interconnects. In contrast, the use of a photodiode on the drop port of the microring allows the optical power in each channel to be addressed independently, allowing for the independent thermal stabilization of each microring modulator in a WDM modulator bank (Fig. 3.8).

3.5 Energy Efficiency Analysis

For the successful implementation of this thermal stabilization system in commercial applications the system must adhere to the stringent power consumption requirements foreshadowed for future small-scale optical interconnects. These predictions project that in the most demanding environments, the justification for optical networks-on-chip

will require the aggregate power consumption for the optical link to be below ∼1 pJ/bit [20]. Less localized interconnects, such as the ones that will populate board-to-board or rack-to-rack interconnections will likely be less strict. To validate the feasibility of our demonstrated system, we project its power consumption if implemented with current leading technology.

As shown in Fig. 3.2, the thermal stabilization system is composed of sub-components, the first sub-component consisting of circuitry to extract the photodiode current and condition the feedback response, the second sub-component consisting of the resistive heater used to adjust the local temperature of the microring modulator.

For the integrated heater used in this device, we measured a DC resistance of 1340 Ω, and a tuning efficiency of 0.12 nm/mW (67 μW/GHz). This integrated heater was not optimized for tuning efficiency, and hence, has a relatively low tuning efficiency when compared to more recent literature (as was reviewed in section 1.3.2.1). For this reason, in our analysis we utilize the results of [69], in which an integrated heater was demonstrated to tune across 5 nm (64 K), using sub 1-V voltage, a tuning efficiency of 1.14 nm/mW (7 μW/GHz), and without compromising the performance of the 10-Gb/s microring modulator.

For analyzing the power consumption of the circuitry, we reference Fig. 3.5(b), where it is illustrated how the circuitry is composed of a TIA, instrumentation amplifier, PID control circuit, and summer. Aside from the instrumentation amplifier, all of these components were implemented using standard op-amps. However, the instrumentation amplifier is internally composed of 3 op-amps, and can be deconstructed into such. While we used individual op-amps for the proportional, derivative, and integral portions of the PID control, the entire PID control can be, and is routinely implemented, as a single op-amp circuit [89]. Hence, the circuit can be reduced to a total of 6 op-amps.

Simulations on deeply integrated silicon photonic components have shown thermal time constants on the order of ∼1 ms [72]. As was shown in chapter 2, a feedback controller implemented in analog electronics, comprised of op-amps of 3-MHz bandwidth, could stabilize against thermal fluctuations $>$ 1 kHz. Hence, we conclude that op-amps used in an integrated microelectronic implementation of the system would need to have a bandwidth on the order of 1 MHz, while being able to supply the 1 V required to maximally tune the aforementioned integrated heater [69]. Fortunately, op-amps with these characteristics have been routinely implemented in CMOS technology, with power

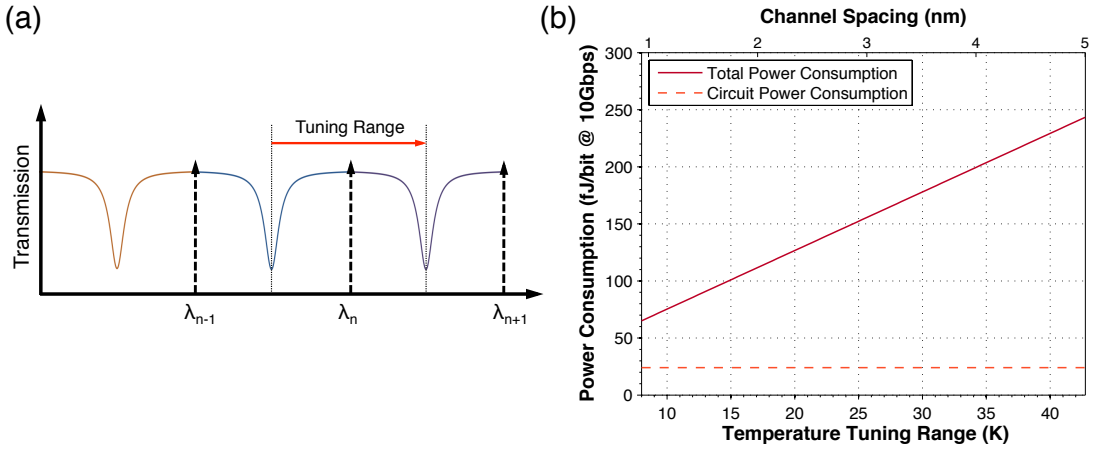

Figure 3.9: (a) Diagram of an array of microring resonators and a comb laser source with equivalent spacing. Ambient temperature changes will create relative offsets between the two grids, but this can be corrected by tuning the microring to the laser, with the maximum tuning range equivalent to the channel spacing (the microring-wavelength arrangement will be reshuffled if the microring needs to be tuned past this pony). (b) Estimated average power consumption for thermally stabilizing a single microring modulator. For larger channel spacings (top axis), the microring modulator may have to be tuned across a larger temperature range (bottom axis).

consumptions as low as 40 μW [90]. This yields an aggregate power consumption of 24 fJ/bit of the circuit at a microring modulation speed of 10 Gb/s.

To fully leverage the advantages of microrings, future optical interconnects will likely utilize them in a WDM configuration (as shown in Fig. 3.8). The source for this type of system will likely be a comb laser containing evenly spaced channels [43]. Additionally, advances in process technology have demonstrated evenly channel-spaced microrings within localized regions [91]. Hence, it is possible to engineer a system in which there is a rigidly channel-spaced laser source, a rigidly and equivalently channel-spaced array of microring modulators, and a slight offset between the two WDM grids from ambient temperature changes.

Lastly, we note schemes to minimize the maximum tuning range of any single microring modulator. Specifically, if the temperature change is large enough to shift the microrings more than one channel spacing of their original position, the microring-wavelength assignments can be reshuffled to minimize tuning [37]. Hence, as depicted in Fig. 3.9(a), the maximum tuning range required for a single microring modulator

will be equivalent to the channel spacing.

In the outlined system, the power consumption for thermally stabilizing a single modulator will be, on average, $P_{Total} = P_{Circuit} + 0.5 \times Max\{P_{Heater}\}$, where $P_{Circuit}$ is relatively static, and Max$\{P_{Heater}\}$ is the maximum required power expended by the heater. Utilizing the previous metrics and analysis, Fig. 3.9(b) plots the average power consumption of the thermal stabilization system as a function of channel spacing (top axis), or equivalently, the maximum temperature tuning range required for that channel spacing (bottom axis).

The plot in Fig. 3.9(b) shows that the integrated heater comprises the large bulk of the power consumption, especially when it is required to cover a large tuning range. As section 1.3.2.1 reviewed, there are far more progressive integrated heaters than the one chosen for this analysis. Adaptation of these extremely energy efficient integrated heaters would drastically reduce the power consumption of the thermal stabilization system.

3.6 Conclusion

This work demonstrated a control system that maintains error-free performance of a microring modulator when subjected to thermal fluctuations of 3 K, a magnitude that would normally render it inoperable. The magnitude of the generated thermal fluctuations were limited by the thermal test setup. However, through use of the integrated heater, the control system should be able to guard against the very large thermal fluctuations that would be present in commercial applications.

Importantly, all the optoelectronic components necessary to implement the stabilization system have been integrated onto a single device using CMOS-compatible processes. And as shown, this bit-rate transparent stabilization system operates independently, and without disturbing, the high-performance optical modulation.

Chapter 4

Wavelength Locking and Stabilizing Microring Resonators using Dithering Signals

While the work presented in chapter 2 and 3 on the use of power monitoring technique is valuable, it is only applicable to the specialized case of microring modulators. While microring modulators are undoubtedly one of the most popular and important microring-based devices, there are also a number of other functionalities microrings have manifested in their passive states, such as filters and switches. Furthermore, in the demonstrations detailed in chapters 2 and 3 of using power monitoring for microring modulators the initialization state of the microring modulator was manually set, whereas for commercial applications, the initial wavelength locking between modulator and laser wavelength needs to automated.

These comments tie back to the original scope of the thesis (section 1.4), a search for an elegant, robust and power-efficient method to initialize and stabilize microring-based structures. For this purpose we introduce what can be considered the main contribution of the thesis, the use of dithering signals for generating anti-symmetric error signals that can robustly initialize and lock microring resonators.

Working off this innovative dithering mechanism, the notable contributions of this work:

- Demonstrated use of a dithering signal to generate an anti-symmetric error signal.

- Thermal stabilization of a passive microring resonator using a dithering signal.
- Wavelength locking of a microring resonator using a dithering signal.
- Fast μs-scale wavelength locking of a microring resonator using a dithering signal.

4.1 Dithering Signals for Generating Anti-symmetric Error Signals

Locking a laser wavelength to a optical resonator is not a new problem. The greatest precedent for this stems from the nascent beginnings of laser technology, in which the laser wavelength would be locked to a fixed-wavelength gas cavity cell. In those scenarios, methods such as the Pound-Drever-Hall (PDH) technique would be used to generate anti-symmetric error signals which could then be incorporated into closed-loop feedback controllers [92]. However, in these aforementioned techniques the anti-symmetric error signal was generated by the manipulation of the laser wavelength (for instance, a phase or polarization modulation). In a microring resonator system, we are interested in tuning the resonator to a wavelength (rather than the vice-versa just described); hence, old techniques such as PDH locking are not applicable.

To resolve this issue, this work introduces the principle of using a dithering signal on the resonator to generate an anti-symmetric error signal centered at the resonant wavelength of the microring. Fig. 4.1(a) illustrates the dithering mechanism (applied thermally), whereby a small modulation is applied to the local temperature of the microring in order to produce a small modulation of the optical signal (it should be noted that, while not as practical, the dithering can also be applied electrically). The generated optical modulation will either be in-, or out-of-phase with the driving signal, depending on which side of the resonance the laser wavelength is offset. By mixing the modulated optical signal with the driving dithering signal this information can be recovered as shown in Eq. 4.1, where f_D is the frequency of the dithering signal, and ϕ is the relative phase (0 or π) of the modulated optical signal.

$$\cos(f_D t) \otimes cos(f_D t + \phi) = \frac{1}{2}[\cos(2f_D t + \phi) + cos(\phi)] \tag{4.1}$$

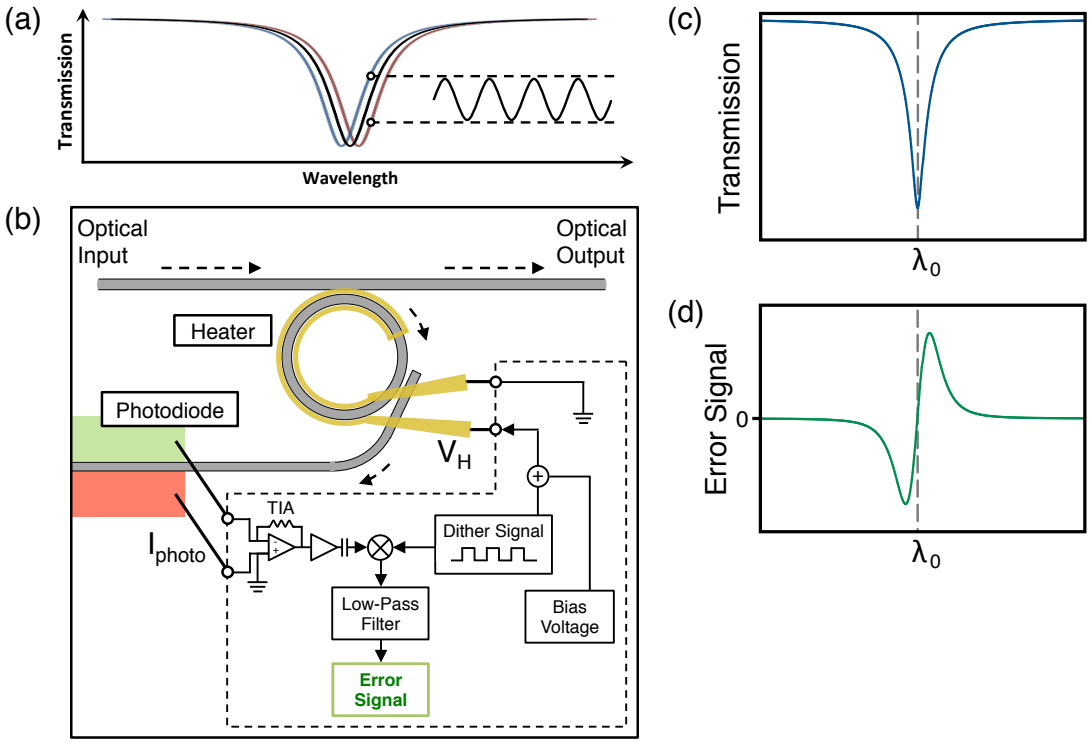

Figure 4.1: (a) A small dither signal, applied thermally to the microring resonator, results in a small modulation of the optical signal (depicted for thru port response). (b) Schematic of the setup for generating an error signal using the dithering mechanism, off-chip circuitry is shown in the dashed box. (c) Symmetrical ***optical*** thru port response of a microring resonator and the corresponding (d) ***electrical*** anti-symmetric error signal generated.

The higher harmonic can be filtered, leaving the sign of the DC component $\cos(\phi)$ term as an indication of the location of the resonance relative to the optical signal. The end product of this process is the desired anti-symmetric error signal.

Fig. 4.1(b) depicts the configuration of the microring resonator and the off-chip electronics required to generate the error signal. Fig. 4.1(c) depicts a typical thru port optical response of the microring resonator, and Fig. 4.1(d) shows the expected electrical error signal. As can be seen in the graphs, the error signal is essentially the first derivative of the optical response.

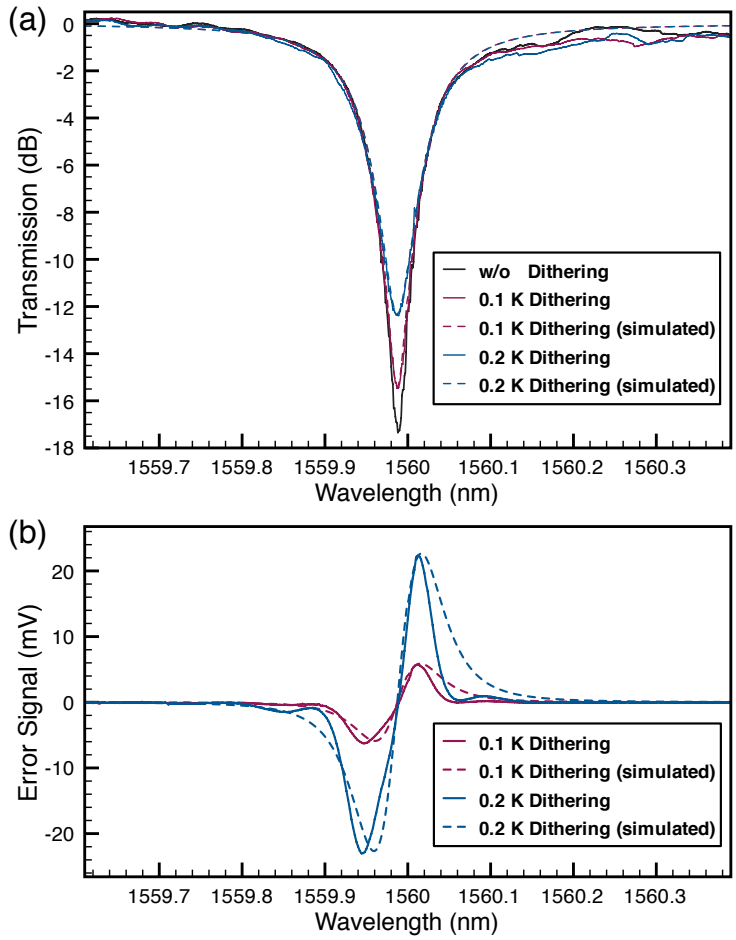

Figure 4.2: (a) The microring resonance as it is subjected to thermal dithering signals of varying magnitude (simulations in dashed). (b) The corresponding generated error signals (simulations in dashed).

4.1.1 Measured Error Signal

In this work, the device used to demonstrate the use of the dithering mechanism is the same one as described in chapter 3. Similarly, the off-chip electronics implementing the thermal dithering system are shown in the dashed box of Fig. 4.1(b) consist of low-speed ($<$ 20-MHz bandwidth) analog and digital ICs. A 1-kHz square-wave dithering signal is used. An analog multiplier IC (AD 633) was used to mix the received photo signal with the driving dithering signal, producing the products of Eq. 4.1. This product was then low-pass filtered to generate the desired error signal.

The use of the thermal dithering signal has the consequence of reducing the extinction ratio of the microring resonance. In Fig. 4.2(a), the simulated and measured resonances of the microring resonator (Q of ∼14,000) are plotted for square-wave thermal dithering signals of magnitude 0.1 K and 0.2 K. A larger thermal dither will result in a larger reduction of the extinction ratio. Fig. 4.2(a) shows the un-dithered resonance having an original extinction ratio of 17.3 dB. For thermal dithering of magnitude 0.1 K and 0.2 K the reduction in extinction ratio was measured to be 1.9 and 4.8 dB, respectively. Simulations produced identical results (Fig. 4.2(a)). While a larger thermal dither results in a larger reduction in extinction ratio, it has the advantage of producing a stronger error signal. Fig. 4.2(b) plots the simulated and measured waveforms of the generated error signal.

The anti-symmetric response of the error signal (see Fig. 4.2(b)) clearly distinguishes between the red and blue sides of the microring resonance. Furthermore, the zero crossing of the monotonic slope is located at the resonance minimum. Hence, a feedback controller can easily stay locked to the zero crossing in order to lock the microring resonance with the laser wavelength. While a larger error signal makes the system more robust against noise, we found that the smaller 0.1 K dithering signal generated a sufficient error signal for locking and stabilizing the microring resonator. All further results described in this chapter on this device were done using a dithering signal of magnitude 0.1 K.

4.1.2 Optimization of the Error Signal

As aforementioned, our experimental implementation utilized a square-wave dithering signal rather than the sinusoidal dithering signal described in Eq. 4.1. In theory, the dithering signal can be composed of any periodic waveform. However, the square-wave offers the advantage of being able to be synthesized easily in electronic circuitry. Additionally, the mixed product of (ideal) square-waves will produce a pure DC component and none of the higher harmonic components that are eventually filtered (see Appendix B). This has the consequence of producing a larger error signal for dithering signals of equivalent magnitude. Fig. 4.3(a) graphs simulations of the generated error signals when using an ideal square-wave dithering signal versus using an ideal sinusoidal dithering signal. As can be seen from the graph, the square-wave dithering signal generates an error signal that is twice as large in magnitude.

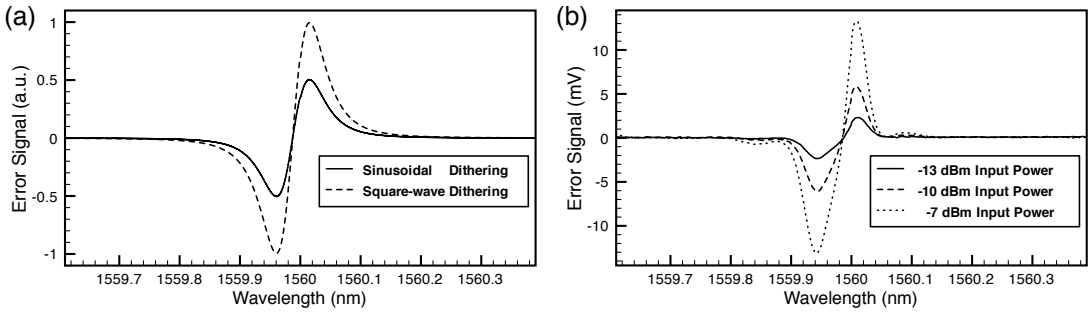

Figure 4.3: (a) Simulations of the generated error signal contrast the use of a square-wave dithering signal versus the use of a sinusoidal dithering signal. (b) The measured error signals when a 0.1 K thermal dithering signal is applied to the resonator and the optical power of the laser into the chip is varied.

4.1.3 Immunity to Power Fluctuations

A significant advantage of the generated error signal is that it is relatively immune to changes in the optical power of the signal. In future microring-based optical networks it is envisioned that optical paths can be reconfigured as necessary to address dynamic bandwidth allocation requirements. The insertion loss characteristics of optical paths will change as they are re-provisioned, yielding uncertainty in the optical power reaching any given microring resonator.

As Fig. 4.3(b) shows the generated error signals will change in magnitude following variations in optical power. Additionally, the slope of the error signal will also vary. However, a robust feedback controller (one that is able to contend with the change in slope of the error signal) will be able to maintain the locking between the microring resonator and laser wavelength because the zero crossing of the error signal remains constant.

It should also be noted that, as demonstrated, these error signals can be generated with a relatively weak optical signal reaching the photodetector. The fiber-to-fiber coupling loss of the chip was measured to be $\sim$ 20 dB; assuming symmetric coupler and waveguide losses, the power reaching the photodiode for the measured error signals in Fig. 4.3 is then less than -20 dBm. This figure covers the lowest optical powers that would be present in a silicon photonic link given the sensitivity limit on current photodetectors [26].

4.1.4 Effect of Dithering on Data Signals

For use in data applications, it is critical that the dithering of the microring resonance does not negatively impact the integrity of the optical data signals. To test this, we simulated 10 Gb/s optical data signals as they are routed from the input port, through the microring, and into the drop port of a dithered microring resonator (a microring in a demultiplexing configuration). Fig. 4.4 shows the simulated eye patterns of the received signal when a dithering signal of magnitude of 0.1 and 0.2 K was applied to the microring, as well as when no dithering signal was applied (as stated before, a 0.1 K dithering magnitude was sufficient for experimentally locking and thermally stabilizing the microring resonator). In these simulations, we modeled the microring resonator to have the same characteristics (extinction ratio and Q) as the microring resonator we worked experimentally with (see Fig. 4.2(a)).

As expected, and as evidenced by the simulated eye patterns, the dithering has the effect of broadening only the '1' level of the optical signal. However, this broadening is minimal, resulting in eye closures of only 0.3% and 1.6% when using dithering signals of 0.1 and 0.2 K, respectively. For small deterministic eye closures such as this, the power penalties can be directly correlated as being 0.01 and 0.07 dB, respectively. Power penalties of this magnitude are well within the optical link budgets for microring-based links [26], and hence will not impede the use of the dithering technique for data applications.

Finally, it should be noted that the error signal generated from a modulated signal will be smaller than the error signal generated from an unmodulated signal. This is due to the broadened spectrum of the modulated signal. Our simulations show that the error signal generated from a 10-Gbps NRZ signal will be 20% smaller than an error signal generated from an unmodulated signal (when using a microring resonator with the prior discussed parameters).

4.2 Wavelength Locking using Dithering Signals

The first application of the generated error signal is in the process of tuning the microring resonator such that it is aligned in resonant wavelength with the laser source, denoted as "wavelength locking". The electronic circuitry devoted to the wavelength locking process is detailed in Fig. 4.5(a) (outlined by the red box). The functionality of

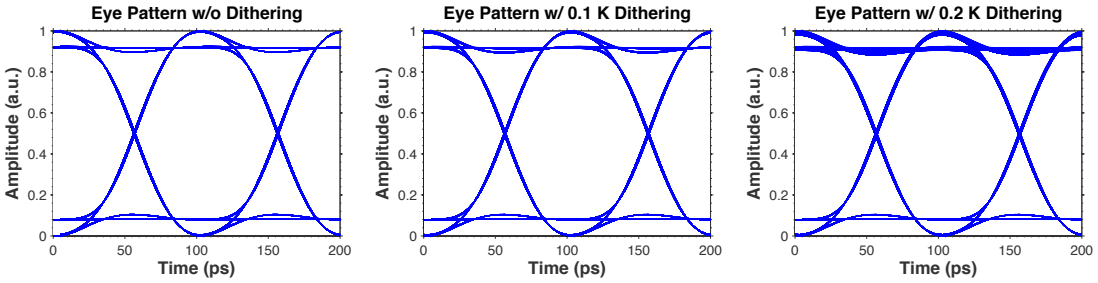

Figure 4.4: Simulated eye patterns of a 10 Gb/s optical signal propagating through a microring with no dithering (left), and dithering magnitudes of 0.1 K (middle) and 0.2 K (right).

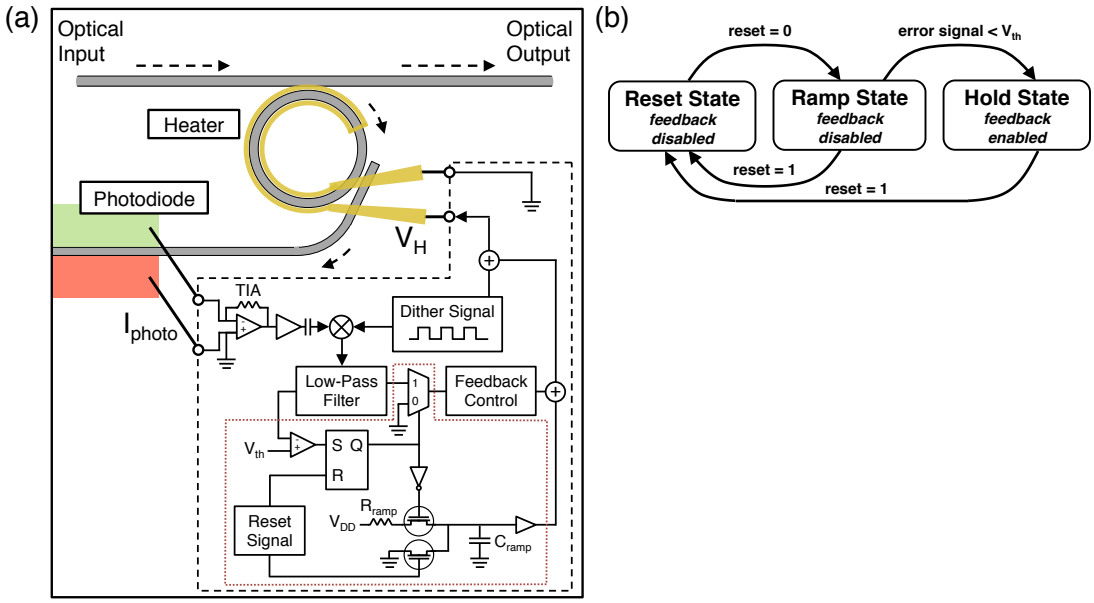

Figure 4.5: (a) Schematic of the device and circuitry implementing the dithering mechanism, and additionally, the added circuitry (dashed red box) for implementing wavelength locking. (b) A state diagram describing the functionality of the wavelength locking circuitry.

this circuitry is succinctly described in the state diagram of Fig. 4.5(b). A simple reset signal is used to trigger the ramping of the voltage applied to the integrated heater. As the microring is tuned to the laser wavelength the error signal will trip the system into the hold state, in which the feedback controller is activated and the microring is locked and stabilized against further drifts in temperature or laser wavelength. Additional

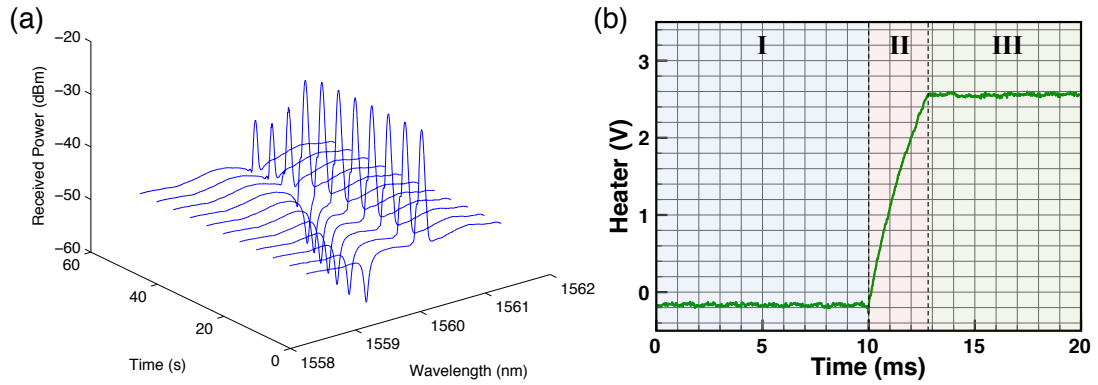

Figure 4.6: (a) Optical traces show the microring resonance being tuned and wavelength locked to a laser source. (b) Oscilloscope trace of the heater voltage as the microring is wavelength locked to the laser source. Annotated are the reset state (I), ramp state (II), and hold state (III).

logic can be added to reset and re-attempt the wavelength locking should it fail on its initial attempt.

The optical spectrum analyzer traces in Fig. 4.6(a) demonstrate the system locking a microring resonator to a laser (an ASE source is used to background image the microring's resonance). Initially, the microring resonance is at ∼1559.2 nm, and the laser is offset at ∼1560 nm. Over the course of 50 s, the microring is tuned higher in wavelength until the control system detects the error signal and establishes the lock. To record the optical traces of Fig. 4.6(a), the ramp speed (rate at which the tuning occurs) of the system was drastically reduced, such that the wavelength locking would occur over the course of seconds. In subsequent trials, the ramp speed was increased to achieve wavelength locking in the ∼ms time frame (and further work in this chapter will show $\sim \mu$s-locking).

Fig. 4.6(b) shows an oscilloscope measurement of the heater voltage during the wavelength locking process. Here, the ramp speed has been decreased to allow locking in the ∼ms regime. The graph of Fig. 4.6(b) has been annotated with the stages of the state machine, with the period (I) designating the heater voltage while the system is in the reset state, (II) designating the period in which the voltage is ramped, and (III) designating the wavelength-locked hold state, which occurs once the microring resonator and wavelength become aligned.

4.3 Thermal Stabilization using Dithering Signals

The wavelength locking method we have demonstrated serves as an effective means to initialize the microring-based photonic link. Tying back to the work described in chapter 2 and 3, the error signal generated using the dithering mechanism was used to demonstrate the thermal stabilization of a passive microring resonator.

To implement this, the thermal dithering system was multiplexed with a feedback system (as schematized in Fig. 4.5(a) to thermally stabilize the microring resonator. To test the system, 10-Hz sinusoidal thermal fluctuations of magnitude 5 K were generated using an external visible laser (as previously described in section 2.2).

In order to verify the thermal stabilization, wavelength scans were performed of a resonance adjacent in wavelength to the resonance that the thermal dithering and feedback system was locked to (see Fig. 4.7(a)). As Fig. 4.7(a) shows, with the thermal dithering and feedback system implemented, the microring resonance stays locked to the laser wavelength, with the dynamic tuning of the heater counteracting the thermal fluctuations inflicted on the microring (see Fig. 4.7(b)). In contrast, without thermal stabilization, the resonance fluctuates severely, being washed out in the wavelength scan (see Fig. 4.7).

This thermal stabilization method is robust enough that wavelength locking can occur even in thermally volatile environments. To demonstrate this the microring resonator was wavelength locked while the microring resonator was subjected to sinusoidal thermal fluctuations. Fig. 4.7(c) shows the heater voltage during this process. At the moment in time that the microring resonator is wavelength locked, the system immediately begins the thermal stabilization mechanism (as evidenced by the sinusoidal counter-tuning of the heater voltage in Fig. 4.7(c)).

4.4 Scalability and Power Efficiency

In order for the demonstrated control system to be adapted for commercial microring-based links it must be scalable. Scalability requires meeting two criteria, the first being that the control system is sufficiently low-power such that the aggregate power consumption of initializing and stabilizing all the microring resonators in the optical link does not exceed the power-efficiency improvement gained by the use of microring resonators. Secondly, the mechanisms in the control system must be compatible with

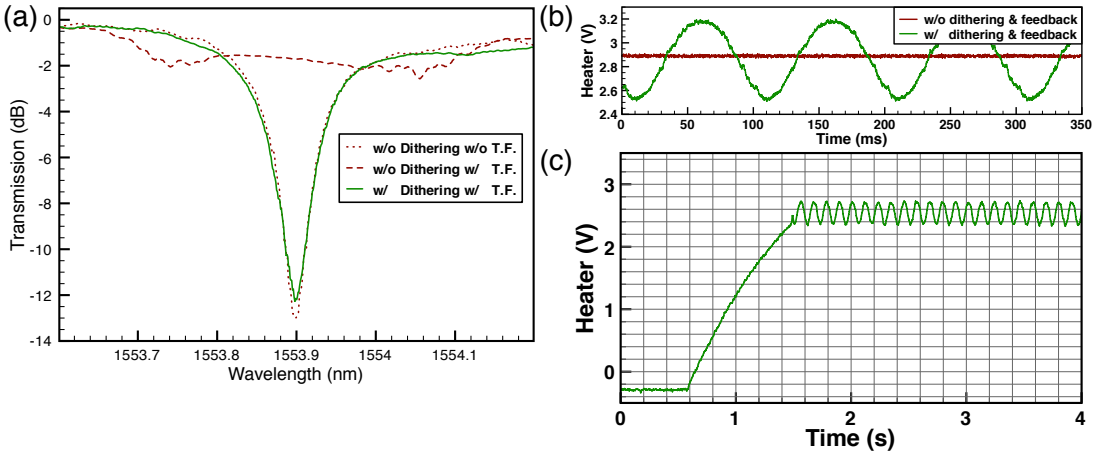

Figure 4.7: (a) The microring resonance when subjected to thermal fluctuations (T.F.) with and without the dithering and feedback system implemented. Also shown for comparison is the resonance without the thermal stabilization system under normal, thermally stable conditions. (b) Heater voltage when the microring resonator is being exposed to thermal fluctuations and, with and without, the dithering system counteracting said fluctuations. (c) Heater voltage as the microring resonator is wavelength locked while being subjected to sinusoidal thermal fluctuations.

the typical WDM configuration of microring resonators, in which they are multiplexed along a common waveguide bus.

To get an estimate of the power consumption we replicate the approach of section 3.5, tabulating the active components of the control circuitry (see Fig. 4.5(a)) and referencing established power consumption figures when these components are implemented in conservative CMOS technology. We note that the majority of the circuitry devoted to wavelength locking (see Fig. 4.5(a), red box) is composed of digital logic elements that only draw power when switching logic states. Under the assumption that the optical links operating time will be much longer than the initialization period, the power consumption of these elements are negligible. The feedback control can be decomposed into 4 op-amps (see section 3.5), with the TIA, unity buffer, and summers contributing another 4 op-amps, for a total of 8 op-amps. Op-amps with the required ∼MHz bandwidth characteristics have routinely been implemented in CMOS technology with power consumptions as low as 40 μW [90]. The dithering signal can be implemented using an oscillator, with an example oscillator covering the required sub-MHz to few-MHz range while exhibiting power consumptions as low as 20 μW [93].

Lastly, analog multipliers are also routinely implemented in CMOS technology, with a conservative example having a power consumption of 45 μW [94]. The aggregate power consumption of the control circuitry can then be estimated to be 385 μW. To express this in the popular fJ/bit metric we assume that the microring resonator is operating on a 10 Gb/s data signal, yielding a power consumption of 38.5 fJ/bit for the control circuitry. This estimate falls well within the strictest pJ/bit power budgets required of some envisioned applications [20].

As was mentioned in section 3.5, the power consumption of the full control system should also include that of the integrated heater. These values were reviewed in section 1.3.2.1, with the current leading technology showing exceptionally promising tuning efficiencies.

When considering the other important criteria, that the control method is compatible with WDM implementation, we note that there are no inherent features of the dithering technique that precludes the use of WDM. The dithering is a process local to the microring resonator and does not affect adjacent multiplexed microring resonators. As was illustrated in Fig. 3.8, the use of drop port detectors lends itself to the multiplexed arrangement of WDM microring resonators. A demonstration of WDM scaling the dithering mechanism will be shown in chapter 5.

Additionally, for complex microring-structures, such as large radix switches [15], the orthogonality principle can be leveraged by utilizing different dithering frequencies for different microring resonators:

$$\int \cos(f_n t) cos(f_m t) dt = 0, f_n \neq f_m \tag{4.2}$$

This feature eliminates crosstalk in error signals even when microring resonators overlap in the spectral regime.

4.5 μs-scale Wavelength Locking of a Microring Resonator

In any data link, latency is a critical parameter, and depending on the application, may supersede bandwidth and energy-efficiency in importance. For optical links, there are a variety of factors that determine the latency, such as time-of-flight, PLL lock times, and complexity of encoding. When considering the system design of microring-based optical interconnects, a critical component of the latency will be associated with initializing the

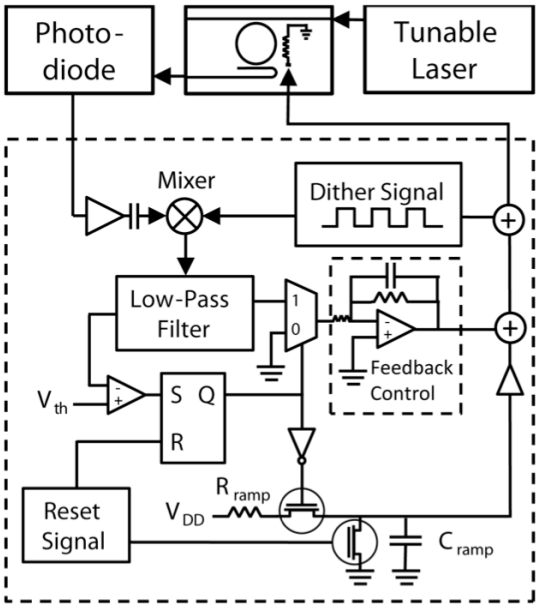

Figure 4.8: Schematic of the experimental setup and the wavelength initialization circuitry, with configuration of the chip indicated in the top-center of the diagram.

microring-based devices. For some architectures, the initialization will be a one-time event; however, other architectures, those emphasizing either energy-efficiency or rapid path configuration might require re-initialization for every data transfer.

The goal of this work was to study the latency characteristics of wavelength locking when using dithering signals, and show that μs-scale wavelength locking is possible when using the dithering mechanism.

The device used in this work differed from the prior device that the dithering mechanism was first demonstrated on. Full details on the device are given in chapter 5, but it can be succinctly described as a 10 μm diameter microring demultiplexing filter fabricated using a standard CMOS-compatible process on a 250 nm SOI wafer with 3 μm of buried oxide. It has 450×250 nm waveguide channels and a nickel-chromium heater deposited on top of a 1 μm thick oxide cladding. With a small 1 μm separation from the microring, the 1.8 kΩ heater offers a tuning efficiency of 0.56 nm/mW (70 GHz/mW).

The experimental setup is shown in Fig. 4.8. A tunable laser is coupled onto the chip using tapered fiber, and DC probes are used to contact the heater. A 100 kHz,

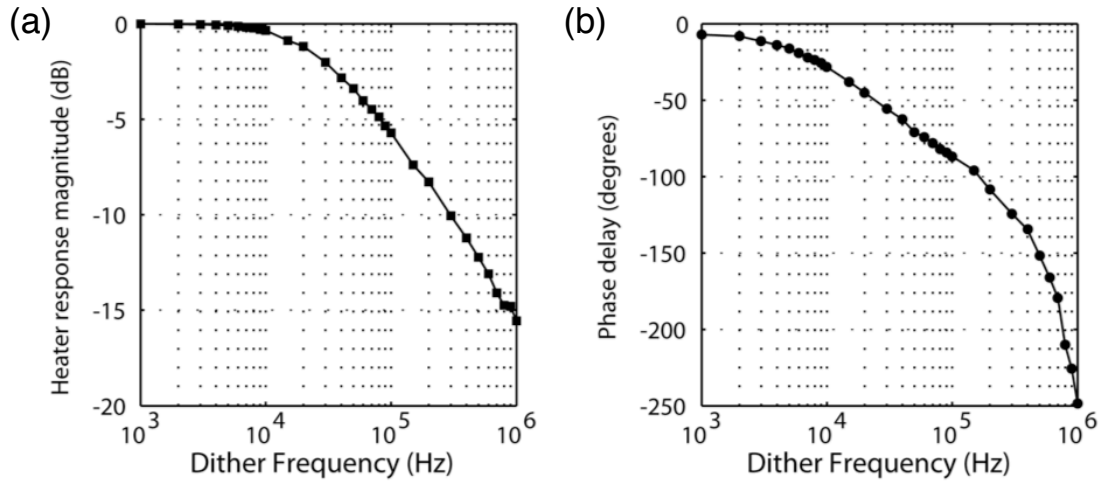

Figure 4.9: Thermo-optic modulation characterization of the integrated heater, showing the (a) magnitude and (b) phase of the generated dithering signal.

40 mV_{pp} sinusoidal dither signal drives the heater, which imprints a small modulation on the light reaching the drop port. Here, instead of an integrated photodiode as was shown for the prior device in the chapter, the output at the drop port is detected by a commercial off-chip low-speed photodetector and mixed with the original dither signal to generate the error signal used for feedback.

4.5.1 Experimental Results

The total latency for wavelength locking can be approximated as

$$t \approx \left(\frac{\Delta\lambda}{\frac{\partial\lambda}{\partial t}} \right) + t_{circuit} + t_{feedback} \tag{4.3}$$

where $\Delta\lambda$ is the offset between the resonance and laser wavelength, $\partial\lambda/\partial t$ is the ramp speed of the heater, $t_{circuit}$ is the delay from the circuit logic, and $t_{feedback}$ is the time it takes for the feedback system to stabilize. $t_{circuit}$ is measured in 10s of nanoseconds, as would be expected given the shallow logic depth and the speed of current digital circuitry. Hence, $t_{circuit}$ is sufficiently small that it be can ignored when approximating the aggregate initialization time.

Our work has found that the frequency of the dithering signal is the key limitation on the wavelength locking latency. Essentially, the control system can not respond faster

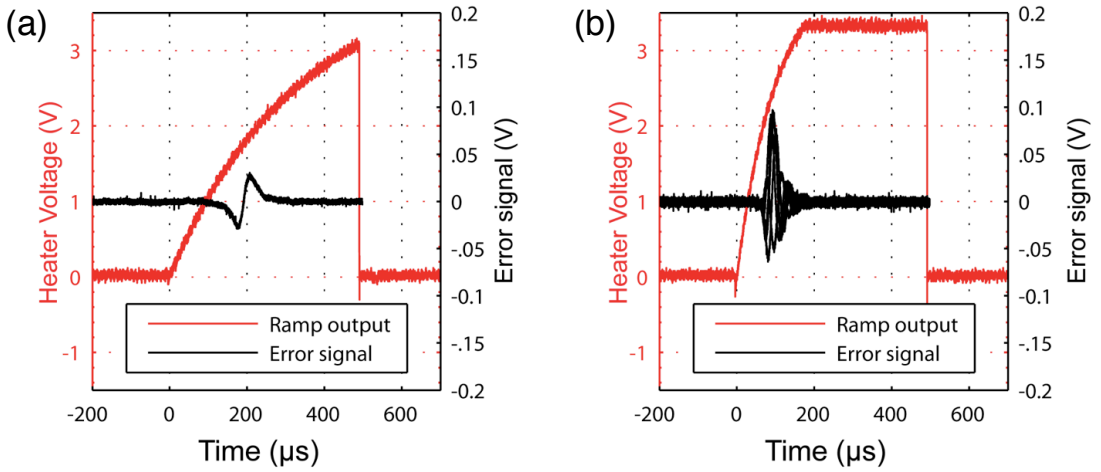

Figure 4.10: (a) Ramp rate that generates an usable error signal. (b) Ramp rate that is too fast, generating an unstable error signal.

than the rate at which the microring resonator is dithered. The dithering frequency is in turn, limited by the thermal time constant between the integrated heater and microring resonator. Fig. 4.9 shows the magnitude and phase of the optical modulation from the heater as the frequency of the dithering signal is increased.

From this characterization, the maximum frequency of the dithering signal was chosen to be 100 kHz to achieve the lowest wavelength locking latencies while maintaining sufficient SNR at the output of the mixer to lock the microring successfully.

Using the 100 kHz dithering frequency, we then characterized the fastest possible ramp rates of the integrated heater. Fig. 4.10(a) shows the fastest usable ramp rate achieved for this specific device, corresponding to a resonance shift of 0.012 nm/μs (1.5 Ghz/μs), and the corresponding recovered error signal. A faster ramp rate generates an unstable error signal (Fig. 4.10(b)). This instability arises because the ramp signal has frequency components on the same order as the dither signal itself, which interferes with the mixing process used to generate the error signal. The faster heater ramp also overshoots the actual device thermal response, making it impossible for the feedback system to lock at the resonance and stabilize the system.

Lastly, we consider the stabilization time ($t_{feedback}$) required during the wavelength locking process. Fig. 4.11 shows feedback voltage during the wavelength locking process when the 100 kHz dithering signal is used. At the time denoted 0 μs, the error signal

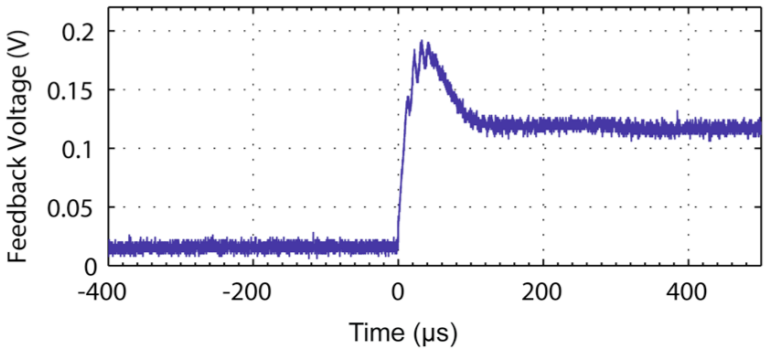

Figure 4.11: Feedback circuit output during initialization, inverted for clarity.

trips the control circuitry enabling the PID controller. As evident in the graph, the circuit overshoots and then settles back to a steady state after 100 μs. Because the dither signal generates the error input to the feedback system, the settling time must be larger than the period of the dithering signal. Hence, the measured settling time of 100 μs, one order larger than the period of the 100 kHz dithering signal, is relatively close to the fastest possible stabilization time.

Fundamentally, the wavelength locking speed of any implemented control system using an integrated heater is limited by the thermal time constant. Our integrated heater was measured to have a thermal time constant of 7 μs, which is typical for devices with heater located above the oxide layer (see section 1.3.2.1). Given this thermal time constant, we were able to show wavelength locking on the scale of 100s of μs, showing that the dithering mechanism is effective for achieving the fastest possible wavelength locking. Furthermore, from our analysis, intimately located heaters with demonstrated sub-μs thermal time constants, can decrease this wavelength locking time by an order of magnitude [16].

4.6 Conclusion

The demonstrated control system has been shown to be able to effectively initialize and thermally stabilize individual microring resonators using the dithering mechanism. As demonstrated, the novel use of thermal dithering to generate the error signal has the advantage of giving the feedback system relative immunity to power fluctuations. This renders the system robust against fluctuations in the received power, and resilient

to Fabry-Perot artifacts in the optical path. Additionally, the use of low-speed analog and digital ICs in the experimental implementation lends credibility to the systems ability to scale in an energy-efficient manner to the multiple microring resonators that comprise a WDM photonic interconnect.

Chapter 5

FPGA Implemented Wavelength Locking of a WDM Microring Demultiplexer

The work in chapter 4 described the innovative use of the dithering mechanism for wavelength locking and thermally stabilizing microring resonators. In that work, the method was implemented in low-speed circuitry, composed of discrete analog and digital ICs. This implementation was done partly for the ease of prototyping, and also for showing that the control system can be implemented in very simple low-speed circuitry.

The work in this chapter is focused on scaling the control system such that it can wavelength lock and stabilize multiple microring resonators, specifically, a WDM microring demultiplexer system. However, to scale the control system practically, it is first translated to a FPGA-based implementation. A FPGA implementation allows the basic control system to be easily modified (for variants of the basic microring configuration) and to be scaled to cover multiple microrings (such as in the WDM microring demultiplexer).

The notable contributions of this work:

- Translation of the wavelength locking and thermal stabilization mechanisms of chapter 4 from mixed circuitry to a scalable FPGA platform.
- Demonstrated wavelength locking and stabilization of a multi-microring system.

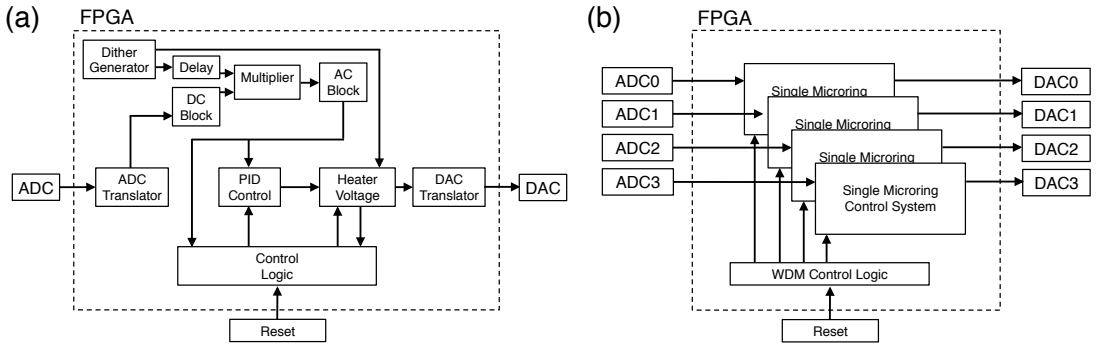

Figure 5.1: (a) Block diagram showing the FPGA implementation of the dithering-based control system for a single microring resonator. (b) Block diagram showing the scaling of the FPGA-based system to wavelength lock and stabilize multiple microring resonators in a multiplexed WDM configuration.

- Eye diagram and BER measurements on 10 Gb/s data progressing through a wavelength locked microring demultiplexer, showing an average 0.1 dB power penalty, validating the negligible effect dithering has on the integrity of data signals.

5.1 FPGA Implementation of Control System Utilizing Dithering Signals

Fig. 5.1(a) shows a block diagram representation of the implemented dithering-based control system in our FPGA platform. To convert the analog signal from the photodetector, an ADC (Maxim MAX11046) is used, and conversely, to generate the analog signal required to drive the integrated heater, a DAC (TI DAC8734) is used.

The scalability advantage is evident in Fig. 5.1(b). Here, the single-resonator control system is iterated to cover each microring resonator in the WDM link. Global control logic ties together each separate control system (for instance, controlling the sequencing of the wavelength locking). This implementation also shows the power of the dithering mechanism, in which the control system for each microring can be abstracted, localized to that specific microring resonator.

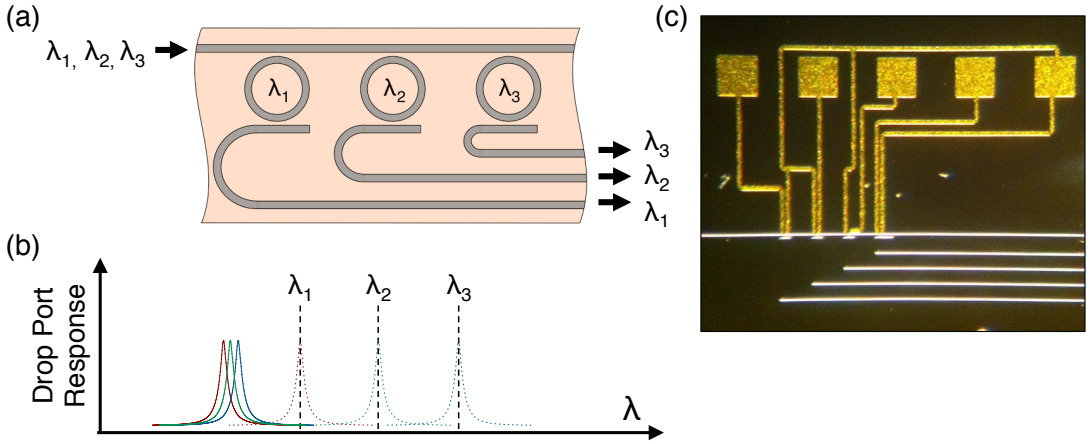

Figure 5.2: (a) Schematic of a WDM silicon microring demultiplexer. (b) Illustration of a scenario in which the microring resonances are not initialized (solid), and their corresponding position (dotted) after they have been tuned to the appropriate resonant wavelengths. (c) Microscope image of the tested device showing contact pads for the integrated heaters (top) and waveguides of comprising the microring demultiplexer (bottom). The microrings themselves are too small to be imaged at this magnification.

5.2 Wavelength Locking a WDM Microring Demultiplexer

A WDM microring demultiplexer consists of cascaded passive microring filters that demultiplex a WDM stream into their individual channels (see Fig. 5.2(a)). Typically, the drop ports of the microring resonators are terminated in a high-speed photodetector to enable conversion of the data signal into the electrical realm. However, as has been previously described, functionality of the WDM demultiplexer is contingent on the microrings being wavelength locked and thermally stabilized to their respective data channels. Prior work has shown that spectrally well-spaced cascaded arrays of microring resonators are feasible given current fabrication process tolerances [91]. In that case, each microring resonator must simply lock to the nearest laser wavelength. In this work, we tackle the even more challenging scenario of when the resonances are initially bunched (as depicted in 5.2(b)), and hence must overlap spectrally when being wavelength locked to the received wavelength channels.

The layout of the WDM silicon microring demultiplexer used in to demonstrate the control system was topologically similar to the illustration in Fig. 5.2(a), albeit the resonators were designed in a racetrack configuration. The device was fabricated at

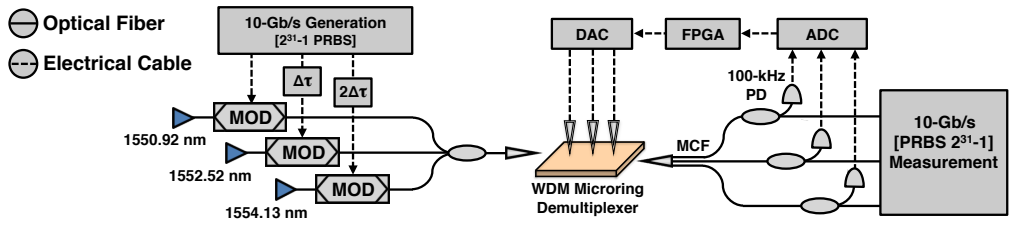

Figure 5.3: Experimental setup (polarization control not depicted).

the Cornell Nanofabrication Facility on a standard silicon-on-insulator (SOI) platform. The fabricated resonators were 5 μm in radius, with a Q of $\sim$3000. Integrated heaters were formed by depositing NiCr above the cladding of the silicon waveguide. With no power applied to the integrated heaters, the resonant wavelengths of microrings 1, 2, and 3 (corresponding to Fig. 5.2(a)) were 1549.50 nm, 1548.76 nm, and 1550.73 nm, respectively.

The experimental setup is depicted in Fig. 5.3. $LiNbO_3$ modulators were used to generate 3 data channels by modulating laser wavelengths at 1550.92 nm, 1552.52 nm, and 1554.13 nm with 10 Gb/s NRZ 2^{31}-1 PRBS. The data on the channels was decorrelated using electrical bit-delays. The data channels, at a power of -3 dBm each, were injected into the bus waveguide of the device using a tapered fiber. The 3 drop ports of the device were probed simultaneously using a 3-channel multi-core fiber (MCF). A 50-50 splitter was used to tap off a portion of each recovered data channel to be received on a slow-speed photodiode (<100 kHz bandwidth) for use in the implemented wavelength locking system. The remaining portion of the signal was evaluated for data integrity using eye diagrams and BER measurements.

As described in section 5.1, we translated the original analog and digital circuitry implementing the dithering mechanism and corresponding control system to an FPGA-based platform. The detected dithering signals (from the slow-speed photodiodes) are relayed to the FPGA through an ADC. The FPGA interfaces with the individual integrated heater on each microring resonator via a DAC that is driving electrical probes on the silicon photonic chip. Using the error signals derived from the dithering mechanism, the control system initializes the microring resonator array, tuning and locking their resonant wavelengths to the injected data channels.

The sequencing of events is more readily understood by observing the integrated

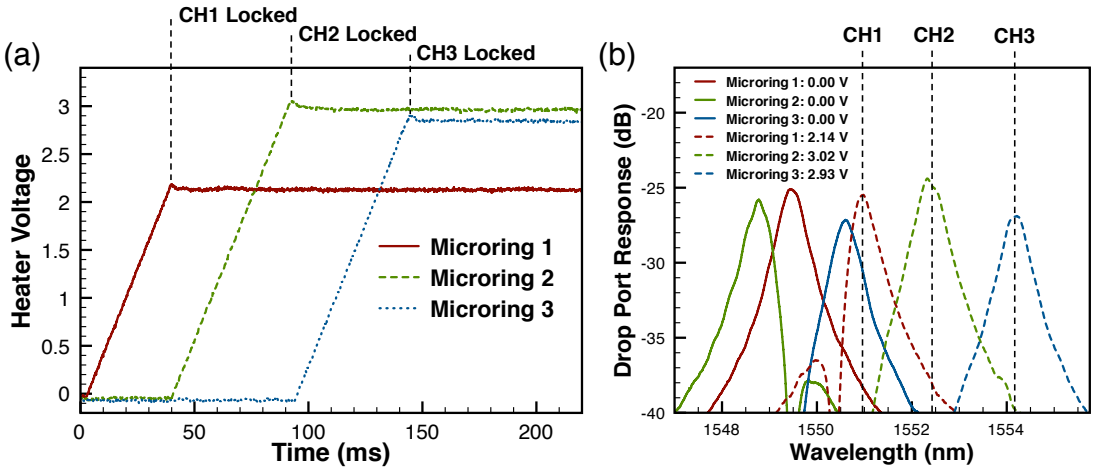

Figure 5.4: (a) Voltages applied by the control system to the integrated heaters during the wavelength locking sequence. (b) Measured drop port responses of the microring resonators when they are in their un-initialized state (solid), and when they are aligned to their respective data channels (dashed).

heater voltages during a wavelength locking cycle (Fig. 5.4(a)). To perform wavelength locking of a channel, the control system ramps the voltage on the integrated heater while simultaneously applying a small dithering voltage (a 10-mV 2-kHz square wave in this instance) to produce a thermal dithering on the resonance. Once the error signal is detected the control system halts the voltage ramp and enables the feedback loop, locking the microring resonator to the data channel. To prevent collisions, the wavelength locking of the microring resonators are sequenced (as seen in Fig. 5.4(a)) according to their physical order in the microring cascade. Using this method, the microring resonators can successfully lock to their respective channels, despite needing to cross over each other spectrally (Fig. 5.4(b)).

A critical concern is that the dithering of the resonance will affect the integrity of the data channel. To evaluate this we measured eye diagrams and performed BER measurements to contrast the performance of the data channel when manually tuning the resonators (without a dithering signal) versus using the wavelength locking system. The eye diagrams of Fig. 5.5(a-b) show that the data channels are not impacted from the use of the dithering signal. Furthermore, from our BER measurements (Fig. 5.5(c)) we found that there were relatively low power penalties of 0.1 dB, 0.0 dB, and 0.3 dB, for data channel 1 (CH1), 2 (CH2), and 3 (CH3), respectively, (an average 0.1 dB power

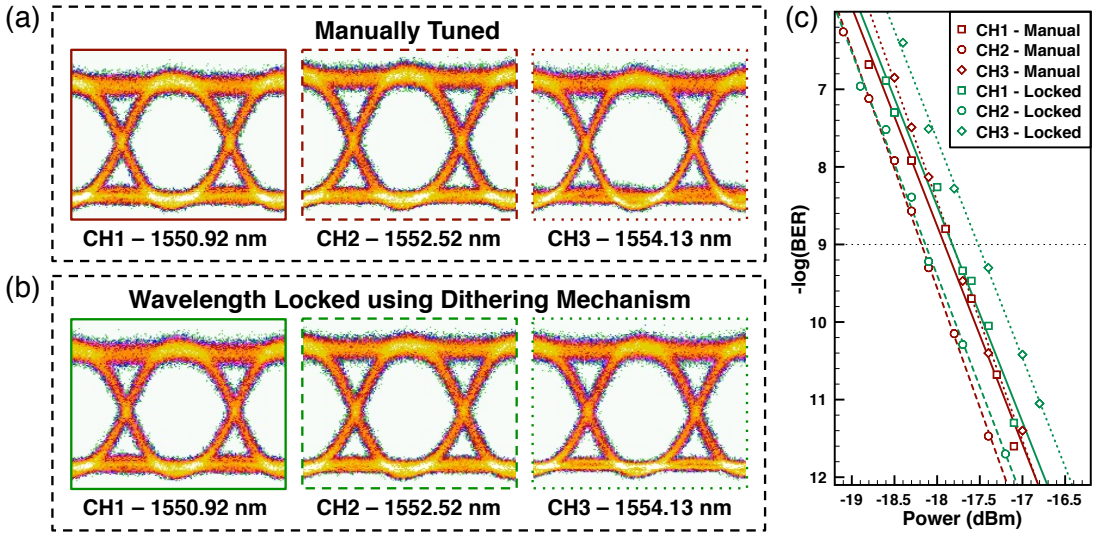

Figure 5.5: (a) Eye diagrams of a 10-Gb/s signal propagating through the microring demultiplexer when (a) manually tuning the integrated heaters to the data channels and (b) using the wavelength locking control system based on the dithering mechanism. (c) BER measurements on the respective data channels.

penalty) further validating our claim.

5.3 Conclusion

This work has demonstrated that the use of dithering signals can be scaled to advanced microring configurations, such as a WDM microring demultiplexer. It should be noted that while in their locked state, the microring resonators are also inherently thermally stabilized (as was shown in Chapter 4). Importantly, our results show that the dithering signal can be kept small enough to enable locking and stabilization while avoiding any deleterious effects on the integrity of the data.

As seen in this work, the FPGA implementation greatly eases the prototyping of complicated microring systems by allowing for the abstraction of the individual control systems governing each microring resonator. Additionally, the FPGA implementation of the control system lends itself towards future incorporation in high-speed FPGA projects, such as the prior demonstrated silicon photonic enabled CPU-memory optical link [81].

Chapter 6

Control Systems for Microring Switches

The work in this chapter continues to extend the capabilities of the dithering mechanism by adapting and demonstrating its use in thermally stabilizing a 1×2 microring switch. Succinctly, this is challenging because the microring must satisfy two states, remaining locked on to the signal when the switch is "on" (as shown in chapter 4), and also remaining off resonance with the signal when the switch is "off." It will be demonstrated how the dithering-generated error signal can be used to satisfy both of these described conditions. Additionally, we continue refinements on our thermal testbed, introducing the use of a global heater to easily generate large thermal fluctuations on chip.

The notable contributions of this work:

- Use of an on-chip global heater to generate larger thermal fluctuations for control-system prototyping.
- Demonstration that surface state absorption (SSA) from *p-i-n* silicon waveguides is sufficient to generate the photocurrent needed for the dithering mechanism (hence, no ion implantation necessary).
- Adapation of the dithering signal generated error signal for microring switches.
- Thermal stabilization of a 1×2 microring switch when subjected to thermal fluctuations of magnitude 20 K.
- Proposed expansion of the control system to cover large-radix microring switches.

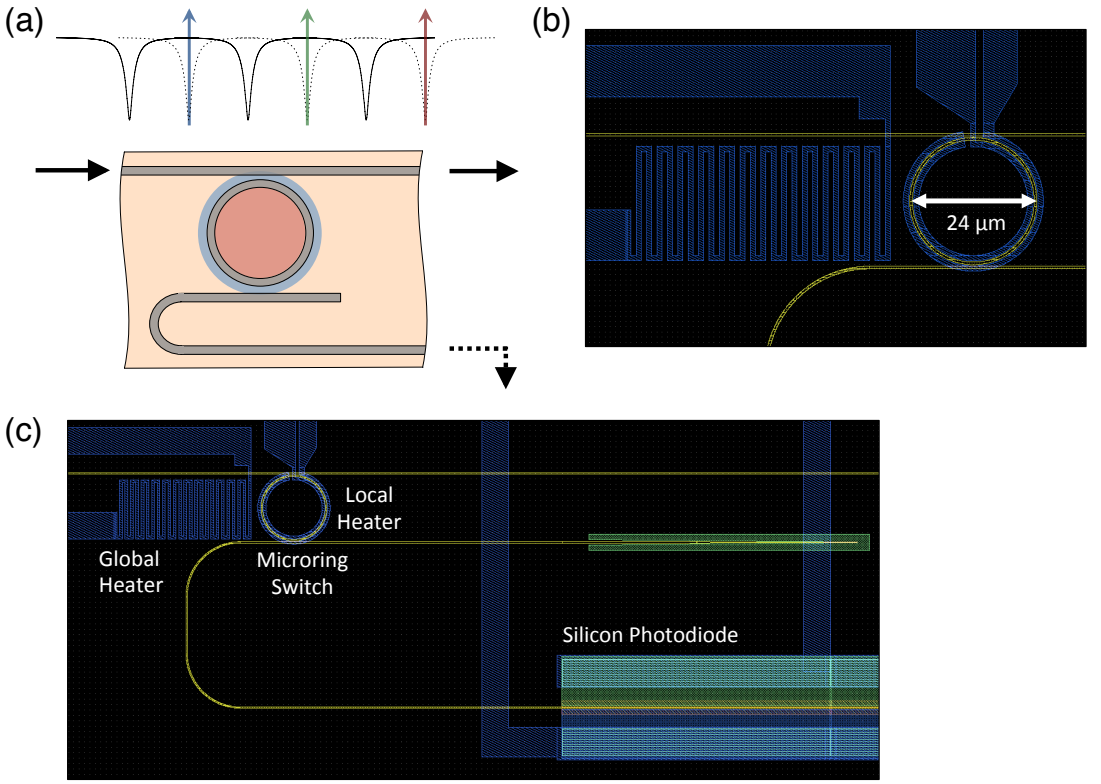

Figure 6.1: (a) Illustration of a microring comb switch with electro-optic WDM switching functionality. (b) CAD closeup showing position of microring resonator, local heater, and global heater (in blue). Waveguides are indicated in yellow. (c) CAD schematic showing position of microring switch, integrated heaters, and in-situ silicon photodiode on the microring switch's drop port.

6.1 Control System for 1×2 Microring Switch

The functionality of a 1×2 microring switch is depicted in Fig. 6.1(a). As illustrated, the FSR of the microring switch is engineered to be equivalent to the WDM spacing of the channels. With this FSR characteristic, it has been demonstrated that these basic microring switches can perform high-speed (*ns*-scale), low-energy, switching of entire WDM streams [95].

Fig. 6.1(c) shows the CAD layout of the manifested 1×2 microring switch (the parameters of the device are similar to the device described in chapter 4). While the illustration in Fig. 6.1(a) showed a *p-i-n* junction embedded within the microring to enable high-speed switching, in our device, a localized integrated heater is used

to enable thermal switching (which is equally effective, albeit has a lower bandwidth). This localized heater is also used to enable thermal stabilization of the microring switch.

6.1.1 Global Heaters for Implementing a Thermal Testbed

Depicted in the CAD closeup of Fig. 6.1(b) is the "global heater", a large integrated heater that is offset, but within the vicinity of the microring resonator. It should be noted that this global heater lies in the same plane as the localized heater for the microring resonator ($\sim$1 μm above the silicon layer). The purpose of this global heater is to generate large thermal fluctuations in the vicinity of the microring. The simplicity of this approach should be contrasted with the thermal testbed setup described in section 2.2, in which a visible laser was shone in the vicinity of the microring resonator to generate the test thermal fluctuations. The tuning efficiency of the localized heater was measured to be 0.071 nm/mW, and the tuning efficiency of the global heater is 0.0067 nm/mW, an order of magnitude lower due to the global heater's offset location from the microring resonator.

6.1.2 Silicon Photodiodes based on Surface State Absorption

Similar to the work described in chapter 4, this device used a 500-μm long *p-i-n* silicon photodiode. However, whereas our prior work had used defect-enhanced (using Si ion implantation) photodiodes, these photodiodes did not undergo an ion implantation during their fabrication process. Despite this, the silicon photodiodes were still able to produce enough photocurrent to be able to used in conjunction with the dithering mechanism. This ability to produce photocurrent despite the lack of ion implantation can be attributed to surface state absorption (SSA) in the *p-i-n*. Work from other researchers had previously identified this photocurrent mechanism, and demonstrated these types of silicon photodiodes to have bandwidth up to 60 MHz, providing ample margin for use in our demonstrated control systems [96]. As demonstrated here, this allows the use of in-situ silicon photodiodes without the additional ion-implantation step in the fabrication process.

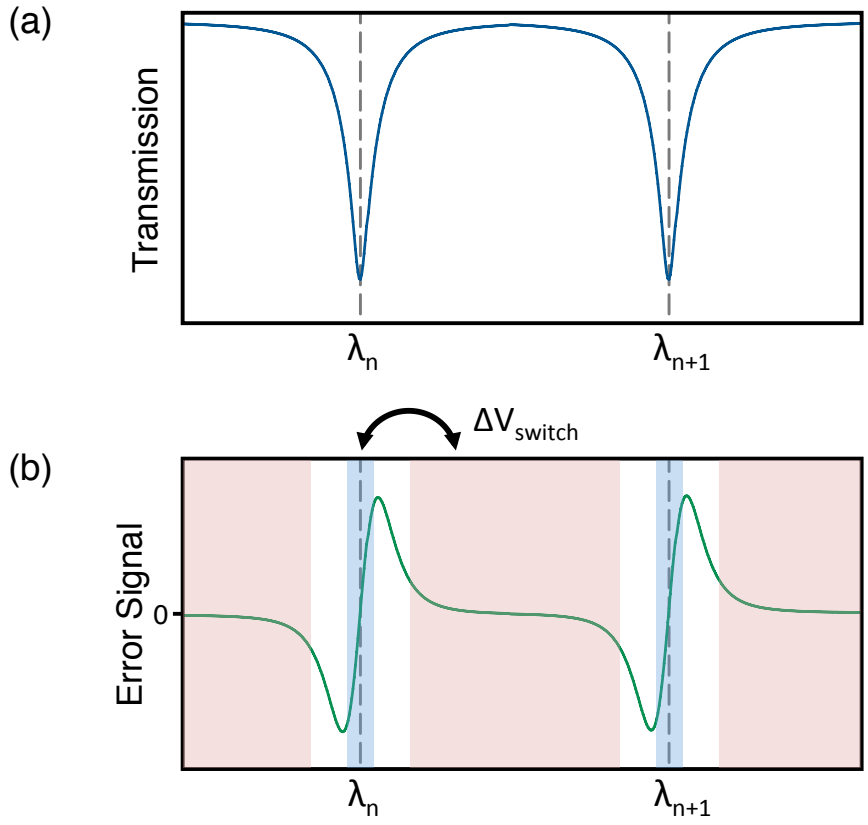

Figure 6.2: Illustration of the (a) periodic optical transmission spectrum of a microring switch and the (b) corresponding error signal generated. Highlighted in (blue) and (red) are the regions of the error signal for operating the microring switch in the (on) and (off) state, respectively.

6.1.3 Adapting the Dithering Mechanism to a Microring Switch

In chapter 4, where the dithering mechanism was first introduced, the focus was on locking the microring resonator to an optical signal. As shown further in 5, this is the necessary control functionality for a microring demultiplexer. For a microring switch however, there are two distinct states which must be satisfied:

1. When the switch is "on", the microring resonator should be locked to the optical signal, and remain locked in the presence of thermal fluctuations.

2. When the switch is "off", the microring resonator should be off-resonance from the optical signal, and remain off-resonance in the presence of thermal fluctuations.

The second condition is the new constraint that the dithering mechanism must be adapted to, that is, ensuring that when the microring has been switched off, thermal fluctuations do not drift the resonance back into alignment with the optical signal. To resolve this issue, we leverage the spectrally periodic properties of the microring resonator, and hence, the generated error signal.

Fig. 6.2(a) depicts this periodicity in the spectral transmission and corresponding error signal. Highlighted in blue in Fig. 6.2(b) is the region of monotonic slope of the error signal in which the resonator can lock to the optical signal. Additionally, highlighted in red is the region of monotonic slope of the error signal in which the resonator can "lock off" the optical signal, that is to say the resonance will stay stabilized between two wavelength adjacent optical signals in the WDM grid.

Also indicated in the diagram is V_{swing}, the voltage required to transition between the two regions. V_{swing} can be the voltage applied to the *p-i-n* junction to enable electro-optic switching (as illustrated in Fig. 6.1(a)), or as in our demonstration, it can be the voltage applied to the localized integrated heater to enable thermo-optic switching.

The experimental measurements in Fig. 6.3 show the aforementioned periodic spectral transmission and the generated error signal when using the dithering mechanism (here, the transmission through the drop port is shown instead of the thru port).

6.1.4 Thermal Stabilization of Microring Switch

An off-chip BJT amplifier circuit and function generator were used to drive the global heater with the large voltage swings required (up to 40 V) to generate large thermal fluctuations. With this implementation, the global heater was able to produce thermal fluctuations of magnitude 20 K at a frequency of 0.1 Hz in the vicinity of the microring switch. It should be noted that the global heater was limited to sub-Hz frequencies due to its large thermal time constant.

The control system for the microring switch was manifested using an FPGA implementation as had been discussed prior in detail in chapter 5. Fig. 6.4(a) shows the normalized output (at the drop port) of the microring switch when there are no thermal fluctuations, and the control system for thermal stabilization is not implementing. As can be seen, the output of the microring is switched at rate of ∼1 Hz.

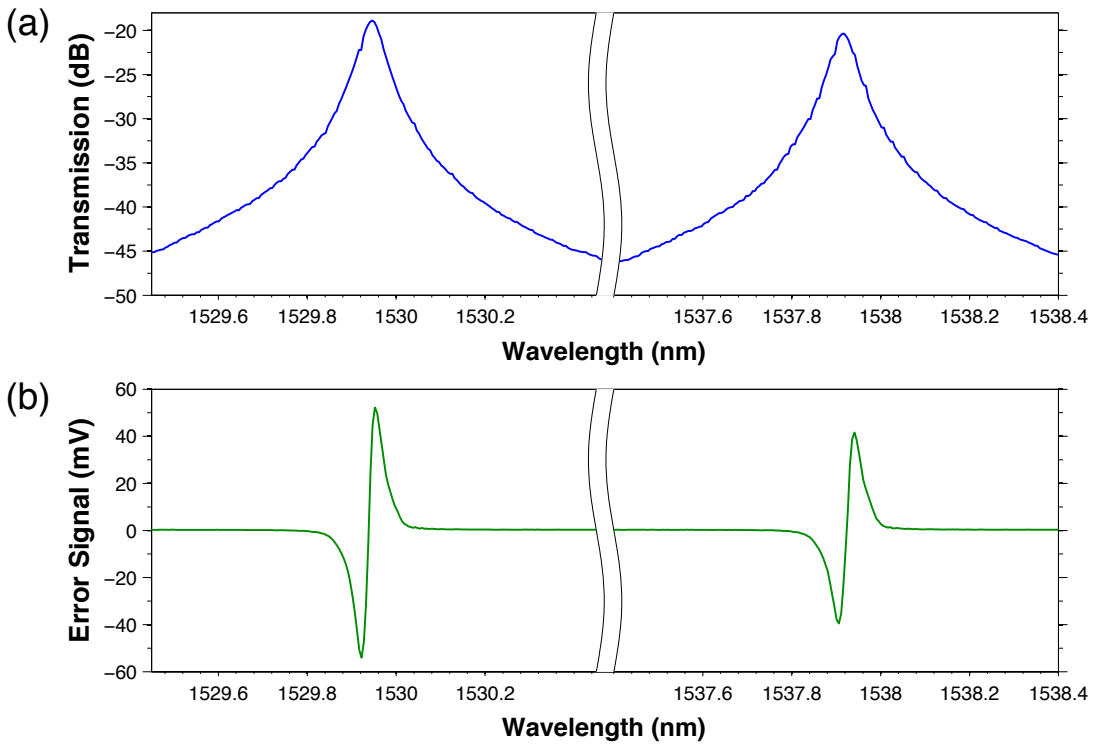

Figure 6.3: (a) Measured transmission spectrum of the switch drop port. (b) Measurement of the generated error signal.

Fig. 6.4(b) shows the switch output (showing several traces overlaid) when the global heater is generating thermal fluctuations of 20 K. It is clear from these traces that the thermal fluctuations impede any the successful switching functionality of the microring switch. However, as shown in Fig. 6.4(c), implementation of the thermal stabilization control system can thermally stabilize the microring switch and preserve its switching functionality.

6.2 Control Systems for Large-Radix Microring Switches

While a 1×2 microring switch is a useful component of future microring-based networks, the functionality of these microring switches increases dramatically as one considers higher radix switches, such as the 4×4 microring switch that has previously been demonstrated [15]. The configuration of this microring switch is depicted in Fig. 6.5(a). Example routed paths are highlighted in the diagram. In Fig. 6.5(c), the routing table

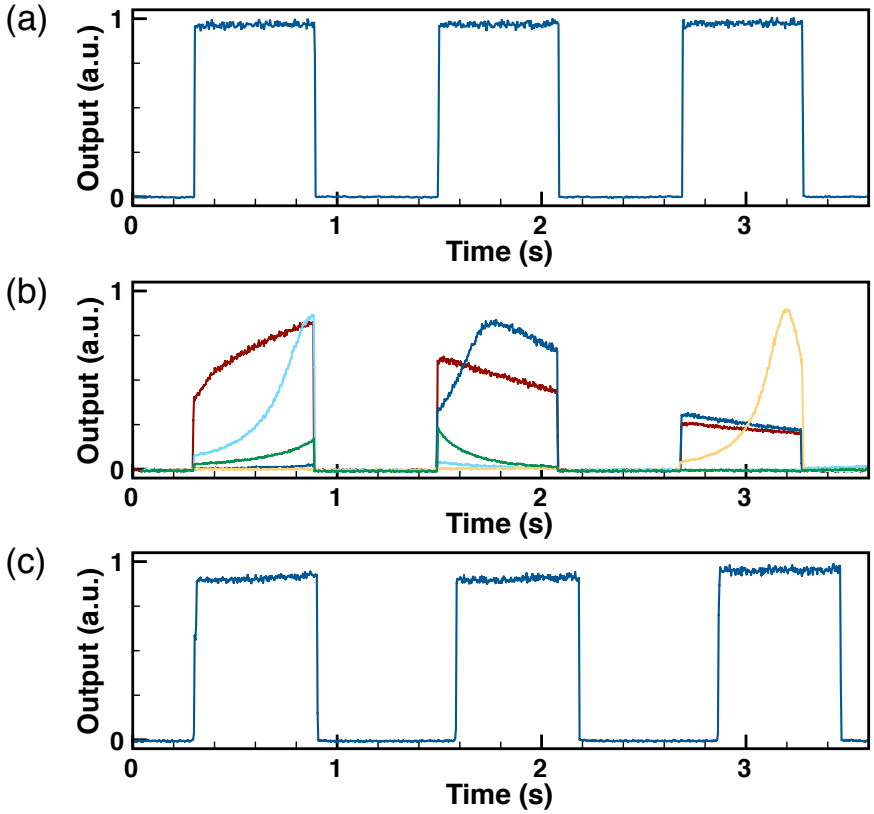

Figure 6.4: Normalized output of the switch when (a) experiencing no thermal fluctuations and having ***with no*** control system implemented, (b) experiencing thermal fluctuations of magnitude 20 K ***with no*** control system implemented (several measurements shown), and (c) experiencing thermal fluctuations of magnitude 20 K ***with*** the control system implemented.

for all states of the 4×4 microring switch are shown.

For implementing a control system we propose adding in-situ silicon waveguides (as were previously demonstrated in this chapter) to enable initialization and control of each individual microring resonator in the switch fabric. Fig. 6.5(a) illustrates the addition of the photodiodes. Each microring resonator has a corresponding in-situ photodetector downstream. In this manner they can be sequentially locked-on, or locked-off, the relevant laser wavelengths.

Leveraging the prior demonstrated control system for a 1×2 microring switch is critical for creating a tractable control solution for this large 4×4 microring switch. Essentially, as shown in Fig. 6.5, each microring resonator within the 4×4 switch has

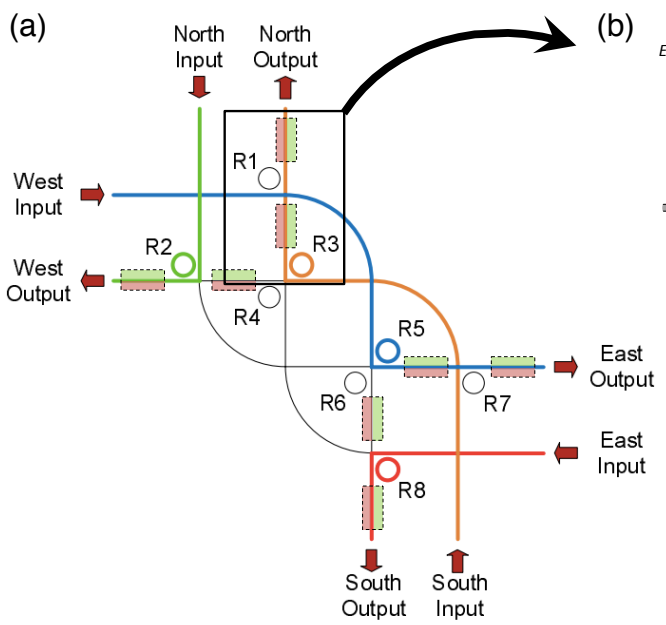

(c)

State Number	I/O Combination				
	N	S	E	W	Rings Used
1	W	N	S	E	R2,R3,R8,R5
2	W	E	N	S	R2,R7
3	W	E	S	N	R2,R7,R8,R1
4	S	N	W	E	R6,R3,R4,R5
5	S	W	N	E	R6,R5
6	S	E	W	N	R6,R7,R4,R1
7	E	W	S	N	R8,R1
8	E	W	N	S	none
9	E	N	W	S	R1,R4

Figure 6.5: (a) Diagram of a 4×4 microring switch with example routing paths highlighted. Added to the diagram are proposed in-situ silicon photodiodes for the purpose of implementing a control system. (b) Closeup of switch fabric, showing two microrings in series. Use of orthogonal dithering frequencies (indicate as ω_D) can allow each microring to generate independent error signals ($E.S.$). (c) Table indicating routing logic for all possible input-output states of the switch (adapted from [15]).

the functionality of a 1×2 switch. Hence, the control system we demonstrated prior can be adapted to enable localized control of each microring as a 1×2 switch. A global control can then control the sequencing of the specific 1×2 switches to enable to the 4×4 configuration desired. Fig. 6.6 shows the sequencing table required to achieve the configuration (highlighted paths) shown in Fig. 6.5(a). Note that for any given path configuration there may be some microrings which will not be relevant, and hence the control system for those specific microrings can be disabled to achieve better energy efficiency.

Lastly, an inherent difficulty is the presence of multiple photodiodes in the down-

Sequence #	Microring	Action
1	R2	Lock-On
2	R8	Lock-On
3	R7	Lock-Off
4	R3	Lock-On
5	R1	Lock-Off
6	R5	Lock-On
7	R4	Disable Control
8	R6	Disable Control

Figure 6.6: Table showing proposed sequencing of microring resonators in a 4×4 microring switch for path configuration shown highlighted in Fig. 6.5

stream path of a microring resonator. To resolve this, the othogonality principle can be leveraged (Eq. 4.2), as shown in Fig. 6.5(b). By using a set of orthogonal dithering frequencies, the dithering signal received on the photodiode from non-relevant microring resonators is filtered away when generating the error signal.

6.3 Conclusion

We have further demonstrated the power and utility of the dithering mechanism by adapting it for a microring-based switch, and illustrating how the control system could be extended to large-radix microring switches. Additionally, we have demonstrated thermal stabilization of a microring switch enduring thermal fluctuations of magnitude 20 K, a range that is equivalent to the magnitude of thermal fluctuations in such applications as data centers [97].

While no data measurements were performed in this demonstration, the results of chapter 5 had shown rigorously the compatibility of the dithering mechanism with high-speed data. The demonstration can easily be extended by improving the device characteristics: embedding a *p-i-n* junction to have high-speed electro optic switching, leaving the localized integrated heater purely for thermal stabilization. Additionally, the FSR should be reengineered to be smaller, matching the wavelength grid used in

WDM and DWDM applications (100 GHz and smaller). Then the microring switch can be demonstrated as it switches high-speed WDM streams [95], albeit with a full control system thermally stabilizing the device.

Chapter 7

Simplified Platforms for Microring-Sensing using Wavelength Locking

The work in the prior chapters described innovative techniques to wavelength lock and stabilize microring resonators for the purpose of high-speed optical interconnects. In this chapter, the author adapts those developed techniques to demonstrate a simplified platform for microring sensors.

The notable contributions of this work:

- Adaptation of wavelength locking a microring resonator for the purpose of measuring sensing-induced resonance shifts.
- Measurement of resonance shifts with $\sigma = 7$ pm, demonstrating validity of technique.

7.1 Microring Resonators for Sensing Applications

With their small footprint, CMOS-compatible fabrication, and multiplexed operation, silicon microring resonators are ideal for use as measurement devices. Their high-refractive index provides them with a high sensitivity to such environmental factors such as temperature, and when chemically treated, they can be used as effective label-free biosensors [98, 99, 100]. The latter use has received wide attention for its potential to provide fast, compact, and cost- effective diagnostic instrumentation for applications

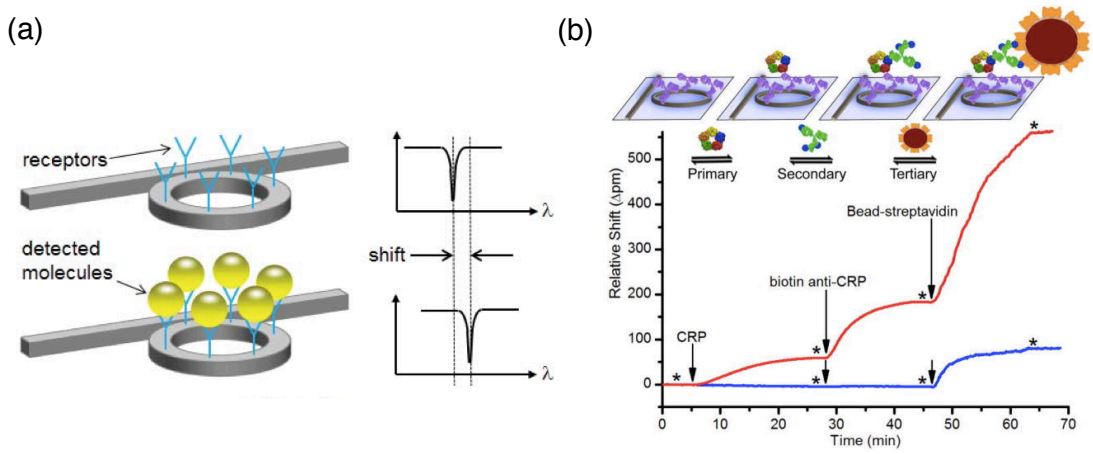

Figure 7.1: (a) Illustration of a chemically treated microring and the induced shift in its resonance from reaction with biochemical molecules (adapted from [18]). (b) Measurements from a microring sensor showing typical resonance shifts on the order of 100s of *pm*. (adapted from [19]).

in environmental monitoring, biochemistry, and healthcare; and as a testament to its utility, has been implemented commercially in that capacity.

7.2 Microring-Sensing using Wavelength Locking

The routine procedure for using the microring resonator as a sensor is to probe the resonance shift of the resonator as it is exposed to the environment or sample (Fig. 7.3(a) illustrates this resonance shift). The traditional technique for measuring this resonance shift consists of conducting fast spectral scans with a tunable laser and photodiode, or a broadband source, monochromator, and photodiode [100]. However, the use of costly, bulky, and sensitive equipment such as tunable lasers and monochromators is prohibitive to the desired deployment of microring resonators as low-cost, portable, and robust sensors.

Prior attempts to address this issue have utilized electrical tracing using cascaded microring structures with a high-speed detector, and wavelength locking using a tunable laser [101, 102]. In this work we show that the wavelength locking techniques detailed in chapter 4 can be adapted to perform direct electrical readouts of the sensing-induced resonance shifts.

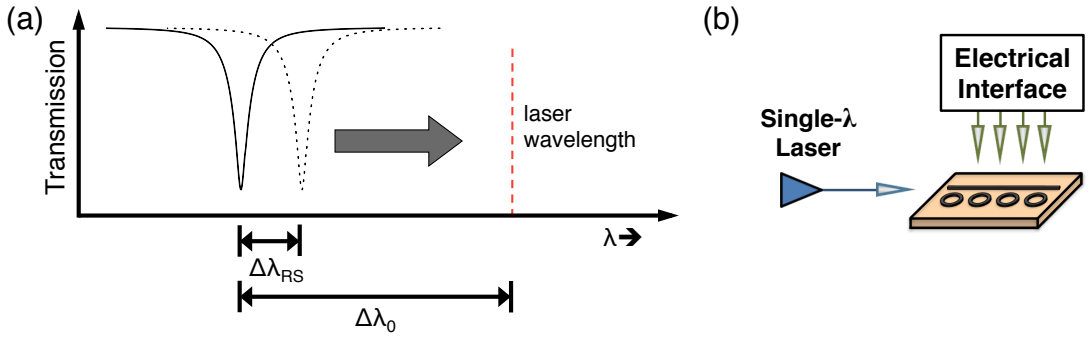

Figure 7.2: (a) Illustration of induced resonance shifts and wavelength locking. (b) Microring-sensing platform using wavelength locking.

Fig. 7.2(a) illustrates specifically how wavelength locking can be used to directly measure the sensing-induced resonance shift. In its initial state, the microring needs to be tuned a distance $\Delta\lambda_0$ as shown in Fig. 7.2(a) during the wavelength locking process. However, following exposure to the sample or environmental condition, a resonance shift $\Delta\lambda_{RS}$ will be induced in the microring. Subsequently, the microring will then be needed to tune $(\Delta\lambda_0 - \Delta\lambda_{RS})$ to be wavelength locked to the fixed laser. The voltage on the integrated heater required to wavelength lock in these two scenarios will change, and is defined as

$$V = \sqrt{R_H(\Delta\lambda_0 - \Delta\lambda_{RS})(\partial\lambda/\partial P)^{-1}} \tag{7.1}$$

where R_H is the resistance of the heater, and $\partial\lambda/\partial P$ is the tuning efficiency of the heater.

By wavelength locking the resonator and sampling the voltage applied to the heater during the wavelength locked state we retrieve a direct measurement of the resonance shift, with no additional post-processing needed. Fig. 7.2(b) shows the implementation of our method, which requires only a single-point optical coupling (assuming on-chip photodetectors) of a single-wavelength laser (where the specific wavelength can be arbitrary).

To demonstrate the described technique, we reutilized the silicon microring device previously described in chapter 4. Ideally, the demonstration would show the simplified sensing technique for a biochemical application. However, showing the technique working for any sensing-induced resonance shift would be enough for a proof-of-principle,

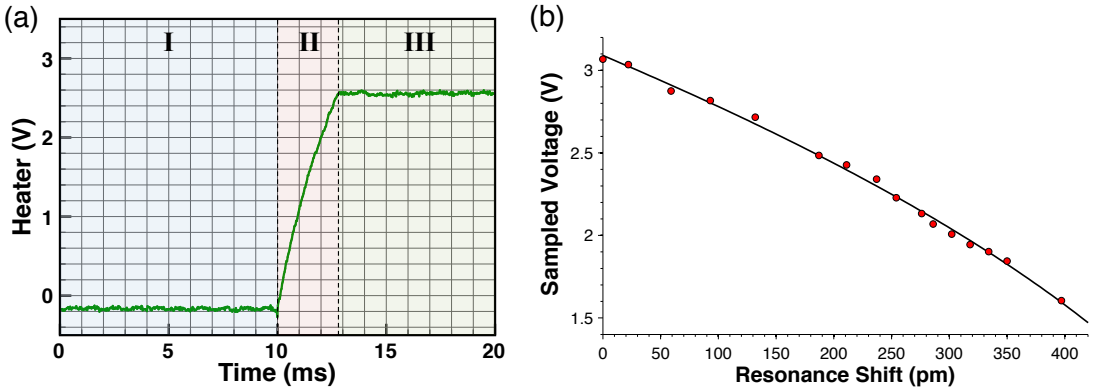

Figure 7.3: (a) Heater voltage during the wavelength locking sequence. Sampling of the voltage takes place in the hold state (III). (b) Measured data points fitted to Eq. 7.1.

with the results being directly translatable to biochemical sensing. For this reason, we utilized the natural temperature sensitivity of the microring resonator to demonstrate the technique. By placing the chip on a thermo-electric cooler (TEC) platform, the temperature of the microring resonator could easily be changed, inducing a resonance shift via the thermo-optic effect.

As had been previously shown in chapter 4, Fig. 7.3(a) shows the heater voltage during the wavelength locking process when using the dithering mechanism. As annotated on the graph, the voltage is ramped to tune the microring to the laser wavelength (II), and when the microring is wavelength locked to the laser (III), the voltage is sampled in order to measure the resonance shift. To gather measurements using the technique, we experimentally varied the resonance shift, $\Delta\lambda_{RS}$, by cooling the chip using a TEC. $\Delta\lambda_{RS}$ was measured using spectral scans, and simultaneously measured using our wavelength locking technique. The measurement was able to measure resonance shifts with $\sigma = 7$ pm (calculated against the fitted curve, Fig. 7.3(b)), validating its ability to measure resonance shifts accurately.

Limitations on the accuracy of the technique can be attributed to the experimental setup. Specifically, Fabry-Perot artifacts in the drop port (where the photodiode was located) resulted in a drop port response that deviated from the through port response. It is expected that re-iteration of the device and the experimental design could produce significantly better accuracy in the measurement results. Regardless, the demonstrated accuracy ($\sigma = 7$ pm) is sufficient for use with current implementations of microring

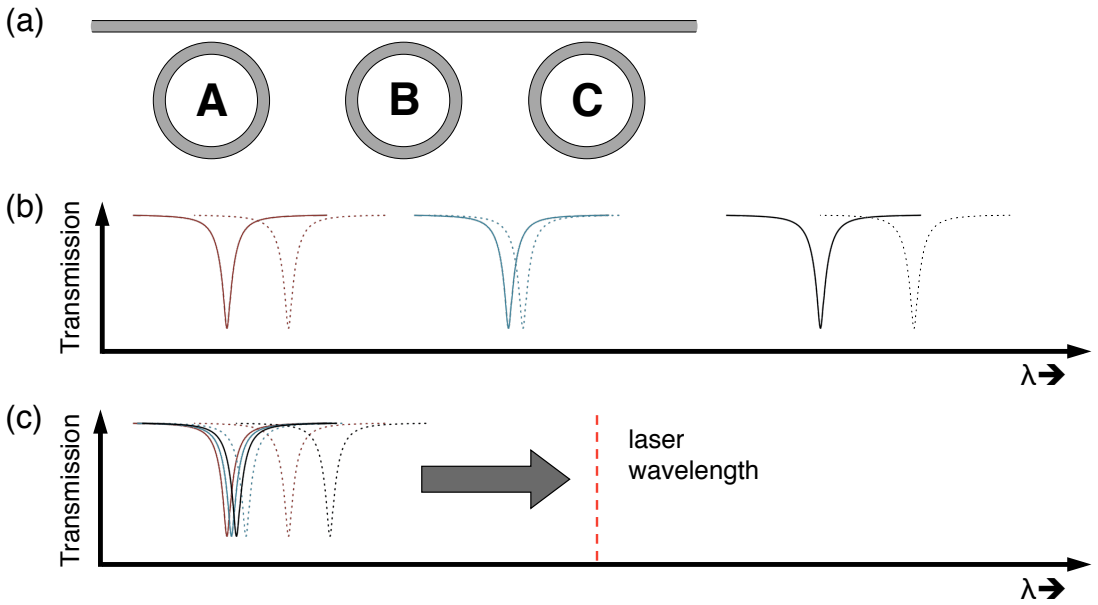

Figure 7.4: (a) Illustration of cascaded microrings, each treated with a different analyze to give it unique sensing properties. (b) Optical spectrum when using traditional method of extracting readout from multiplexed cascaded microrings. (c) Optical spectrum when adapting wavelength locking technique to multiplexed microring sensors.

sensors (which typically have resonance shifts on the order of 100s of pm, see Fig. 7.1(b)).

7.2.1 Multiplexed Microring Sensor Readout using Wavelength Locking

The advantages of the demonstrated wavelength locking technique intensify when adapting it to multiplexed microring sensors. As described in chapter 1, microrings are frequently cascaded to enable WDM optical links. For biochemical sensing applications, cascaded microrings are motivated for multiplexed sensing applications. As illustrated in Fig. 7.4(a), in a cascaded arrangement, each microring is treated with a different analyte such that they are sensitive to unique biochemical agents in the sample. The traditional method for measuring the resonance shift of each microring requires performing a wavelength scan across the spectrum that the resonances occupy. To avoid overlap between resonances, the microrings must be carefully fabricated such that they are spectrally well spaced (as seen in Fig. 7.4(b)). The increased fabrication toler-

ances required, as well as the additional post-processing of the spectrum data, makes it difficult to manifest multiplexed microring sensors successfully.

In contrast, using the wavelength locking technique the prior issues can easily be resolved. In our platform, microrings can be fabricated with identical dimensions (spectrally overlapping), as the wavelength locking mechanism can sequentially probe and discern individual microrings. Fig. 7.4(c) illustrates this process. Consequently, an additional advantage is that the number of microring sensors that can be cascaded is not limited by the available spectrum (which is dictated by the FSR of the microring).

7.3 Conclusion

This initial proof-of-principle demonstration validated the use of the wavelength locking for direct electrical readout of a microring sensor. By requiring only a single-wavelength laser source (in contrast to a tunable laser or monochromator), our demonstrated platform is orders of magnitude more cost-effective, robust, and compact than current microring-sensing platforms. Additionally, as was shown in section 4.5, μs-scale wavelength locking is possible, allowing rapid sampling of microring sensors, even when they are in multiplexed configurations as was discussed in section 7.2.1.

Finally, we note that for applications in which the integrated heater cannot be situated directly above the microring, there are demonstrated configurations that enable microring tuning while delocalizing the position of the integrated heater and microring [103].

Chapter 8

Summary and Conclusion

8.1 Summary of Contributions

The work of the author developed and validated two powerful methods to stabilize microring resonators: power monitoring (as applied to microring modulators), and the use of dithering signals (applicable to the general class of microring-based devices). These methods were embodied in experimental control systems that rigorously showed their validity in high-speed data applications. Furthermore, the provided analysis provides argument that they can be successfully incorporated into commercial implementations. Demonstration of their ability to be abstracted in a FPGA implementation provides evidence that these implemented control systems can scale in size to match even the most complex microring-based systems.

The developed control systems have been demonstrated to resolve the current thermal and fabrication issues that have plagued microring-based devices, and may hence be the enabling factor in their commercial deployment.

8.2 Recommendations for Future Work

A number of immediate projects can be pursued to extend the fundamental work developed in this dissertation:

- Thermally stabilize a microring modulator using power monitoring in which the power monitoring is conducted not using a separate photodiode, but photodetection in the driving p-n junction itself. It has been shown prior that when reverse

biased, the modulator's *p*-*n* junction generates a photocurrent that can be used for power monitoring [104].

- ASIC implementations of the discussed control circuitry to verify their energy-efficiency and circuit footprint characteristics.
- An initialization and thermal stabilization of a full WDM microring-based link, in which all photonic transmit and receive elements besides the lasers have been implemented on-chip.
- Incorporation of the FPGA implementation of the control systems into the demonstrated high-speed FPGA-based optical link demonstrations [81]. The resultant FPGA system would allow full prototyping of a silicon photonic interconnect from the physical layer to the application layer.

There is also the great potential to scale the use of dithering signals (using the principles outlined in the dissertation) to larger and more complex microring-based devices:

- As detailed in chapter 6, implement a control system for a high-radix microring switch (such as a 4×4 microring switch), scaling the control methodology presented for a 1×2 switch by abstracting control with a global routing logic to configure which microrings should be "on" and "off".
- Implement the dithering mechanism to stabilize higher-order microring switches. These switches possess better passband and extinction metrics, but the individual tuning of each microring (and their corresponding spectral inter-dependencies) is typically considered an impediment in their use.
- Extend the results of chapter 6 by redesigning the 1×2 microring switch such that it has a smaller FSR (to be capable of comb switching). Include a high-speed electrical junction to show *ns*-scale switching while simultaneously thermally stabilizing the switch using an integrated heater.

Because the work on control systems for microring-based devices had prior been so nascent, many architecture studies on microring-based systems omitted or assumed parameters related to the control of the many microring resonators comprising said

systems. Leveraging the work on energy-efficiency and latency of control systems performed in this dissertation, these studies can now gain more accuracy:

- An architecture study incorporating the latency and energy consumption tradeoffs of initializing and stabilizing microring-based interconnects.
- Incorporation of latency metrics into microring-based switch metrics, accounting for the reconfiguration time when reprovisioning optical paths.
- An architecture study on the energy consumption of thermally stabilizing microring-based systems in varying ambient temperature environments (such as would be found in target application areas such as data centers).

Lastly, in the realm of sensing applications, the author's work had demonstrated a proof-of-princple method to perform a direct electrical readout of the microring sensor. This of course can be improved upon by extension to a biochemical sensing application.

- Implementation of the simplified microring sensor platform in which the microring is sensitive to an applied biochemical agent, perhaps utilizing an re-engineered structure to allow both an integrated heater and sampling region to co-exist [103].
- Measurement of the wavelength locking technique's precision in ascertaining the resonance shift of the microring (our initial work was limited by Fabry Perot artifacts).

8.3 Final Remarks

Beyond the advantages of energy-efficiency and economy that the silicon photonic platform provides is the ability of the platform to manifest an incredible amount of photonic functionality in a single chip. The advantage of the silicon photonic platform lies not in the metrics of a single device, but the ability to mass produce complex photonic systems, analogous to the ability in the microelectronics world to manufacture complex systems from fundamental building blocks.

Also similar to microelectronics, the focus of research will correspondingly shift from the demonstration of individual devices to instead the demonstration of full systems. Within the research community, the recent emergence of foundry services that provide

reliable devices have the potential to usher in an age of sophisticated photonic systems for high-speed data, biophotonics, analog photonics, optical processing and yet to be envisioned applications.

Within that context, the role of control systems, such as the ones demonstrated in this dissertation, will will continue to grow in importance and scale as the number of photonic elements in an integrated chip continues to increase.

References

[1] Cary Gunn. **Silicon Photonics: Poised to Invade Local Area Networks**. *Photonics Spectra*, **40**(3):62–69, 2006. v, 2

[2] Benjamin G Lee, Xiaogang Chen, Aleksandr Biberman, Xiaoping Liu, I-Wei Hsieh, Cheng-Yun Chou, Jerry I Dadap, Fengnian Xia, William MJ Green, Lidija Sekaric, et al. **Ultrahigh-bandwidth silicon photonic nanowire waveguides for on-chip networks**. *Photonics Technology Letters, IEEE*, **20**(6):398–400, 2008. v, 3

[3] Fang Xu and Andrew W Poon. **Silicon cross-connect filters using microring resonator coupled multimode-interference-based waveguide crossings**. *Optics express*, **16**(12):8649–8657, 2008. v, 1, 3

[4] Solomon Assefa, Fengnian Xia, Stephen W Bedell, Ying Zhang, Teya Topuria, Philip M Rice, and Yurii A Vlasov. **CMOS-integrated high-speed MSM germanium waveguide photodetector**. *Optics express*, **18**(5):4986–4999, 2010. v, 1, 3

[5] Hao Xu, Xi Xiao, Xianyao Li, Yingtao Hu, Zhiyong Li, Tao Chu, Yude Yu, and Jinzhong Yu. **High speed silicon Mach-Zehnder modulator based on interleaved PN junctions**. *Optics express*, **20**(14):15093–15099, 2012. v, 3

[6] Long Chen. **Silicon Photonic Integrated Circuits for WDM Technology and Optical Switch**. In *Optical Fiber Communication Conference*, pages OW1C–1. Optical Society of America, 2013. v, 3

[7] Qianfan Xu, David Fattal, and Raymond G. Beausoleil. **Silicon microring resonators with 1.5-μm radius**. *Opt. Express*, **16**(6):4309–4315, Mar 2008. v, 6, 7

[8] Andrea Guarino, Gorazd Poberaj, Daniele Rezzonico, Riccardo Degl'Innocenti, and Peter Günter. **Electro–optically tunable microring resonators in lithium niobate**. *Nature Photonics*, **1**(7):407–410, 2007. v, 6

[9] Xiaomin Zhang and Andrea M Armani. **Silica microtoroid resonator sensor with monolithically integrated waveguides**. *Opt. Express*, **21**(20):23592–23603, Oct 2013. v, 6

[10] Alexander Spott, Yang Liu, Tom Baehr-Jones, Rob Ilic, and Michael Hochberg. **Silicon waveguides and ring resonators at 5.5 μm**. *Applied Physics Letters*, **97**(21):–, 2010. v, 6

[11] Jacob S Levy, Alexander Gondarenko, Mark A Foster, Amy C Turner-Foster, Alexander L Gaeta, and Michal Lipson. **CMOS-compatible multiple-wavelength oscillator for on-chip optical interconnects**. *Nature Photonics*, **4**(1):37–40, 2009. v, 6

[12] M. Pantouvaki, Hui Yu, M. Rakowski, P. Christie, P. Verheyen, G. Lepage, N. Van Hoovels, P. Absil, and J. Van Campenhout. **Comparison of Silicon Ring Modulators With Interdigitated and Lateral p-n Junctions**. *Selected Topics in Quantum Electronics, IEEE Journal of*, **19**(2):7900308–7900308, March 2013. vi, 7

[13] Jie Teng, Pieter Dumon, Wim Bogaerts, Hongbo Zhang, Xigao Jian, Xiuyou Han, Mingshan Zhao, Geert Morthier, and Roel Baets. **Athermal Silicon-on-insulator ring resonators by overlaying a polymer cladding on narrowed waveguides**. *Opt. Express*, **17**(17):14627–14633, 2009. vi, 9, 11, 12

[14] Biswajeet Guha, Bernardo BC Kyotoku, and Michal Lipson. **CMOS compatible athermal silicon microring resonators**. *arXiv preprint arXiv:0911.3444*, 2009. vi, 13, 14

[15] Nicolás Sherwood-Droz, Howard Wang, Long Chen, Benjamin G Lee, Aleksandr Biberman, Keren Bergman, and Michal Lipson. **Optical 4x4 hitless slicon router for optical networks-on-chip (NoC)**. *Opt. Express*, **16**(20):15915–15922, 2008. vi, xii, 7, 14, 16, 21, 57, 74, 76

[16] Michael R Watts, William A Zortman, Douglas C Trotter, Gregory N Nielson, David L Luck, and Ralph W Young. **Adiabatic resonant microrings (ARMs) with directly integrated thermal microphotonics**. In *Conference on Lasers and Electro-Optics*. Optical Society of America, 2009. vi, 17, 61

[17] Po Dong, Wei Qian, Hong Liang, Roshanak Shafiiha, Dazeng Feng, Guoliang Li, John E Cunningham, Ashok V Krishnamoorthy, and Mehdi Asghari. **Thermally tunable silicon racetrack resonators with ultralow tuning power**. *Optics Express*, **18**(19):20298–20304, 2010. vi, 18

[18] Benjamin G Lee, Jean-Olivier Plouchart, Alexander V Rylyakov, Jeong Hwan Song, Fuad E Doany, and Clint L Schow. **Passive photonics in an unmodified CMOS technology with no post-processing required**. *IEEE Photonics Technology Letters*, **25**:393–396, 2013. xii, 1, 80

[19] Matthew S Luchansky, Adam L Washburn, Melinda S McClellan, and Ryan C Bailey. **Sensitive on-chip detection of a protein biomarker in human serum and plasma over an extended dynamic range using silicon photonic microring resonators and sub-micron beads**. *Lab on a Chip*, **11**(12):2042–2044, 2011. xii, 80

[20] Ashok V Krishnamoorthy, Ron Ho, Xuezhe Zheng, Herb Schwetman, Jon Lexau, Pranay Koka, GuoLiang Li, Ivan Shubin, and John E Cunningham. **Computer systems based on silicon photonic interconnects**. *Proceedings of the IEEE*, **97**(7):1337–1361, 2009. 1, 43, 57

[21] Ryohei Urata, Hong Liu, Cedric Lam, Pedram Dashti, and Chris Johnson. **Silicon Photonics for Optical Access Networks**. In *Group IV Photonics*, page 3, Washington DC, 2012. 1

[22] Po Dong, Wei Qian, Shirong Liao, Hong Liang, Cheng-Chih Kung, Ning-Ning Feng, Roshanak Shafiiha, Joan Fong, Dazeng Feng, Ashok V Krishnamoorthy, et al. **Low loss shallow-ridge silicon waveguides**. *Optics express*, **18**(14):14474–14479, 2010. 1

[23] William M Green, Michael J Rooks, Lidija Sekaric, and Yurii A Vlasov. **Ultra-compact, low RF power, 10 Gb/s silicon Mach-Zehnder modulator**. *Optics express*, **15**(25):17106–17113, 2007. 1

[24] Stanley T Cheung, Binbin Guan, Stevan S Djordjevic, Katsunari Okamoto, and SJ Yoo. **Low-loss and high contrast silicon-on-insulator (SOI) arrayed waveguide grating**. In *CLEO: Science and Innovations*, pages CM4A–5. Optical Society of America, 2012. 1

[25] Christopher T DeRose, Douglas C Trotter, William A Zortman, Andrew L Starbuck, Moz Fisher, Michael R Watts, and Paul S Davids. **Ultra compact 45 GHz CMOS compatible Germanium waveguide photodiode with low dark current**. *Optics express*, **19**(25):24897–24904, 2011. 1

[26] Noam Ophir, Christopher Mineo, David Mountain, and Keren Bergman. **A Silicon Photonic Microring Link Case Study for High-Bandwidth Density Low-Power Chip I/O**. *Micro*, 2013. 2, 8, 10, 51, 52, 109

[27] A. Yariv. **Universal relations for coupling of optical power between microresonators and dielectric waveguides**. *Electronics Letters*, **36**(4):321–322, Feb 2000. 3, 4, 111

[28] J. Heebner, R. Grover, T. Ibrahim, and T.A. Ibrahim. *Optical Microresonators: Theory, Fabrication, and Applications*. Optical Sciences, 138. Springer, 2008. 3

[29] W. Bogaerts, P. De Heyn, T. Van Vaerenbergh, K. De Vos, S. Kumar Selvaraja, T. Claes, P. Dumon, P. Bienstman, D. Van Thourhout, and R. Baets. **Silicon microring resonators**. *Laser and Photonics Reviews*, **6**(1):47–73, 2012. 5, 6

[30] Qianfan Xu, Bradley Schmidt, Sameer Pradhan, and Michal Lipson. **Micrometre-scale silicon electro-optic modulator**. *Nature*, **435**(7040):325–327, 2005. 7

[31] Long Chen and Michal Lipson. **Ultra-low capacitance and high speed germanium photodetectors on silicon**. *Opt. Express*, **17**(10):7901–7906, 2009. 7, 8

[32] Aleksandr Biberman, Hugo LR Lira, Kishore Padmaraju, Noam Ophir, Johnnie Chan, Michal Lipson, and Keren Bergman. **Broadband silicon photonic electrooptic switch for photonic interconnection networks**. *Photonics Technology Letters, IEEE*, **23**(8):504–506, 2011. 7

[33] Guoliang Li, Xuezhe Zheng, Jin Yao, Hiren Thacker, Ivan Shubin, Ying Luo, Kannan Raj, John E Cunningham, and Ashok V Krishnamoorthy. **25Gb/s 1V-driving CMOS ring modulator with integrated thermal tuning**. *Optics express*, **19**(21):20435–20443, 2011. 7, 108, 109

[34] Xi Xiao, Hao Xu, Xianyao Li, Zhiyong Li, Tao Chu, Jinzhong Yu, and Yude Yu. **60 Gbit/s Silicon Modulators with Enhanced Electro-optical Efficiency**. In *Optical Fiber Communication Conference/National Fiber Optic Engineers Conference 2013*, page OW4J.3. Optical Society of America, 2013. 7

[35] B.G. Lee, B.A. Small, Qianfan Xu, M. Lipson, and K. Bergman. **Characterization of a 4 x 4 Gb/s Parallel Electronic Bus to WDM Optical Link Silicon Photonic Translator**. *Photonics Technology Letters, IEEE*, **19**(7):456–458, April 2007. 8, 117

[36] Ali Ayazi, Tom Baehr-Jones, Yang Liu, Andy Eu-Jin Lim, and Michael Hochberg. **Linearity of silicon ring modulators for analog optical links**. *Opt. Express20 (12)*, pages 13115–13122, 2012. 8

[37] Michael Georgas, Jonathan Leu, Benjamin Moss, Chen Sun, and Vladimir Stojanovic. **Addressing link-level design tradeoffs for integrated photonic interconnects**. In *Custom Integrated Circuits Conference (CICC), 2011 IEEE*, pages 1–8. IEEE, 2011. 8, 44

[38] Magdalena S Nawrocka, Tao Liu, Xuan Wang, and Roberto R Panepucci. **Tunable silicon microring resonator with wide free spectral range**. *Applied physics letters*, **89**(7):071110–071110, 2006. 9

[39] Qing Fang, Junfeng Song, Xianshu Luo, Lianxi Jia, Mingbin Yu, Guoqiang Lo, and Yuliang Liu. **High efficiency ring-resonator filter with NiSi heater**. *Photonics Technology Letters, IEEE*, **24**(5):350–352, 2012. 9, 18

[40] Payam Alipour, Ehsan Shah Hosseini, Ali Asghar Eftekhar, Babak Momeni, and Ali Adibi. **Athermal performance in high-Q polymer-clad silicon microdisk resonators**. *Optics letters*, **35**(20):3462–3464, 2010. 9, 11

[41] Kishore Padmaraju, Johnnie Chan, Long Chen, Michal Lipson, Keren Bergman, et al. **Thermal stabilization of a microring modulator using feedback control**. *Opt. Express20 (27)*, pages 27999–28008, 2012. 9

[42] Andrew P Knights, Edgar Huante-Ceron, Jason Ackert, Dylan Logan, Greg Wojcik, Feng Zhang, Alexey Gubenko, and Sergey Mikhrin. **Comb-laser driven WDM for short reach silicon photonic based optical interconnection**. In *Group IV Photonics (GFP), 2012 IEEE 9th International Conference on*, pages 210–212. IEEE, 2012. 10

[43] D Livshits, D Yin, A Gubenko, I Krestnikov, S Mikhrin, A Kovsh, and G Wojcik. **Cost-effective WDM optical interconnects enabled by quantum dot comb lasers**. In *OPTO*, pages 76070W–76070W. International Society for Optics and Photonics, 2010. 10, 44

[44] Jacob S Levy, Kasturi Saha, Yoshitomo Okawachi, Mark A Foster, Alexander L Gaeta, and Michal Lipson. **High-performance silicon-nitride-based multiple-wavelength source**. *Photonics Technology Letters, IEEE*, **24**(16):1375–1377, 2012. 10

[45] Yasuo Kokubun, Norihide Funato, and Masanori Takizawa. **Athermal waveguides for temperature-independent lightwave devices**. *Photonics Technology Letters, IEEE*, **5**(11):1297–1300, 1993. 11

[46] Vivek Raghunathan, Winnie N Ye, Juejun Hu, Tomoyuki Izuhara, Jurgen Michel, and Lionel C Kimerling. **Athermal operation of silicon waveguides: spectral, second order and footprint dependencies**. *Optics express*, 2010. 11, 13

[47] Milan M Milosevic, Frederic Y Gardes, David J Thomson, and Goran Z Mashanovich. **Temperature insensitive racetrack resonators for near infrared applications**. In *Optical Fiber Communication Conference*. Optical Society of America, 2012. 11, 12

[48] Jong-Moo Lee, Duk-Jun Kim, Hokyun Ahn, Sang-Ho Park, and Gyungock Kim. **Temperature dependence of silicon nanophotonic ring resonator with a polymeric overlayer**. *Journal of lightwave technology*, **25**(8):2236–2243, 2007. 11

[49] Linjie Zhou, Ken Kashiwagi, Katsunari Okamoto, RP Scott, NK Fontaine, Dan Ding, Venkatesh Akella, and SJB Yoo. **Towards athermal optically-interconnected computing system using slotted silicon microring resonators and RF-photonic comb generation**. *Applied Physics A*, **95**(4):1101–1109, 2009. 11, 12

[50] Qing Li, Siva Yegnanarayanan, Mohammad Soltani, Payam Alipour, and Ali Adibi. **A temperature-insensitive third-order coupled-resonator filter for on-chip terabit/s optical interconnects**. *Photonics Technology Letters, IEEE*, **22**(23):1768–1770, 2010. 11

[51] Vivek Raghunathan, Stefano Grillanda, Vivek Singh, Antonio Canciamilla, Francesco Morichetti, Anuradha Agarwal, Jurgen Michel, Andrea Melloni, and Lionel C Kimerling. **Trimming of Athermal Silicon Resonators**. In *Integrated Photonics Research, Silicon and Nanophotonics*. Optical Society of America, 2012. 12

[52] Feng Qiu, Feng Yu, Andrew M Spring, and Shiyoshi Yokoyama. **Athermal silicon nitride ring resonator by photobleaching of Disperse Red 1-doped poly (methyl methacrylate) polymer**. *Optics Letters*, **37**(19):4086–4088, 2012. 12

[53] Vivek Raghunathan, Tomoyuki Izuhara, Jurgen Michel, and Lionel Kimerling. **Stability of polymer-dielectric bi-layers for athermal silicon photonics**. *Optics Express*, **20**(14):16059–16066, 2012. 12

[54] Kuanping Shang, Stevan S Djordjevic, Jun Li, Ling Liao, Juthika Basak, Hai-Feng Liu, and SJ Yoo. **CMOS-compatible Titanium Dioxide Deposition for Athermalization of Silicon Photonic Waveguides**. In *CLEO: Science and Innovations*. Optical Society of America, 2013. 12

[55] Shiyang Zhu, Guoqiang Lo, and Dim-Lee Kwong. **Towards Athermal Nanoplasmonic Resonators Based on Cu-TiO_2-Si Hybrid Plasmonic Waveguide**. In *Optical Fiber Communication Conference*. Optical Society of America, 2013. 12

[56] Stevan S Djordjevic, Kuanping Shang, Binbin Guan, Stanley TS Cheung, Ling Liao, Juthika Basak, Hai-Feng Liu, and SJB Yoo. **CMOS-compatible, athermal silicon ring modulators clad with titanium dioxide**. *Optics Express*, **21**(12):13958–13968, 2013. 12

[57] Payam Alipour, Amir Hossein Atabaki, Ali Asghar Eftekhar, and Ali Adibi. **Athermal Performance In Titania-clad Microresonators On SOI**. In *Frontiers in Optics*. Optical Society of America, 2010. 12

[58] Mutsunori Uenuma and Teruaki Motooka. **Temperature-independent silicon waveguide optical filter**. *Optics letters*, **34**(5):599–601, 2009. 13

[59] Biswajeet Guha, Alexander Gondarenko, and Michal Lipson. **Minimizing temperature sensitivity of silicon Mach-Zehnder interferometers**. *Opt. Express*, **18**(3):1879–1887, 2010. 13

[60] Biswajeet Guha, Kyle Preston, and Michal Lipson. **Athermal silicon microring electro-optic modulator**. *Optics Letters*, **37**(12):2253–2255, 2012. 13

[61] Long Chen, Kyle Preston, Sasikanth Manipatruni, and Michal Lipson. **Integrated GHz silicon photonic interconnect with micrometer-scale modulators and detectors**. *arXiv preprint arXiv:0907.0022*, 2009. 14, 23, 104

[62] John E Cunningham, Ivan Shubin, Xuezhe Zheng, Thierry Pinguet, Attila Mekis, Ying Luo, Hiren Thacker, Guoliang Li, Jin Yao, Kannan Raj, et al. **Highly-efficient thermally-tuned resonant optical filters**. *Opt. Express*, **18**(18):19055–19063, 2010. 16, 18

[63] Han-Yong Ng, Michael R Wang, Daqun Li, Xuan Wang, Jose Martinez, Roberto R Panepucci, and Kachesh Pathak. **4×4 wavelength-reconfigurable photonic switch based on thermally tuned silicon microring resonators**. *Optical Engineering*, **47**(4):044601–044601, 2008. 16

[64] MM Geng, LX Jia, Lei Zhang, Lin Yang, Ping Chen, Tong Wang, YL Liu, et al. **Four-channel reconfigurable optical add-drop multiplexer based on photonic wire waveguide**. *Optics express*, 2009. 16

[65] Hui Yu, Marianna Pantouvaki, Sarvagya Dwivedi, Peter Verheyen, Guy Lepage, Roel Baets, Wim Bogaerts, Philippe Absil, and Joris Van Campenhout. **Compact, Thermally Tunable Silicon Racetrack Modulators Based on an Asymmetric Waveguide**. *Photonics Technology Letters*, 2013. 16

[66] F Gan, T Barwicz, MA Popovic, MS Dahlem, CW Holzwarth, PT Rakich, HI Smith, EP Ippen, and FX Kartner. **Maximizing the thermo-optic tuning range of silicon photonic structures**. In *Photonics in Switching, 2007*, pages 67–68. IEEE, 2007. 16

[67] Michael R Watts. **Adiabatic microring resonators**. *Optics letters*, **35**(19):3231–3233, 2010. 17

[68] Christopher T DeRose, Michael R Watts, Douglas C Trotter, David L Luck, Gregory N Nielson, and Ralph W Young. **Silicon microring modulator with integrated heater and temperature sensor for thermal control**. In *Conference on Lasers and Electro-Optics*. Optical Society of America, 2010. 17

[69] William Zortman, Anthony Lentine, Douglas Trotter, and Michael Watts. **Integrated CMOS Comaptible Low Power 10 Gbps Silicon Photonic Heater Modulator**. In *Optical Fiber Communication Conference*. Optical Society of America, 2012. 17, 43

[70] Po Dong, Wei Qian, Hong Liang, Roshanak Shafiiha, Ning-Ning Feng, Dazeng Feng, Xuezhe Zheng, Ashok V Krishnamoorthy, and Mehdi Asghari. **Low power and compact reconfigurable multiplexing devices based on silicon microring resonators**. *Optics Express*, **18**(10):9852–9858, 2010. 17

[71] Ivan Shubin, Guoliang Li, Xuezhe Zheng, Ying Luo, Hiren Thacker, Jin Yao, Namseok Park, Ashok V Krishnamoorthy, and John E Cunningham. **Integration, processing and performance of low power thermally tunable CMOS-SOI WDM resonators**. *Optical and Quantum Electronics*, **44**(12-13):589–604, 2012. 18

[72] Yu-Hsin Chen, Chen Sun, and V Stojanovic. **Scalable electrical-optical thermal simulator for multi-cores with optical interconnects**. In *Optical Interconnects Conference, 2013 IEEE*, pages 3–4. IEEE, 2013. 18, 43

[73] Xuezhe Zheng, Ying Luo, Guoliang Li, Ivan Shubin, Hiren Thacker, Jin Yao, Kannan Raj, John E Cunningham, and Ashok V Krishnamoorthy. **Enhanced optical bistability from self-heating due to free carrier absorption in substrate removed silicon ring modulators**. *Optics Express*, **20**(10):11478–11486, 2012. 18

[74] Qi Li, Noam Ophir, Lin Xu, Kishore Padmaraju, Long Chen, Michal Lipson, and Keren Bergman. **Experimental characterization of the optical-power upper bound in a silicon microring modulator**. In *Optical Interconnects Conference, 2012 IEEE*, pages 38–39. IEEE, 2012. 18

[75] Christopher T DeRose, Michael R Watts, Douglas C Trotter, David L Luck, Gregory N Nielson, and Ralph W Young. **Silicon microring modulator with integrated heater and temperature sensor for thermal control**. In *Conference on Lasers and Electro-Optics*, page CThJ3. Optical Society of America, 2010. 19

[76] Ciyuan Qiu, Jie Shu, Zheng Li, Xuezhi Zhang, and Qianfan Xu. **Wavelength tracking with thermally controlled silicon resonators**. *Optics express*, **19**(6):5143–5148, 2011. 20

[77] Erman Timurdogan, Aleksandr Biberman, Douglas C Trotter, Chen Sun, Michele Moresco, Vladimir Stojanovic, and Michael R Watts. **Automated wavelength recovery for microring resonators**. In *CLEO: Science and Innovations*, pages CM2M–1. Optical Society of America, 2012. 20

[78] William A Zortman, Anthony L Lentine, Douglas C Trotter, and Michael R Watts. **Bit-Error-Rate Monitoring for Active Wavelength Control of Resonant Modulators**. *IEEE Micro*, **33**(1):0042–52, 2013. 20

[79] TW Hansch and B Couillaud. **Laser frequency stabilization by polarization spectroscopy of a reflecting reference cavity**. *Optics communications*, **35**(3):441–444, 1980. 20

[80] Jonathan Albert Cox, DC Trotter, and Andrew L Starbuck. **Integrated control of silicon-photonic micro-resonator wavelength via balanced homodyne locking**. In *Optical Interconnects Conference, 2013 IEEE*, pages 52–53. IEEE, 2013. 20

[81] Daniel Brunina, Xiaoliang Zhu, Kishore Padmaraju, Long Chen, Michal Lipson, and Keren Bergman. **10-Gb/s WDM optically-connected memory system using silicon microring modulators**. In *European Conference and Exhibition on Optical Communication*. Optical Society of America, 2012. 25, 68, 86

[82] Qianfan Xu, Sasikanth Manipatruni, Brad Schmidt, Jagat Shakya, and Michal Lipson. **12.5 Gbit/s carrier-injection-based silicon micro-ring silicon modulators**. *Opt. Express*, **15**(2):430–436, 2007. 25, 27, 103, 104, 107, 111, 114

[83] Sasikanth Manipatruni, Rajeev K Dokania, Bradley Schmidt, Nicolás Sherwood-Droz, Carl B Poitras, Alyssa B Apsel, and Michal Lipson. **Wide temperature range operation of micrometer-scale silicon electro-optic modulators**. *Optics letters*, **33**(19):2185–2187, 2008. 25

[84] Philip Amberg, Eric Chang, Frankie Liu, Jon Lexau, Xuezhe Zheng, Guoliang Li, Ivan Shubin, J Cunningham, A Krishnamoorthy, and Ron Ho. **A sub-400 fJ/bit thermal tuner for optical resonant ring modulators in 40 nm CMOS**. In *Digest of Technical Papers, IEEE Asian Solid-State Circuits Conference*, 2012. 32

[85] MW Geis, SJ Spector, ME Grein, JU Yoon, DM Lennon, and TM Lyszczarz. **Silicon waveguide infrared photodiodes with $>$ 35 GHz bandwidth and phototransistors with 50 AW^{-1} response**. *Optics express*, **17**(7):5193–5204, 2009. 35

[86] Jurgen Michel, Jifeng Liu, and Lionel C Kimerling. **High-performance Ge-on-Si photodetectors**. *Nature Photonics*, **4**(8):527–534, 2010. 35

[87] MW Geis, SJ Spector, ME Grein, RJ Schulein, JU Yoon, DM Lennon, CM Wynn, ST Palmacci, F Gan, FX Kńertner, et al. **All silicon infrared photodiodes: photo response and effects of processing temperature**. *Optics Express*, **15**(25):16886–16895, 2007. 35

[88] Dylan F Logan, Philippe Velha, Marc Sorel, Richard M De La Rue, Paul E Jessop, and Andrew P Knights. **Monitoring and tuning micro-ring properties using defect-enhanced silicon photodiodes at 1550 nm**. *Photonics Technology Letters, IEEE*, **24**(4):261–263, 2012. 35

[89] Vratislav Michal, Christophe Prmont, Gaël Pillonet, and Nacer Abouchi. **Single active element PID controllers**. In *Radioelektronika (RADIOELEKTRONIKA), 2010 20th International Conference*, pages 1–4. IEEE, 2010. 43

[90] Christian Jesus B Fayomi, Mohamad Sawan, and Gordon W Roberts. **Reliable circuit techniques for low-voltage analog design in deep submicron standard CMOS: a tutorial**. *Analog Integrated Circuits and Signal Processing*, **39**(1):21–38, 2004. 44, 56

[91] Ashok V Krishnamoorthy, Xuezhe Zheng, Guoliang Li, Jin Yao, Thierry Pinguet, Attila Mekis, Hiren Thacker, Ivan Shubin, Ying Luo, Kannan Raj, et al. **Exploiting CMOS manufacturing to reduce tuning requirements for resonant optical devices**. *Photonics Journal, IEEE*, **3**(3):567–579, 2011. 44, 65

[92] RWP Drever, John L Hall, FV Kowalski, J Hough, GM Ford, AJ Munley, and H Ward. **Laser phase and frequency stabilization using an optical resonator**. *Applied Physics B*, **31**(2):97–105, 1983. 47

[93] Kimmo Lasanen, Elvi Raisanen-Ruotsalainen, and Juha Kostamovaara. **A 1-V, self adjusting, 5-MHz CMOS RC-oscillator**. In *Circuits and Systems, 2002. ISCAS 2002. IEEE International Symposium on*, **4**, pages IV–377. IEEE, 2002. 56

[94] Chunhong Chen and Zheng Li. **A low-power CMOS analog multiplier**. *IEEE TRANSACTIONS ON CIRCUITS AND SYSTEMS PART 2 EXPRESS BRIEFS*, **53**(2):100, 2006. 57

[95] Benjamin G Lee, Aleksandr Biberman, Po Dong, Michal Lipson, and Keren Bergman. **All-optical comb switch for multiwavelength message routing in silicon photonic networks**. *Photonics Technology Letters, IEEE*, **20**(10):767–769, 2008. 70, 78

[96] Tom Baehr-Jones, Michael Hochberg, and Axel Scherer. **Photodetection in silicon beyond the band edge with surface states**. *Optics express*, **16**(3):1659–1668, 2008. 71

[97] Roger R Schmidt, EE Cruz, and M Iyengar. **Challenges of data center thermal management**. *IBM Journal of Research and Development*, **49**(4.5):709–723, 2005. 77

[98] Frank Vollmer and Lan Yang. **Review Label-free detection with high-Q microcavities: a review of biosensing mechanisms for integrated devices**. *Nanophotonics*, **1**(3-4):267–291, 2012. 79

[99] D-X Xu, M Vachon, A Densmore, R Ma, S Janz, A Delâge, J Lapointe, P Cheben, JH Schmid, E Post, et al. **Real-time cancellation of temperature induced resonance shifts in SOI wire waveguide ring resonator label-free biosensor arrays**. *Optics express*, **18**(22):22867–22879, 2010. 79

[100] Muzammil Iqbal, Martin A Gleeson, Bradley Spaugh, Frank Tybor, William G Gunn, Michael Hochberg, Tom Baehr-Jones, Ryan C Bailey, and L Cary Gunn. **Label-free biosensor arrays based on silicon ring resonators and high-speed optical scanning instrumentation**. *Selected Topics in Quantum Electronics, IEEE Journal of*, **16**(3):654–661, 2010. 79, 80

[101] Junfeng Song, Xianshu Luo, Xiaoguang Tu, Mi Kyoung Park, Jack Sheng Kee, Huijuan Zhang, Mingbin Yu, Guo-Qiang Lo, and Dim-Lee Kwong. **Electrical tracing-assisted dual-microring label-free optical bio/chemical sensors**. *Optics express*, **20**(4):4189–4197, 2012. 80

[102] Liron Stern, Ilya Goykhman, Boris Desiatov, and Uriel Levy. **Frequency locked micro disk resonator for real time and precise monitoring of refractive index**. *Optics letters*, **37**(8):1313–1315, 2012. 80

[103] Mohammad Soltani, James T Inman, Michal Lipson, and Michelle D Wang. **Electro-optofluidics: achieving dynamic control on-chip**. *Optics express*, **20**(20):22314–22326, 2012. 84, 87

[104] Hui Yu, Dietmar Korn, Marianna Pantouvaki, Joris Van Campenhout, Katarzyna Komorowska, Peter Verheyen, Guy Lepage, Philippe Absil, David Hillerkuss, Luca Alloatti, et al. **Using carrier-depletion silicon modulators for optical power monitoring**. *Optics letters*, **37**(22):4681–4683, 2012. 86

[105] Sasikanth Manipatruni, Long Chen, and Michal Lipson. **Ultra high bandwidth WDM using silicon microring modulators**. *Optics express*, **18**(16):16858–16867, 2010. 102, 117

[106] Guoliang Li, Ashok V Krishnamoorthy, Ivan Shubin, Jin Yao, Ying Luo, Hiren Thacker, Xuezhe Zheng, Kannan Raj, and John E Cunningham. **Ring Resonator Modulators in Silicon for Interchip Photonic Links**. *Selected Topics in Quantum Electronics, IEEE Journal of*, **19**(6):3401819–3401819, 2013. 103

[107] C Jeruchim. **Techniques for estimating the bit error rate in the simulation of digital communication systems**. *Selected Areas in Communications, IEEE Journal on*, **2**(1):153–170, 1984. 106

[108] Govind P Agrawal. *Fiber-optic communication systems*, **1**. Wiley-Interscience, 1997. 106, 108

[109] John E Heebner. *Nonlinear optical whispering gallery microresonators for photonics*. PhD thesis, University of Rochester, 2003. 106

[110] M Glick, P Watts, R Waegemans, P Bayvel, and RI Killey. **Electronic signal processing to improve system performance of optical interconnects**. In *Transparent Optical Networks, 2007. ICTON'07. 9th International Conference on*, **1**, pages 298–301. IEEE, 2007. 108

[111] Nicolás Sherwood-Droz, Kyle Preston, Jacob S Levy, and Michal Lipson. **Device guidelines for WDM interconnects using silicon microring resonators**. In *Workshop on the Interaction between Nanophotonic Devices and Systems (WINDS)*, **43**, pages 15–18, 2010. 109

[112] Alan H Gnauck and Peter J Winzer. **Optical phase-shift-keyed transmission**. *Journal of lightwave technology*, **23**(1):115, 2005. 110

[113] Lin Zhang, Jeng-Yuan Yang, Muping Song, Yunchu Li, Bo Zhang, Raymond G Beausoleil, and Alan E Willner. **Microring-based modulation and demodulation of DPSK signal**. *Optics express*, **15**(18):11564–11569, 2007. 111, 113

[114] Walid A Atia and Roy S Bondurant. **Demonstration of return-to-zero signaling in both OOK and DPSK formats to improve receiver sensitivity in an optically preamplified receiver**. In *LEOS'99. IEEE Lasers and Electro-Optics Society 1999 12th Annual Meeting*, **1**, pages 226–227. IEEE, 1999. 115

[115] Katsumi Iwatsuki and Jun-ichi Kani. **Applications and technical issues of wavelength-division multiplexing passive optical networks with colorless optical network units [Invited]**. *Journal of Optical Communications and Networking*, **1**(4):C17–C24, 2009. 117

[116] Po Dong, Chongjin Xie, Long Chen, Nicolas K Fontaine, and Young-kai Chen. **Experimental demonstration of microring quadrature phase-shift keying modulators**. *Optics Letters*, **37**(7):1178–1180, 2012. 118

Appendix A

Relevant Author Publications

- K. Padmaraju. X. Zhu, L. Chen, M. Lipson, K. Bergman. **Intermodulation Crosstalk Characteristics of WDM Silicon Microring Modulators.** IEEE Photonics Technology Letters, 26 (14), 2014.
- K. Padmaraju, L.-W. Luo, X. Zhu, M. Glick, R. Dutt, M. Lipson, K. Bergman. **Wavelength Locking of a WDM Silicon Microring Demultiplexer using Dithering Signals.** Optical Fiber Communication Conference (OFC), San Francisco, 2014.
- K. Padmaraju, D. F. Logan, T. Shiraishi, J. J. Ackert, A. P. Knights, K. Bergman. **Wavelength Locking and Thermally Stabilizing Microring Resonators using Dithering Signals.** IEEE Journal of Lightwave Technology, 32 (3), 2014.
- K. Padmaraju, D. F. Logan, X. Zhu, J. J. Ackert, A. P. Knights, K. Bergman. **Wavelength Locking of Microring Resonators and Modulators using a Dithering Signal.** European Conference on Optical Communications (ECOC), London, England, 2013.
- K. Padmaraju, K. Bergman. **Resolving the thermal challenges for silicon microring resonator devices.** Nanophotonics, 2 (4), 2013.
- K. Padmaraju, D. F. Logan, J. J. Ackert, A. P. Knights, K. Bergman. **Initialization and Stabilization of Microring Resonators for Next-Generation Silicon Photonic Interconnects.** SRC TechCon, Austin, 2013.

- K. Padmaraju, D. F. Logan, X. Zhu, J. J. Ackert, A. P. Knights, K. Bergman. **Integrated thermal stabilization of a microring modulator.** Optics Express, 21 (12), 2013.

- K. Padmaraju, D. F. Logan, X. Zhu, J. J. Ackert, A. P. Knights, K. Bergman. **Simplified Platform for Microring-Sensing using Wavelength Locking [post-deadline paper].** Conference on Lasers and Electro-Optics (CLEO), San Jose, 2013.

- K. Padmaraju, D. F. Logan, J. J. Ackert, A. P. Knights, K. Bergman. **Microring Resonance Stabilization using Thermal Dithering.** IEEE Optical Interconnects Conference, Santa Fe, 2013.

- K. Padmaraju, D. F. Logan, X. Zhu, J. J. Ackert, A. P. Knights, K. Bergman. **Integrated Thermal Stabilization of a Microring Modulator.** Optical Fiber Communication Conference (OFC), Anaheim, 2013.

- X. Zhu, K. Padmaraju, L. Chen, D. F. Logan, J. J. Ackert, A. P. Knights, M. Lipson, K. Bergman. **Pattern-Dependent Performance of Microring Modulators.** Optical Fiber Communication Conference, Anaheim, 2013.

- R. R. Grote, K. Padmaraju, B. Souhan, J. B. Driscoll, K. Bergman, R. M. Osgood. **10 Gb/s Error-Free Operation of All-Silicon Ion-Implanted-Waveguide Photodetectors at 1.55 um.** IEEE Photonics Technology Letters, 25 (1), 2013.

- K. Padmaraju, J. Chan, L. Chen, M. Lipson, K. Bergman. **Thermal stabilization of a microring modulator using feedback control.** Optics Express, 20 (27), 2012.

- D. Brunina, X. Zhu, K. Padmaraju, L. Chen, M. Lipson, K. Bergman. **10-Gb/s WDM Optically-Connected Memory System using Silicon Microring Modulators.** European Conference on Optical Communications (ECOC), Amsterdam, Netherlands, 2012.

- L. Xu, Q. Li, N. Ophir, K. Padmaraju, L. W. Luo, L. Chen, M. Lipson, K. Bergman. **Colorless Optical Network Unit Based on Silicon Photonic Components for WDM PON.** IEEE Photonics Technology Letters, 24 (16), 2012.

- K. Padmaraju, N. Ophir, Q. Xu, B. Schmidt, J. Shakya, S. Manipatruni, M. Lipson, K. Bergman. **Error-free transmission of microring-modulated BPSK.** Optics Express, 20 (8), 2012.
- Q. Li, N. Ophir, L. Xu, K. Padmaraju, M. Lipson, K. Bergman. **Experimental Characterization of the Optical-Power Upper Bound in a Silicon Microring Modulator.** IEEE Optical Interconnects Conference, Albuquerque, 2012.
- R. R. Grote, K. Padmaraju, J. B. Driscoll, B. Souhan, K. Bergman, R. M. Osgood. **10 Gb/s Error-Free Operation of an All-Silicon C-band Waveguide Photodiode.** Conference on Lasers and Electro-Optics (CLEO), San Jose, 2012.
- K. Padmaraju, J. Chan, L. Chen, M. Lipson, K. Bergman. **Dynamic Stabilization of a Microring Modulator Under Thermal Perturbation.** Optical Fiber Communication Conference (OFC), Los Angeles, 2012.
- K. Padmaraju, N. Ophir, Q. Xu, B. Schmidt, J. Shakya, S. Manipatruni, M. Lipson, K. Bergman. **Error-Free Transmission of DPSK at 5 Gb/s Using a Silicon Microring Modulator.** European Conference on Optical Communications (ECOC), Geneva, Switzerland, 2011.
- L. Xu, K. Padmaraju, L. Chen, M. Lipson, K. Bergman. **10-Gb/s Access Network Architecture Based on Micro-Ring Modulators With Colorless ONU and Mitigated Rayleigh Backscattering.** IEEE Photonics Technology Letters, 23 (13), 2011.
- A. Biberman, H. L. R. Lira, K. Padmaraju, N. Ophir, J. Chan, M. Lipson, K. Bergman. **Broadband Silicon Photonic Electro-Optic Switch for Photonic Interconnection Networks.** IEEE Photonic Technology Letters, 23 (8), 2011.
- K. Padmaraju, N. Ophir, S. Manipatruni, C. B. Poitras, M. Lipson, K. Bergman. **DPSK Modulation Using a Microring Modulator.** Conference on Lasers and Electro-Optics (CLEO), Baltimore, 2011.
- N. Ophir, K. Padmaraju, A. Biberman, L. Chen, K. Preston, M. Lipson, K. Bergman. **First Demonstration of Error-Free Operation of a Full Silicon On-Chip Photonic Link.** Optical Fiber Communication Conference (OFC), Los Angeles, 2011.

- L. Xu, K. Padmaraju, L. Chen, M. Lipson, K. Bergman. **First Demonstration of Symmetric 10-Gb/s Access Networks Architecture based on Silicon Microring Single Sideband Modulation for Efficient Upstream Signal Remodulation.** Optical Fiber Communication Conference (OFC), Los Angeles, 2011.

- K. Padmaraju, N. Ophir, A. Biberman, L. Chen, E. Swan, J. Chan, M. Lipson, K. Bergman. **Intermodulation Crosstalk from Silicon Microring Modulators in Wavelength-Parallel Photonic Networks-on-Chip.** IEEE Photonics Society Conference, Denver, 2010.

- A. Biberman, H. L. R. Lira, K. Padmaraju, N. Ophir, M. Lipson, K. Bergman. **Broadband CMOS-Compatible Silicon Photonic Electro-Optic Switch [post-deadline paper].** Conference on Lasers and Electro-Optics (CLEO), San Jose, 2010.

Appendix B

Efficacy of Squarewave Dithering

The Fourier representation of a normalized 2π-periodic ideal square wave is given as

$$f(t,\phi) = \frac{4}{\pi} \sum_{n=1,3,5\ldots}^{\infty} \frac{\sin(nt+\phi)}{n} \tag{B.1}$$

As per the construction in section 4.1, when the generated optical modulation is in-phase with the driving dithering signal, the product is given as

$$f(t,0)f(t,0) = \frac{16}{\pi^2} \left(\sum_{n=1,3,5\ldots}^{\infty} \frac{\sin(nt)}{n} \right) \left(\sum_{n=1,3,5\ldots}^{\infty} \frac{\sin(nt)}{n} \right) \tag{B.2}$$

The DC component is given as the integral of Eq. B.2. Using the orthogonality principle (Eq. 4.2), the cross-terms can be eliminated, leaving the non-zero terms as follows:

$$\begin{aligned} \int f(t,0)f(t,0)dt &= \frac{16}{\pi^2} \int \sum_{n=1,3,5,\ldots}^{\infty} \frac{\sin^2(nt)}{n^2} dt \\ &= \frac{16}{\pi^2} \left(\frac{1}{2}\right) \sum_{n=1,3,5,\ldots}^{\infty} \frac{1}{n^2} \\ &= \frac{16}{\pi^2} \left(\frac{1}{2}\right) \left(\frac{\pi^2}{8}\right) = 1 \end{aligned} \tag{B.3}$$

where the infinite summation has been solved as a modified Basel series. Similarly, when the generated optical modulation is out-of-phase with the driving dithering signal, the product and DC component are given as Eq. B.4 and B.5, respectively,

$$f(t,0)f(t,\pi) = \frac{16}{\pi^2} \left(\sum_{n=1,3,5\ldots}^{\infty} \frac{\sin(nt)}{n} \right) \left(\sum_{n=1,3,5\ldots}^{\infty} \frac{\sin(nt+\pi)}{n} \right) \tag{B.4}$$

$$\int f(t,0)f(t,\pi)dt = -\frac{16}{\pi^2}\int \sum_{n=1,3,5...}^{\infty} \frac{\sin^2(nt)}{n^2}dt = -1 \tag{B.5}$$

Hence, the DC component takes on a value of {1, -1}, in comparison to using normalized sinusoidal waveforms (section 4.1), in which the DC components have values of {1/2, -1/2}.

Appendix C

Intermodulation Crosstalk Characteristics of WDM Silicon Microring Modulators

In this appendix the author presents work that elaborates on and experimentally characterize the intermodulation crosstalk properties of a 10-Gb/s silicon microring modulator. Bit-error-rate measurements and eye diagrams are used to discern the degradation in signal quality due to intermodulation crosstalk. Evaluation of the power penalties with varying channel spacing are used to support WDM cascaded microring modulator channel spacings as dense as 100 GHz with negligible expected intermodulation crosstalk.

C.1 Intermodulation Crosstalk in Multiplexed Microring Modulators

Fig. C.1(a) illustrates the common WDM configuration of microring modulators, whereby the radius of each microring is tuned to an unique wavelength. As each source wavelength propagates along the bus waveguide, it is optically modulated by the microring modulator corresponding to its wavelength. By this arrangement, parallelized high-speed electrical signals are imprinted on the WDM source wavelengths. With the ability to independently modulate the optical signals along the same bus waveguide, the bandwidth density of the photonic system is drastically improved, helping to meet

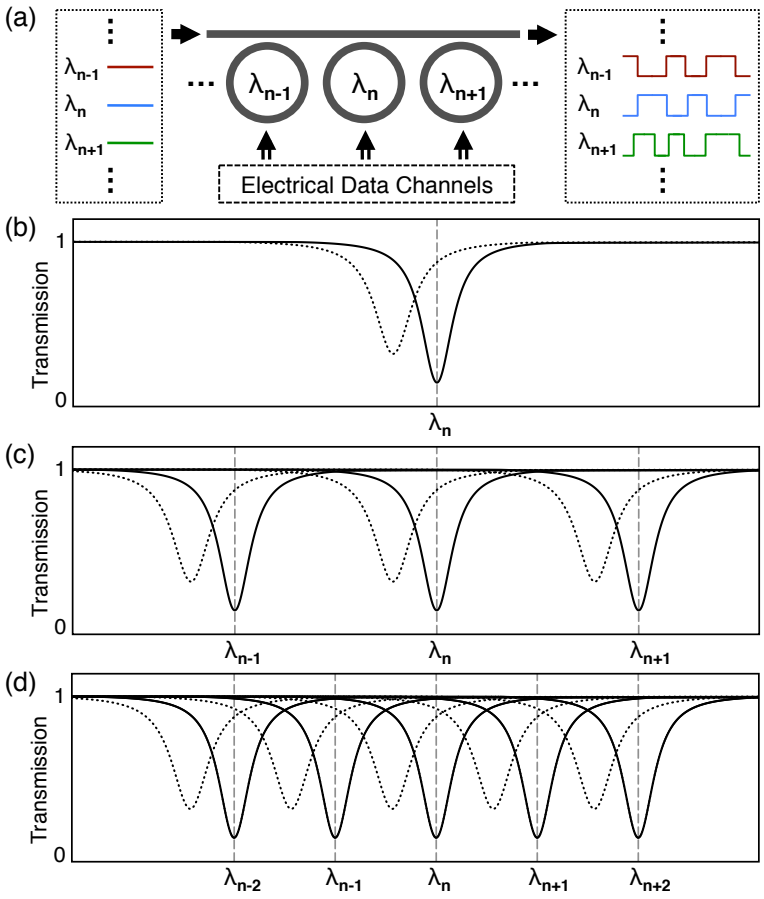

Figure C.1: (a) Configuration that cascades microrings of varying radius along a single waveguide bus to generate WDM optical signals from parallel electrical data streams. (b) Transmission spectrum of the two bit-states (solid and dashed) of a single microring modulator. The position of the wavelength is indicated with a vertical line. (c) Aggregate transmission spectrum of the cascaded microring modulators when using a coarse channel spacing. (d) Aggregate transmission spectrum of the cascaded microring modulators when using a dense channel spacing.

the footprint constraints of microelectronic environments [105].

Fig. C.1(b) illustrates the functionality of an individual microring modulator. Displayed in solid is the passive optical resonance of the microring modulator. Through injection of carriers the resonance is shifted (displayed dashed), allowing a '1' bit to be imprinted on the aligned optical wavelength. Schematically depicted is the decrease in the quality factor (Q), caused by the increased loss due to free carrier absorption from

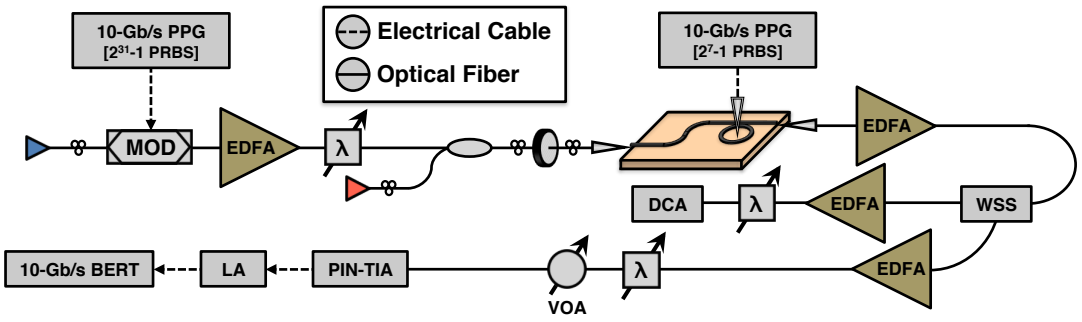

Figure C.2: Experimental setup used to measure and characterize intermodulation crosstalk.

the injected carriers [82]. It should be noted that depletion mode modulators work in a similar fashion, utilizing an expansion of the depletion zone instead of carrier injection, resulting in a reversed but identical modulation mechanisms [106].

Fig. C.1(c) illustrates the scenario of microring modulators cascaded in a WDM configuration. Here, the wavelength spacing between microring resonances is kept sufficiently coarse such that the modulated resonances do not overlap with neighboring optical signals. However, as the density of the WDM signals increases (the channel spacing is decreased), these resonances will begin to overlap, as shown in Fig. C.1(d). As a consequence, each wavelength is not only modulated by the corresponding microring modulator, but adjacent modulators as well. This intermodulation (IM) crosstalk serves as a limit on the WDM channel spacing density. In this work the author shows the deleterious effect of IM crosstalk on the quality of the microring-modulated signal. Additionally, an analysis is provided on the limitations on channel spacing WDM cascaded microring modulators.

C.2 Measurements and Results

C.2.1 Experimental Setup

The goal of the experimental characterization was to verify and measure the deleterious effects of the microring-induced IM crosstalk using standard optical performance metrics. To do this rigorously we created an experimental setup (Fig. C.2) with two signals. The first signal, tuned near the resonant wavelength of the microring, was modulated by the microring modulator to verify its functionality. The second signal

emulated a signal spaced adjacently in the WDM grid. This second signal, modulated prior, experiences IM crosstalk from the microring modulator as the wavelength spacing between the two signals is brought closer.

In the experimental setup, we used a 6-μm radius carrier-injection microring modulator (passive Q of $\sim$6000) fabricated at the Cornell Nanofabrication Facility. Further fabrication details can be found in [61].

The modulator was electrically contacted with high-speed RF probe tips. To electrically drive the microring modulator, a PPG was used to generate a 10-Gb/s NRZ 2^7-1 PRBS electrical signal. The 1-Vpp signal was biased at 0.6 V and conditioned with a pre-emphasis circuit to enable high-speed operation of the device [82]. A CW tunable laser was set to TE polarization and tuned in wavelength near the resonant wavelength of the microring (1546.7 nm) in order to produce an optimal 10-Gb/s microring-modulated signal.

To generate the second signal, the one being afflicted by IM crosstalk, we used a second separate tunable laser, and a commercial $LiNbO_3$ MZM. A second PPG, generating a 2^{31}-1 PRBS pattern, was used to drive the $LiNbO_3$ MZM modulator. The use of two different PPGs with two different PRBS patterns ensured that there was no correlation in the modulation data of the two signals.

The laser power levels were set such that the power of the two signals coming off-chip was equivalent. Once off-chip, the two signals were amplified and then separated using a wavelength-selective-switch (WSS).

The eye diagram of each signal was captured as the wavelength spacing between the two signals was decreased. Additionally, following reception of each signal on a PIN-TIA and limiting amplifier, a BERT was used to measure the BER curves of each signal.

C.2.2 Eye Diagrams and BER Measurements

Fig. C.3 depicts the eye diagrams recorded as the wavelength spacing between the two signals is decreased. Specifically, the wavelength of the microring-modulated signal is fixed near the resonant wavelength of the microring. The wavelength of the second signal (modulated by the $LiNbO_3$ MZM) was incremented closer to the wavelength of the first signal. This was done in two sweeps approached from both higher and lower

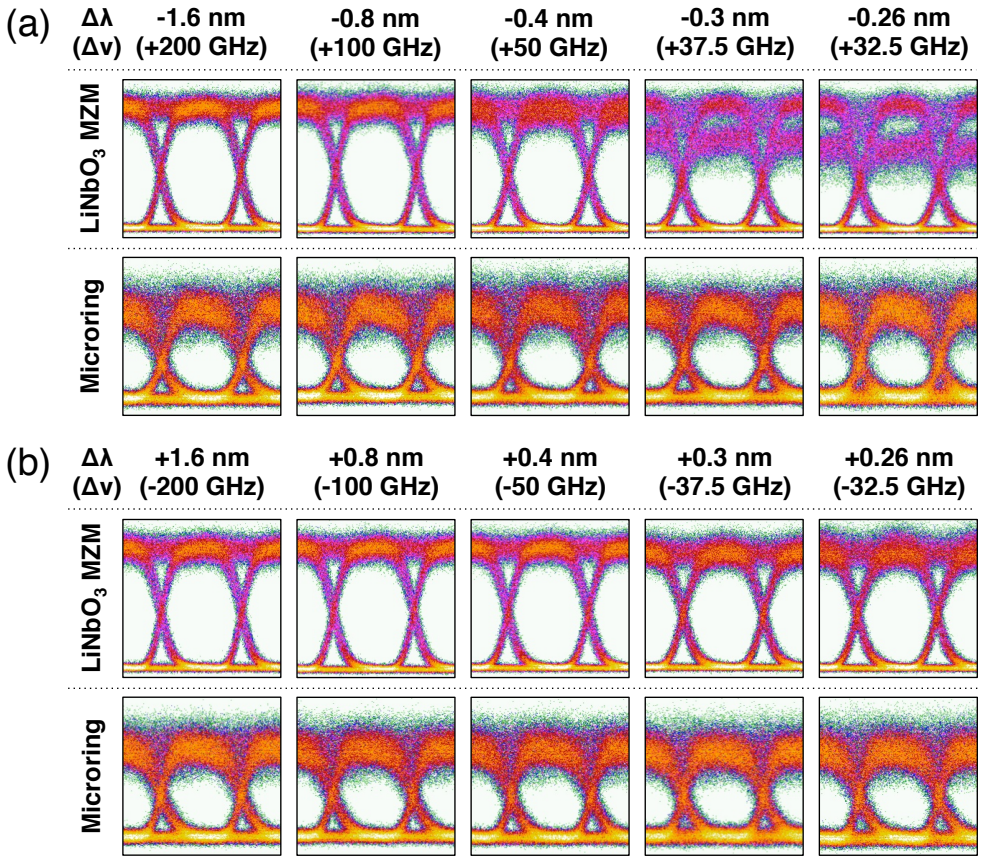

Figure C.3: Eye diagrams when the MZM-modulated channel is spaced (a) below in wavelength relative to the microring-modulated channel and (b) above in wavelength relative to the microring-modulated channel.

wavelengths relative to the resonance of the microring. The motivation for this was to expose the asymmetry of the IM crosstalk relative to wavelength.

Given the close spacing of the signals, a critical aspect of this experiment was to verify that observed crosstalk was due to the microring-induced IM crosstalk, and not filtering crosstalk from the separation of the signals. The consistent eye diagrams of the microring-modulated signal indicate that the filtering was sufficient to completely separate the signals. The BER measurements in Fig. C.4(a) and C.4(b) further affirm this fact, showing near identical BER curves for the microring-modulated signal at all channel spacings.

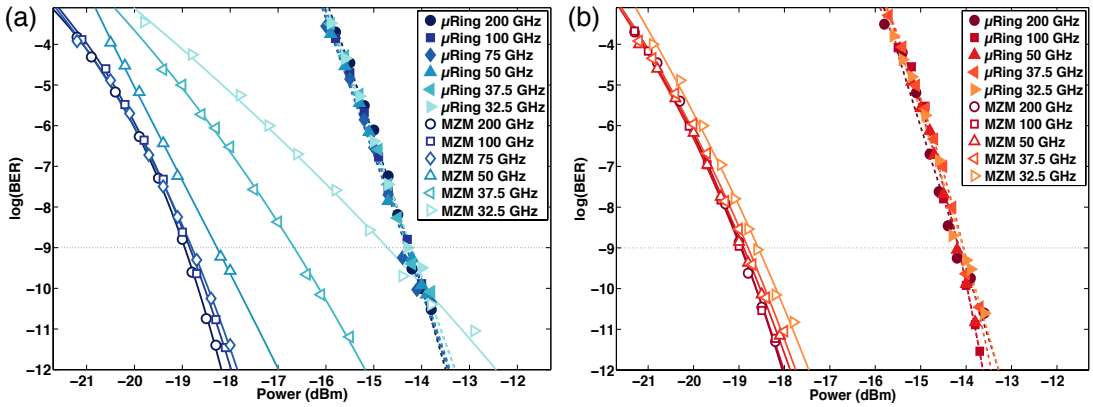

Figure C.4: BER measurements when the MZM-modulated channel is spaced (a) below in wavelength relative to the microring-modulated channel and (b) above in wavelength relative to the microring-modulated channel.

C.2.3 Power Penalties vs. Channel Spacing

The BER measurements in Fig. C.4 are used to assess the power penalties as the channel spacing is reduced. Trend lines were established by exponentially fitting the BER measurements [107]. Fig. C.5 plots the power penalties from these BER curves against the channel spacing.

We develop a simple model to provide a general expression for the crosstalk-induced power penalty vs. channel spacing. First, we note that a power penalty (pp) can commonly be attributed to the eye opening of the signal, that is, the power in the '1' bit ($P1$) and '0' bit ($P0$) in the data signal [108], also illustrated in Fig. C.6(a).

$$pp = 10 \log \left(\frac{P_1 - P_0}{P_1 + P_0} \right) \tag{C.1}$$

The main deleterious mechanism of IM crosstalk is to suppress the power in the '1' bit and '0' bit of the adjacent channel. Fig. C.6(b) illustrates the corresponding decrease in eye opening. To determine what this eye closure is we model the microring transmission spectrum using as a Lorentzian function [109].

$$T(\lambda, \lambda_0, Q) = \left(1 + \left(\frac{2Q(\lambda - \lambda_0)}{\lambda_0} \right)^2 \right)^{-1} \tag{C.2}$$

As seen in the diagram of Fig. C.6(c), the two bit-states comprising microring modulation can be described with parameters described by the Q and resonant wavelength

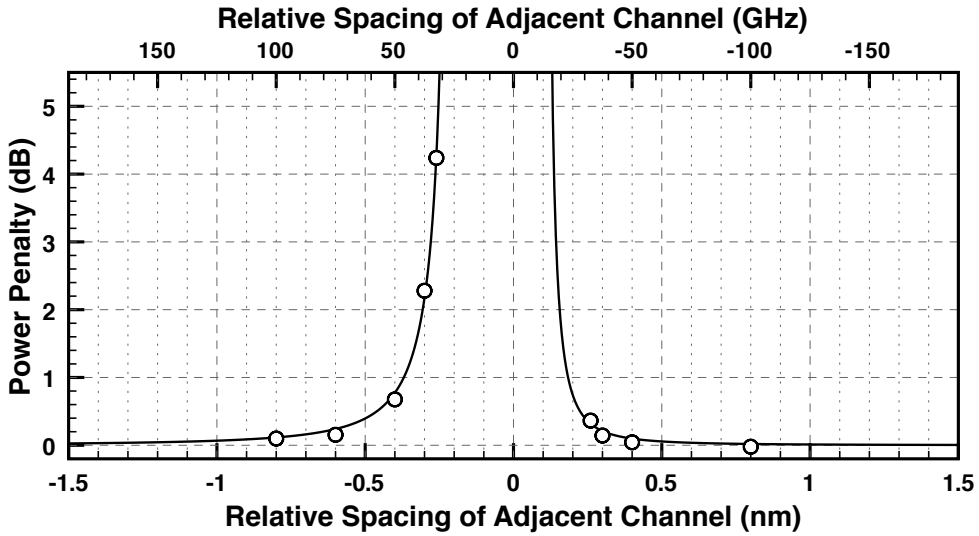

Figure C.5: Measured power penalties vs. relative channel spacing, fitted (separately for lower and higher wavelength spacings) to Eq. C.3.

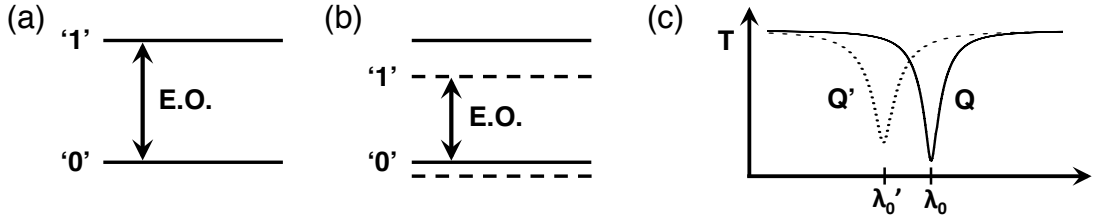

Figure C.6: Eye opening (E.O.) under (a) normal operation, and (b) when the data channel is suffering from intermodulation crosstalk. (c) Illustration of the two bit-states comprising microring modulation.

(λ_0) of the microring. During modulation, λ_0 changes from the free carrier dispersion effect, and Q changes due to free carrier absorption [82]. Equating the reduction in the '1' bit to the transmission of the microring, the relative incurred power penalty, $\Delta pp = pp - pp'$, is then

$$\Delta pp = 10 \log \left(\left(\frac{P_1 - P_0}{P_1 + P_0} \right) \left(\frac{T(\lambda, \lambda_0, Q) P_1 + P_0}{T(\lambda, \lambda_0, Q) P_1 - P_0} \right) \right) \tag{C.3}$$

The measured power penalties are fitted to Eq. C.3 (see Fig. C.5), showing the large increases in power penalty as the channel spacing is progressively decreased from either side.

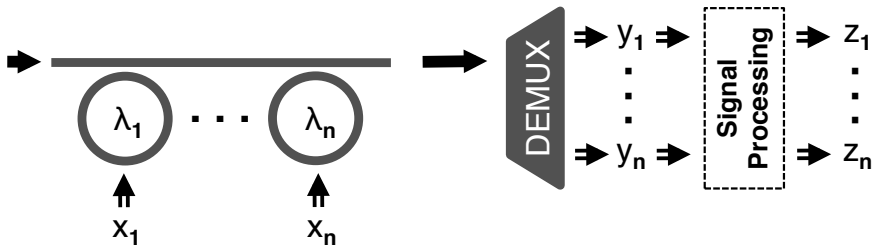

Figure C.7: Schematic depicting the use of DSP at the receive end of the optical link to mitigate intermodulation crosstalk and allow denser channel spacing.

C.3 Analysis

Our fitted measurements of power penalties show the expected features of IM crosstalk. Mainly, that it increases with decreased channel spacing, and secondly, that it is asymmetric (attributable to the unique modulation mechanism of the microring). For a system using a microring modulator with these Q characteristics, power penalties of 0.1 dB and 0.7 dB were measured for channel spacings of 100 GHz and 50 GHz, respectively (see Fig. C.5), providing evidence that microring modulators would be suitable for use in current telecom WDM systems, which are routinely spaced at 100 GHz [108].

The Q characteristics of the microring modulator can be tailored as necessary for applications requiring even denser channel spacing. However, increasing the Q of the microring increases the photon lifetime, which puts a limitation on the modulation bandwidth of the microring [33]. An interesting alternative for increasing the channel density is to use electronic digital signal processing (DSP) at the receive end of the optical link [110], as depicted in Fig. C.7. The deterministic nature of IM crosstalk especially lends itself towards mitigation using DSP. For example, a simple relation for IM crosstalk cancellation (referencing Fig. C.7) can be expressed as

$$z_n = y_n + \alpha z_{n-1} \tag{C.4}$$

where due to the asymmetry of IM crosstalk, only the contribution from the lower channel is relevant for the crosstalk cancellation (hence, $z_1 = y_1$).

C.4 Conclusion

This work has measured and extrapolated power penalties from IM crosstalk for a typical microring modulator operating at 10 Gb/s. We expect similar results at the higher data rates that microring modulators are trending towards [33]. Our power penalty measurements show credibility towards the use of the normative WDM channel spacings of 100 GHz and 50 GHz. Our proposed use of DSP may help push this channel spacing further.

However, it should be noted that in a completely microring-based link, IM crosstalk is not the only factor constraining channel spacing density. Other relevant parameters include spectral crosstalk from the microring demultiplexing filters, aggregate (including electrical driving circuitry) energy efficiency when using different bit-rates, and non-linear optical effects within the silicon waveguides [26, 111]. Such studies point towards either a 50 GHz or 100 GHz WDM channel spacing as preferred for system-optimized microring-based optical links.

Appendix D

Phase Modulation using Silicon Microring Modulators

In this appendix the author presents work on the generation of error-free binary-phase-shift- keyed (BPSK) data at 5 Gb/s using a silicon microring modulator. Prior work by the author had demonstrated the first experimental phase modulation using a microring modulator. In this work, microring-modulated BPSK is propagated at fiber lengths up to 80 km, maintaining error-free performance, while demonstrating resilience to chromatic dispersion. Bit-error-rate measurements and eye diagrams are used to show near equivalent performance of a microring-based BPSK modulator as compared to commercial $LiNbO_3$ phase modulators.

Prior to this work, research efforts had focused exclusively on using the microring modulator for the generation of on-off-keyed (OOK) data. In contrast, this work demonstrated the first error-free generation and propagation of BPSK data for long-reach applications using a silicon microring modulator. The BPSK modulation format has several beneficial characteristics over OOK: a sensitivity improvement, lower susceptibility to fiber non-linearities, and reduced crosstalk in WDM systems [112]. This demonstration effectively combines the benefits of silicon microring modulators and the BPSK format.

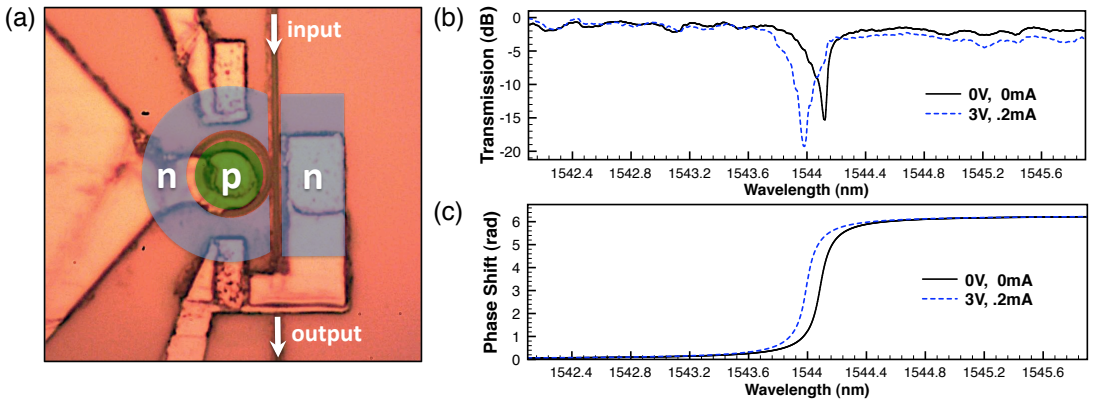

Figure D.1: (a) Microscope image of the microring modulator (doping regions are highlighted in green for p-doping and blue for n-doping) and its corresponding (b) amplitude and (c) phase response under DC condition.

D.1 BPSK Modulation using a Microring Modulator

The silicon microring modulator used in this work was fabricated at the Cornell Nanofabrication Facility (CNF). As depicted in Fig. D.1(a), it consists of a 5-μm-radius microring side-coupled to waveguide. The microring and waveguide are designed for quasi-TE operation using a width and height of 450 nm and 200 nm, respectively. A 50-nm Si slab surrounding the microring was doped accordingly to produce a *p-i-n* structure capable of injecting carriers into the microring (Fig. D.1(a)).

The optical resonance of the microring in its passive state is shown in Fig. D.1(b). Carrier injection, enabled through the *p-i-n* structure, produces a blue shift in the resonance via the free carrier dispersion mechanism to generate OOK data [82].

In addition to generating traditional OOK data, it had been theorized [113] and demonstrated experimentally (at 250 Mb/s, in the author's prior work) that the microring modulator is also capable of producing BPSK data. BPSK generation is enabled through the utilization of the microrings strong localized phase response.

The phase response of the microring modulator can be calculated from the optical length of the microring, L, the loss in the cavity, α, and the coupling coefficient, κ [27]. Using these parameters, the field response of the microring is given as

$$\frac{E_{out}}{E_{in}} = \frac{-\alpha + (1-\kappa)e^{\frac{-i2\pi L}{\lambda}}}{-\alpha(1-\kappa) + e^{\frac{-i2\pi L}{\lambda}}} \tag{D.1}$$

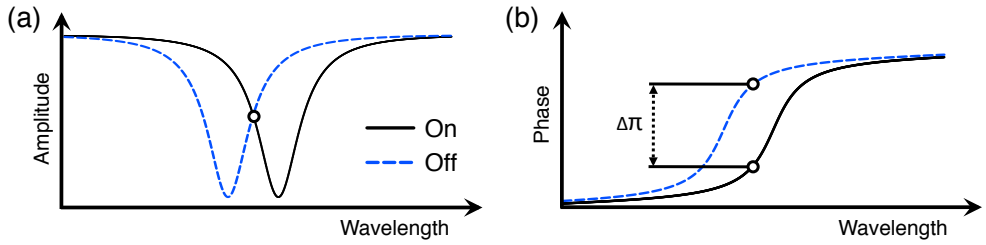

Figure D.2: BPSK generation using a microring modulator. (a) The two bit-states have equivalent amplitudes, but (b) a difference in phase of π.

Only over-coupled microrings, where $\kappa > \alpha$, exhibit the strong phase response necessary for phase modulation. This condition can be met by appropriately specifying the gap between the microring and waveguide. We use the amplitude response (Fig. D.1(b)) and Eq. D.1 to fit the phase response of the over-coupled microring used in this experiment. As can be seen in Fig. D.1(c), the phase response of the microring blue shifts in tandem with the blue shift of the resonance. While Fig. D.1(c) is a derived fit, the wavelength shift of the phase response has been confirmed through a direct measurement in the author's earlier work.

Similar to the generation of OOK, generation of BPSK using a microring modulator exploits a resonance shift to produce the desired bit-state. However, BPSK generation requires positioning the wavelength such that the optical bits have equivalent amplitude (Fig. D.2(a)), but differ by a phase shift of π (Fig. D.2(b)). A consequence of operating inside the resonance region is an inherent insertion loss completely separate from the waveguide or coupling losses. This insertion loss was approximately 3 dB for the microring modulator used in the experiment. It should be noted that while Fig. D.2 depicts perfect symmetry between the two resonance states, in the carrier-injected state, free carrier absorption increases the loss in the cavity, leading the resonance to approach critical coupling. This is visible in the two resonance states depicted in the experimental measurement of Fig. D.1(b), with the carrier-injected state closer to critical coupling. The asymmetry produces a pattern dependency in the demodulated BPSK signal, as seen in the experimentally demodulated BPSK signals of Fig. D.5.

In Fig. D.3, the fitted resonances of Fig. D.1(b) are used to generate the signal constellation of the microring-modulated BPSK generated in this experiment. As Fig. D.3(a) illustrates, the combination of the phase shift and amplitude dip produces a

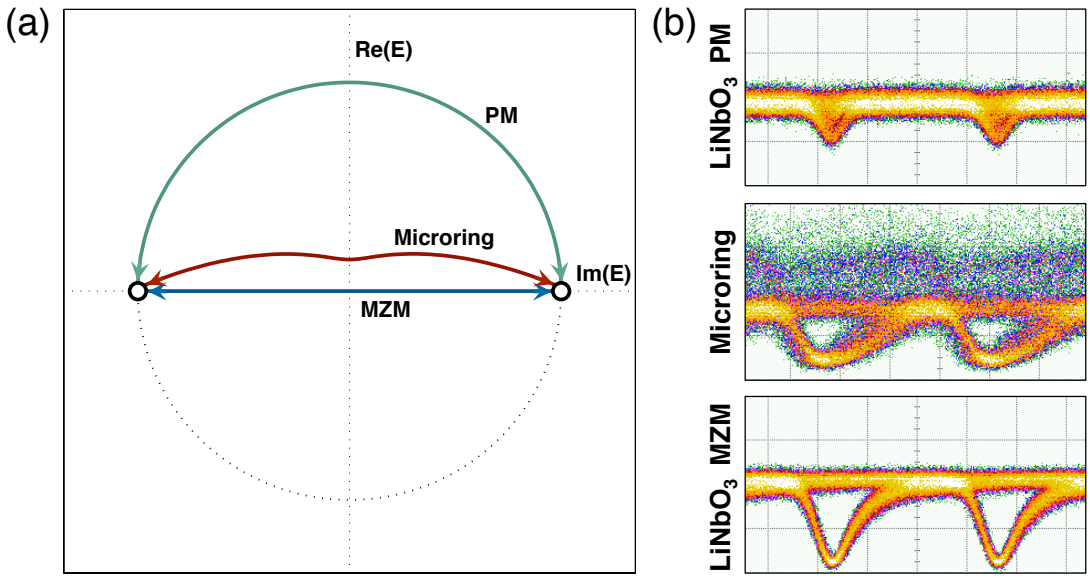

Figure D.3: (a) Signal constellation for PM-, microring-, and MZM-modulated BPSK. (b) PM-, microring-, and MZM-modulated BPSK before demodulation.

modulation mechanism unique to the microring modulator, differing from the phase modulation mechanism in either the PM or MZM [113]. The experimentally measured BPSK signals confirm that the microring modulator generates amplitude dips larger than the PM, but not reaching full extinction such as the MZM (Fig. D.3(b)). It should be noted that the noise present on the microring-modulated BPSK signal of Fig. D.3(b) is a result of the previously mentioned pattern dependency of the microring modulator.

The simultaneous combination of amplitude and phase modulation generates chirp characteristics that differ from those produced by the $LiNbO_3$ PM or MZM. Subsequently, it is expected that the subjection of microring-modulated BPSK to the dispersive effects of optical fiber will yield different results when compared to using BPSK generated from a PM or MZM; hence, motivating experimental measurements to validate the use of microring-modulated BPSK for long-reach applications.

D.2 Long-Haul Transmission of Microring-Modulated BPSK

D.2.1 Experimental Setup

Our characterization consisted of generating BPSK using the aforementioned silicon microring modulator, and then propagating it through progressively longer spans of fiber while observing the deformation of the eye pattern and changes in the bit-error-rate. In the experimental setup, (Fig. D.4), a PPG was used to generate a 5-Gb/s NRZ 2^7-1 PRBS electrical signal. The 1-V_{pp} signal was biased at 1.2 V and conditioned with a pre-emphasis circuit to enable high-speed operation of the modulator [82]. A CW tunable laser at a wavelength of 1544 nm was set to a TE polarization before being launched onto the chip. The microring-modulated BPSK signal egressing from the chip was amplified with an EDFA, and filtered (λ), before being passed into [0, 30, 55, 80] km of single-mode fiber (SMF) at a power of 11 dBm. The varying lengths of fiber result in variable amounts of accrued loss; hence, a variable optical attenuator (VOA) was used to attenuate the signal to a fixed power of -17 dBm, thereby ensuring OSNR consistency between measurements. This signal was then amplified and filtered before being passed into a thermally stabilized delay line interferometer (DLI) to demodulate the BPSK signal. Because the differential of PRBS is equivalent to the original PRBS, error testing is possible without the customary differential-phase-shift-keying (DPSK) encoder and decoder. The demodulated signal was received using a PIN-TIA photodetector followed by a limiting amplifier and fed to a BERT for BER measurements. In addition, a sampling oscilloscope (DCA) was used to record eye patterns.

For comparison, a commercial $LiNbO_3$ dual-drive MZM (rated for 10-Gb/s operation) was inserted in place of the microring modulator. In this setup, both the inverted and non-inverted ports of the PPG are used to generate 4-V_{pp} electrical signals that drive the MZM in a push-pull configuration, producing the desired BPSK. The launch and exit powers of the fiber span were also maintained at 11 dBm and -17 dBm, respectively, to ensure consistency with the characterization of the microring-modulated BPSK. Similarly, a commercial $LiNbO_3$ single-arm PM (also rated for 10-Gb/s operation) was characterized in the same configuration, using a single output of the PPG to generate the 6-V_{pp} electrical signal needed to drive the PM.

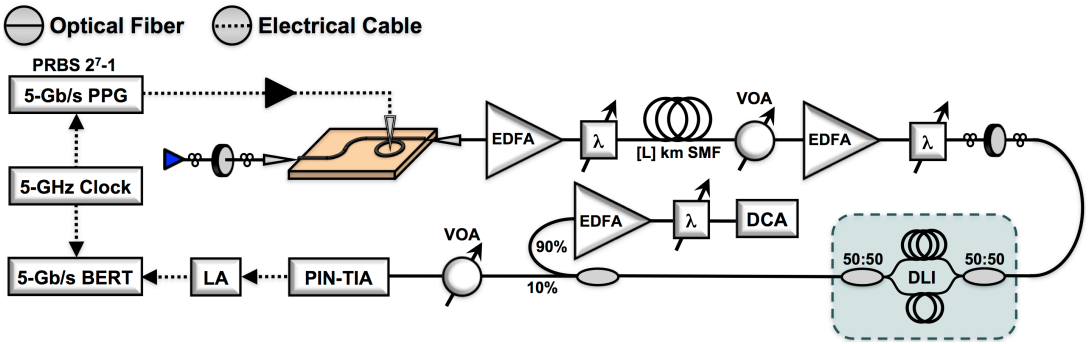

Figure D.4: Experimental setup for BER validation of microring-modulated BPSK.

D.2.2 Experimental Results

Fig. D.5 depicts the eye patterns for the constructive port of the demodulated BPSK signals as they propagate through the progressively increasing fiber spans. For the PM- and MZM- modulated BPSK signals, the chirp induced from the modulation results in a gradual NRZ to RZ conversion of the demodulated signal. A similar phenomenon occurs with the microring-modulated BPSK signal. However, from the eye diagrams, it is observed that the fiber span at which the microring-modulated BPSK signal reaches an optimal RZ format occurs sooner (at 55 km) when compared to the PM- or MZM-modulated BPSK signal.

This behavior is further validated by the BER measurements (Fig. D.6(a)) conducted on the corresponding demodulated BPSK signals of Fig. D.5. Error-free performance is confirmed for microring-modulated BPSK up to the maximally tested fiber span of 80 km. The power-penalties, as measured at the 10^{-9} error-rate point, and referenced to the 0-km propagation of the MZM-modulated BPSK, are summarized in Fig. D.6(b). The chirp-induced NRZ to RZ conversion results in better receiver sensitivity, and hence negative power-penalty relative to the power-penalty with no fiber propagation [114]. The fiber-propagated behavior of the PM- and MZM-modulated BPSK are similar, exhibiting gradually decreasing power-penalties until finally reaching power penalties of -0.5 dB and -0.4 dB, respectively, relative to their 0-km propagation. As expected and indicated by the measurements, the PM-modulated BPSK signal suffers from more chirp than the MZM-modulated BPSK signal.

In contrast, the microring-modulated BPSK, as was noted from the eye patterns,

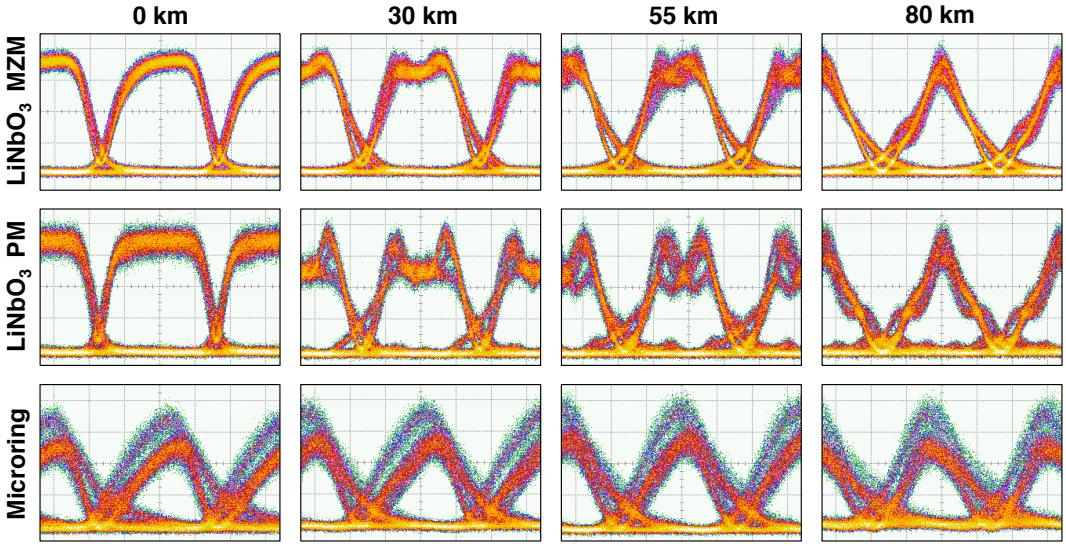

Figure D.5: Eye patterns of the demodulated BPSK signal from the $LiNbO_3$ MZM (top row), $LiNbO_3$ PM (middle row), and silicon microring modulator (bottom row) after propagating [0, 30, 55, 80] km and passing through the fiber DLI.

achieves its lowest power-penalty at 55 km. More importantly, the power-penalty of the microring modulator relative to the MZM is less than 1.3 dB throughout the 80-km propagation of the signal. Because the bandwidth of the microring modulator is lower than that of the MZM or PM, a direct comparison of the chirp-induced propagation is not possible. Regardless, this demonstration shows that the relative power-penalty variance of the microring-modulated BPSK is on par with the commercial MZM and PM.

D.3 Conclusion

We have demonstrated error-free generation of BPSK using a microring modulator at a commercially viable data rate of 5 Gb/s. Furthermore, it was shown that this signal can be propagated up to 80 km with a small ($<$ 1dB) variance in its power penalty, illustrating its resilience to chromatic dispersion and validating its use in the aforementioned long-reach applications. As the bit-error-rate measurements showed, this prototype silicon microring modulator has performance comparable to the commercial modulators normally used for the generation of BPSK. In addition, the silicon microring

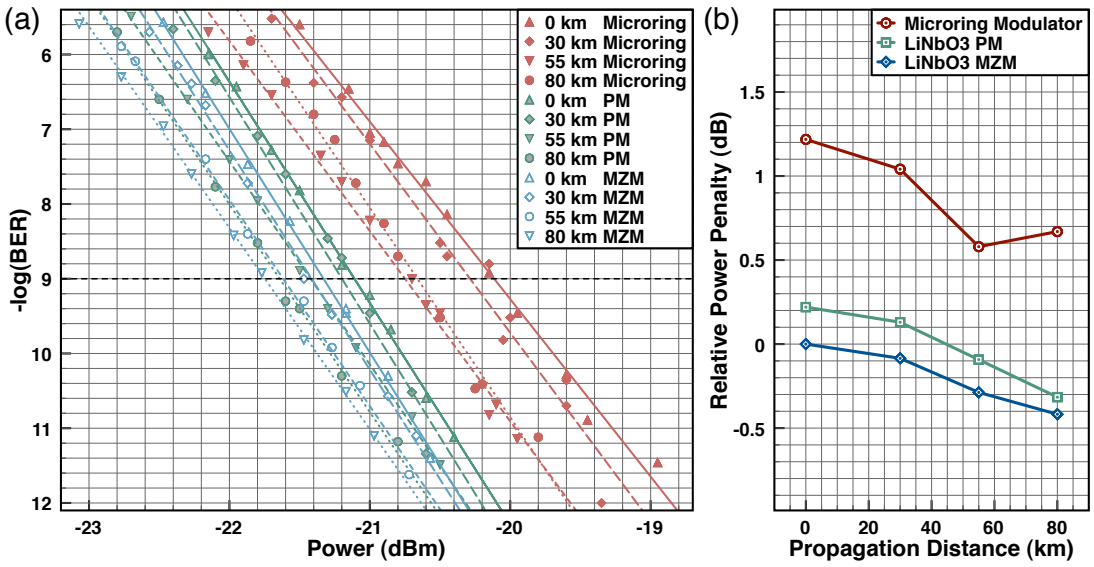

Figure D.6: (a) BER curves. (b) Power penalties taken relative to 0-km propagation of the $LiNbO_3$ MZM-modulated BPSK signal.

modulator has several advantages that would render it preferable over the traditional $LiNbO_3$ PM or MZM.

One advantage of note is the considerably lower drive voltage used for the microring modulator, 1-V_{pp}, versus the 4-V_{pp} and 8-V_{pp} required for the $LiNbO_3$ PM and MZM, respectively. The required drive voltage can be further decreased to sub-volt levels by scaling down the size of the microring modulator, simultaneously reducing the footprint of the device [105]. The low-voltage operation of the microring modulator can enable high-speed optical links while expending with the expensive, high-speed electronic amplifiers normally required. In addition, the wavelength selectivity of the microring modulator can be exploited, enabling the cascading of microring modulators for high-bandwidth wavelength-division-multiplexed (WDM) operation [35]. These advantages are magnified when considering the economy of scale found in long-reach applications, where the low-voltage, integrated WDM operation of microring modulators can translate to a drastic reduction in the number of individual components. As long-reach networks continue to migrate to from PON to WDM-PON, the need for low-cost, integrated photonics, will only further justify the use of microring modulators [115]. Furthermore, recent demonstrations have shown that a combination of microring-

modulated BPSK can produce microring-modulated QPSK signals, foreshadowing its potential use in future long-haul communication networks where QPSK is the preferred next-generation modulation format [116]. Lastly, in our most recent work we have been able to show a full microring-based BPSK link (with the demodulation being performed by a passive microring resonator), showing the potential of microring-modulated BPSK for footprint-constrained network-on-chip applications.